

# Once Again on Wilson Fermion Doubling

S. N. Vergeles

Landau Institute for Theoretical Physics, Russian Academy of Sciences,  
Chernogolovka, Moscow region, 142432 Russia

e-mail: [vergeles@itp.ac.ru](mailto:vergeles@itp.ac.ru)

Received July 21, 2005; in final form, October 11, 2005

Two classes of irregular lattices, in one of which the Wilson fermion doubling is absent, whereas in the other it is formally present, have been presented in my previous works. Irregular lattices are simplicial complexes that are used to define discrete gravity. It has been shown that Wilson fermion doubling is always absent in this discrete gravity with any lattice class, because anomalous modes do not propagate. © 2005 Pleiades Publishing, Inc.

PACS numbers: 04.60.–m, 98.80.H

**1.** Let us consider a generalization of the Dirac action that is defined on a space lattice and has the following properties:

(i) it is local;

(ii) in the naive continuum limit, it is transformed to the Dirac-field action;

(iii) it is phase invariant and  $\gamma^5$  invariant, i.e., invariant under the transformations (a)  $\psi \rightarrow \exp(i\alpha)\psi$ ,  $\bar{\psi} \rightarrow \bar{\psi} \exp(-i\alpha)$  and (b)  $\psi \rightarrow \exp(i\beta\gamma^5)\psi$ ,  $\bar{\psi} \rightarrow \bar{\psi} \exp(-i\beta\gamma^5)$ .

It is well known (see, e.g., [1–4]) that so-called Wilson fermion doubling occurs in the described theory on a hypercubic, or more exactly periodic, lattice. This means that, if one Dirac field exists on the lattice, two Dirac fields are present in the continuum limit. If there is one Weyl field on the lattice, only Dirac fields exist in the continuum limit. In [5], the following theorem was proved: if the fermion action on a periodic lattice has the form

$$I = \sum_{\mathbf{x}, \mathbf{y}} \bar{\psi}_{\mathbf{x}} \hat{H}(\mathbf{x} - \mathbf{y}) \psi_{\mathbf{y}}, \quad (1)$$

where  $\mathbf{x}$  and  $\mathbf{y}$  are the radius-vectors of the sites of the lattice, and it has the above three properties, then the Wilson fermion doubling also occurs. However, the following question has not yet been answered: Does the fermion action with properties (i)–(iii) lead to Wilson fermion doubling on any lattice?

**2.** In my recent works [6, 7], general assurance that Wilson fermion doubling occurs for any lattice generalization of Dirac theory was shown to be doubtful. Irregular lattices (more exactly, simplicial complexes) on which Wilson fermion doubling was absent were found. These complexes were naturally called odd. Complexes on which Wilson fermion doubling formally occurs were also presented. In this work, state-

ments made in [6, 7] are significantly enhanced: even when a lattice formally allows Wilson fermion doubling, this phenomenon is really absent, because anomalous fermion modes (i.e., modes that “multiply” normal fermion modes and give rise to doubling) do not propagate. In this sense, Wilson fermion doubling is absent. This conclusion is valid in the framework of discrete quantum gravity presented in [8, 9].

**3.** Generally speaking, Dirac theory on simplicial complexes naturally arises in the discrete gravity theory proposed in my previous works (see, e.g., [8, 9]). For this reason, it is necessary to briefly describe the discrete quantum gravity theory, the more so that this is required for presenting a new result. The discrete quantum gravity theory was presented in detail in the mentioned works.

Let  $\mathfrak{R}$  be a simplicial complex and  $a_i, a_j, \dots$  be its vertices. In the case of the four-dimensional complex, four Dirac matrices are used with the Euclidean signature:

$$\begin{aligned} \gamma^a, a, b, c, \dots &= 1, 2, 3, 4, \quad \text{tr} \gamma^\alpha \gamma^b = 2\delta^{ab}, \\ \gamma^5 &= \gamma^1 \gamma^2 \gamma^3 \gamma^4, \quad \text{tr} \gamma^5 \gamma^a \gamma^b \gamma^c \gamma^d = 4\epsilon^{abcd}. \end{aligned}$$

Each oriented 1-simplex or edge  $a_i a_j$  is assigned with the Spin(4) group element

$$\Omega_{ij} = \Omega_{ji}^{-1} = \exp\left(\frac{1}{2} \omega_{ij}^{ab} \sigma^{ab}\right), \quad \sigma^{ab} = \frac{1}{4} [\gamma^a, \gamma^b],$$

as well as with the Clifford algebra element

$$\hat{e}_{ij} \equiv e_{ij}^a \gamma^a = -\Omega_{ij} \hat{e}_{ji} \Omega_{ij}^{-1},$$

where  $\omega_{ij}^{ab} = -\omega_{ji}^{ab} = -\omega_{ij}^{ba}$  and  $e_{ij}^a$  are the real variables. Each 0-simplex or vertex  $a_i$  is assigned with mutually conjugate Dirac spinors  $\psi_i$  and  $\bar{\psi}_i$ . Index  $A$

enumerates 4-simplexes. Each 4-simplex  $a_i a_j a_k a_l a_m$  with the index  $A$  is assigned the number  $\varepsilon_{Aijklm} = \pm 1$  whose sign depends on the orientation of this 4-simplex. The symbols  $\bar{\Psi}_{Ai}$ ,  $\Psi_{Ai}$ ,  $\hat{e}_{Aij}$ ,  $\Omega_{Aij}$ , etc., indicate that the edge  $a_i a_j$  belongs to the 4-simplex with the index  $A$ . The action of the gravitational and Dirac fields that is associated with the complex  $\mathfrak{R}$  has the form

$$I = \frac{1}{5 \times 24} \sum_A \sum_{i,j,k,l,m} \varepsilon_{Aijklm} \text{tr} \gamma^5 \times \left\{ -\frac{1}{2l_p^2} \Omega_{Ami} \Omega_{Aij} \Omega_{Ajm} \hat{e}_{Amk} \hat{e}_{Aml} + \frac{1}{24} \hat{\Theta}_{Ami} \hat{e}_{Amj} \hat{e}_{Amk} \hat{e}_{Aml} \right\}, \quad (2)$$

$$\hat{\Theta}_{Aij} = \frac{i}{2} \gamma^a (\bar{\Psi}_{Ai} \gamma^a \Omega_{Aij} \Psi_{Aj} - \bar{\Psi}_{Aj} \Omega_{Aji} \gamma^a \Psi_{Ai}) \equiv \Theta_{Aij}^a \gamma^a \in V. \quad (3)$$

This action is invariant under the following gauge transformations:

$$\begin{aligned} \tilde{\Omega}_{Aij} &= S_{Ai} \Omega_{Aij} S_{Aj}^{-1}, \\ \tilde{e}_{Aij} &= S_{Ai} e_{Aij} S_{Ai}^{-1}, \\ \tilde{\Psi}_{Ai} &= S_{Ai} \Psi_{Ai}, \quad \tilde{\bar{\Psi}}_{Ai} = \bar{\Psi}_{Ai} S_{Ai}^{-1}, \end{aligned}$$

where  $S_{Ai} \in \text{Spin}(4)$ .

Let us present the expression for the partition function  $Z$  in discrete Euclidean gravity, which is transformed to the transfer matrix after the transition to the Lorentzian signature. The vertices and edges of the simplex are enumerated by the indices  $\mathcal{V}$  and  $\mathcal{E}$ , respectively, and  $\Psi_{\mathcal{V}}$ ,  $\Omega_{\mathcal{E}}$ , etc., are corresponding variables. By definition,

$$Z = \text{const} \left( \prod_{\mathcal{E}} \int d\Omega_{\mathcal{E}} \int de_{\mathcal{E}} \right) \left( \prod_{\mathcal{V}} d\bar{\Psi}_{\mathcal{V}} d\Psi_{\mathcal{V}} \right) \exp(-I), \quad (4)$$

where  $d\Omega_{\mathcal{E}}$  is the invariant measure on the  $\text{Spin}(4)$  group and the other measures are clear without comments.

Action (2) has the naive continuum limit. For passage to the continuum limit, it is necessary to introduce the conventional local vertex coordinates

$$x_{Ai}^{\mu} \equiv x^{\mu}(a_{Ai}), \quad \mu = 1, 2, 3, 4,$$

so that the differences between the coordinates of neighboring vertices are small and linearly independent:

$$dx_{Aji}^{\mu} \equiv x_{Ai}^{\mu} - x_{Aj}^{\mu} \sim a,$$

$$\begin{vmatrix} dx_{Am1}^1 & dx_{Am1}^2 & \dots & dx_{Am1}^4 \\ \dots & \dots & \dots & \dots \\ dx_{Am4}^1 & dx_{Am4}^2 & \dots & dx_{Am4}^4 \end{vmatrix} \neq 0.$$

Here,  $a$  is a certain constant that has the length dimension and is on the order of the effective lattice step. In the naive continuum limit, it is supposed that all introduced variables  $\Omega$ ,  $\hat{e}$ ,  $\Psi$ , and  $\bar{\Psi}$  vary only slightly between the neighboring simplexes,  $e_{Ami} \sim a$ , and the elements  $\Omega_{Ami}$  are close to unity. The last condition means that  $\omega_{Ami} \rightarrow 0$ . Let us consider the systems of linear equations

$$\begin{aligned} \omega_{Am\mu} dx_{Ami}^{\mu} &= \omega_{Ami}, \quad e_{Am\mu} dx_{Ami}^{\mu} = e_{Ami}, \\ i &= 1, 2, 3, 4, \end{aligned} \quad (5)$$

that unambiguously determine the 1-forms  $\omega_{Am\mu}$  and  $e_{Am\mu}$ . Let the 1-simplex  $X_{mi}^A = a_m a_i$  belong to the 4-simplexes with the indices  $A_1, A_2, \dots, A_r$ . It is easy to see that the average

$$\omega_{\mu} \left[ \frac{1}{2} (x_{Am} + x_{Ai}) \right] \equiv \frac{1}{r} \{ \omega_{A_1 m \mu} + \dots + \omega_{A_r m \mu} \},$$

which is determined only by the 1-simplex  $a_m a_i$ , satisfies the relation

$$\omega_{\mu} \left[ \frac{1}{2} (x_{Am} + x_{Ai}) \right] dx_{Ami}^{\mu} = \omega_{Ami} \equiv \omega = \omega_{\mu} dx^{\mu}.$$

The 1-form  $e = e_{\mu} dx^{\mu}$  is determined similarly.

Then, it is easy to show that lattice action (2) in the long-wavelength limit is transformed to the known action of the Einstein continuum theory in the Palatini form

$$I = \int \varepsilon_{abcd} \left\{ -\frac{1}{2l_p^2} (R^{ab} \wedge e^c \wedge e^d + \frac{1}{6} \Theta^a \wedge e^b \wedge e^c \wedge e^d) \right\}, \quad (6)$$

$$d\omega^{ab} + \omega_c^a \wedge \omega^{cb} = \frac{1}{2} R^{ab},$$

$$\Theta^a = \frac{i}{2} (\bar{\Psi} \gamma^a \mathcal{D}_{\mu} \Psi - \mathcal{D}_{\mu} \bar{\Psi} \gamma^a \Psi) dx^{\mu},$$

$$\mathcal{D}_{\mu} \Psi_{Ai} = \partial_{\mu} \Psi_{Ai} + \omega_{Ai\mu} \Psi_{Ai}.$$

We point to the important property of the theory. Information on the initial lattice structure is completely lost in the long-wavelength limit: action (6) is independent of the positions of the lattice vertices in the continuum 4-space. This property will be used below.

**4.** We pass to the formulation and analysis of the problem of fermion doubling in the discrete gravity the-

ory described above. In order to solve the problem, it should be extremely simplified. For this reason, we set

$$\Omega_{ij} = 1, \quad (e_{ij}^a + e_{jk}^a + \dots + e_{li}^a) = 0, \quad (7)$$

where the sum is calculated over any closed path consisting of 1-simplexes. Equations (7) mean that the curvature and torsion are equal to zero. Thus, the geometric realization of the complex  $\mathfrak{R}$  is in a Euclidean hyperplane, so that the Cartesian coordinates of the vertex  $a_i$  are  $x_i^a$  and  $e_{ij}^a = x_j^a - x_i^a$  are the Cartesian coordinates of the vector whose beginning and end are at the vertices  $a_i$  and  $a_j$ , respectively. We note that  $\Theta_{ij}^a = -\Theta_{ji}^a$  under conditions (7). Two vertices will be called neighboring if they form the boundary of one edge.

In the continuum limit, Eqs. (7) are represented as  $\oint e^a = 0$ , where the integrals are calculated over all contours. Therefore,  $de^a = 0$  and  $\omega^{ab} = 0$  is the only solution of the equation

$$de^a + \omega^{ab} \wedge e^b = 0.$$

Let us present the equation for the eigenmodes of the discrete Dirac operator in partial case (7). This operator is obtained by varying action (2) with respect to the variable  $\bar{\psi}_i$ . In the four-dimensional case, we have (see [7])

$$\frac{i}{4} \sum_{j(i)} S_{ij}^a \gamma^a \psi_j = \epsilon v_i \psi_i, \quad (8)$$

where

$$S_{ij}^a = (3!)^{-2} \sum_{A(i,j)} \epsilon^{acdf} \epsilon_{A(i,j)ijklm} e_{A(i,j)ik}^c e_{A(i,j)il}^d e_{A(i,j)im}^f. \quad (9)$$

Here, the index  $A(i, j)$  enumerates all the 4-simplexes containing the edge  $a_i a_j$ , the index  $j(i)$  enumerates all the vertices  $a_{j(i)}$  neighboring the vertex  $a_i$ , and  $v_i$  is the oriented 4-volume of that part of the complex which contains only the vertex  $a_i$  and the set of the vertices  $\{a_{j(i)}\}$ . There exist the relations

$$\sum_{j(i)} S_{ij}^a e_{ij}^b = 4 v_i \delta^{ab}, \quad \sum_{j(i)} S_{i,j}^a \equiv 0, \quad (10)$$

that provide the transformation of discrete equation (8) in the long-wavelength limit to the continuum equation

$$i \gamma^a \partial_a \psi = \epsilon \psi. \quad (11)$$

Indeed, this is easily verified by taking into account the relation

$$\psi_j = \psi_i + e_{ij}^a \partial_a \psi_i, \quad (12)$$

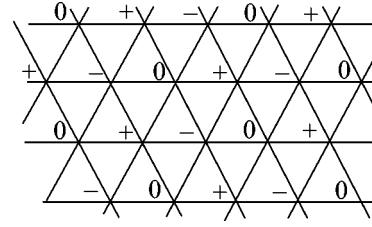


Fig. 1.

that is satisfied with enough accuracy in the long-wavelength limit, i.e., for conventional modes. Here,  $x^a$  are the Cartesian coordinates in the same orthogonal basis in which the components of the vectors  $e_{ij}^a$  are specified. It is again seen that information on the positions of the vertices of the complex is completely lost in the long-wavelength limit; i.e., conventional long-wavelength modes lose information on the lattice structure. The eigenvalues of the modes of Dirac operator (11) are  $\epsilon = \pm|k|$ , where  $k^a$  is the wavevector of a mode. Thus, the eigenvalues of the usual modes can be arbitrarily small.

The main result of works [6, 7] is that the theory under consideration involves two types of lattices. On the lattices of one type, fermion doubling occurs, whereas it is absent on the lattices of the other type. Let us present examples of these two types of lattices.

First, we consider a lattice on which fermion doubling occurs. For illustration, Fig. 1 shows a two-dimensional lattice, but the consideration below is also valid for the multidimensional case. An analog of Eq. (8) on the two-dimensional lattice in the case of zeroth modes ( $\epsilon = 0$ ) for the upper component of the Dirac field can be represented as

$$\sum_{j(i)} (z_{j+1} - z_{j-1}) \phi_j = 0 \longleftrightarrow \sum_{j(i)} z_j (\phi_{j+1} - \phi_{j-1}) = 0. \quad (13)$$

Here, the index  $j(i)$  changes by unity when passing to the neighboring vertex in the process of the successive motion along the boundary of the volume  $v_i$ , which, in the 2D case, consists of all triangles of the complex containing the vertex  $a_i$ ;  $x_j$  and  $y_j$  are the Cartesian coordinates of the vertex  $a_j$ ; and  $z_j = x_j + iy_j$  is its complex coordinate.

Let all the internal vertices of the complex have an even number of neighboring vertices. In addition, let the entire set of internal vertices be divided into a finite number of subsets (three for the case shown in Fig. 1:  $\{a_i\}$ ,  $\{a_i''\}$ , and  $\{a_i''' \}$ ) such that the system of equations for the zeroth mode given by Eq. (13) includes only the differences  $(\psi_{j_1} - \psi_{j_2})$ ,  $(\psi_{j_1}'' - \psi_{j_2}'')$ , and  $(\psi_{j_1}''' - \psi_{j_2}''')$ . It is important that the vertices are in the general positions. The fields  $\psi_j$ ,  $\psi_j''$ , and  $\psi_j'''$  are called the branches of the zeroth mode. In this case, Wilson fermion doubling evidently occurs (the boundary effect can be neglected at  $\alpha_0 \rightarrow \infty$ ). Such an example is shown in

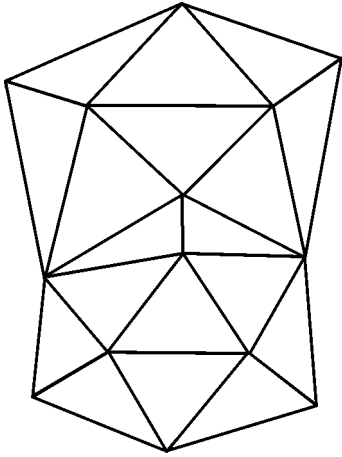


Fig. 2.

Fig. 1, where the vertices belonging to three such subsets are marked by the symbols 0 and  $\pm$ . A nontrivial zeroth mode can be taken in the form  $\varphi^0 = c \neq 0$  and  $\varphi^\pm = [\exp(\pm 2\pi i/3)]c$ . Here,  $\varphi^0$  and  $\varphi^\pm$  are the field  $\varphi$  at the vertices marked in Fig. 1 by the symbols 0 and  $\pm$ , respectively. This nontrivial mode is orthogonal to the trivial mode  $\varphi_i = \text{const}$  (in the natural measure  $\sum_i \bar{\psi}_i \psi_i$  on the regular lattice) and is correspondingly independent. In this example, there are three branches of the nontrivial zeroth mode.

Let us present a 2D lattice on which Wilson fermion doubling is absent. Figure 2 shows a fragment of such a lattice. The lattice in Fig. 2 differs from the lattice in Fig. 1 such that an odd number of edges converge at each internal vertex. In [1, 2], it was proved that Wilson fermion doubling is absent on such lattices and multidimensional analogs of such lattices were constructed.

Further, it is important that, according to the definition, the lattice allows “fermion doubling” if the discrete Dirac operator given by Eq. (8) allows two types of modes with eigenvalues approaching zero.<sup>1</sup> The qualitative difference between them is as follows. The normalized modes of the first type, or normal modes, satisfy the conditions

$$|\psi_i - \psi_j| \sim |\epsilon| |\psi_j| \sim |\epsilon| N^{-1/2},$$

where  $a_i$  and  $a_j$  are the neighboring vertices,  $\epsilon$  is the mode eigenvalue [see Eq. (8)], and  $N$  is the number of the vertices of the complex. The normalized modes of the second type, or anomalous modes, for certain neighboring vertices whose number is comparable with the total vertices of the complex satisfy the conditions

$$|\psi_i^{\mathcal{A}} - \psi_j^{\mathcal{A}}| \sim |\psi_j^{\mathcal{A}}| \sim N^{-1/2}. \tag{14}$$

<sup>1</sup> It is certainly assumed that the sizes of the lattice (i.e., the number of its simplexes) tend to infinity.

The term fermion doubling is presented in the quotation marks, because anomalous soft modes, even if they exist on the lattice, cannot propagate in the continuum limit of the theory under consideration such as conventional soft modes. This is indicated by the long-wavelength behavior of the correlation functions of fields that describe separately conventional and anomalous modes. These correlation functions will be estimated below and these estimates are the result of this work.

We emphasize that the correlation functions of conventional and anomalous soft modes in the theories described in Section 1 behave similarly in the long-wavelength limit. This means that these correlation functions decrease identically at large distances. This statement is easily verified for simple hypercubic lattices. Therefore, fermion doubling is really the doubling of the number of long-wavelength fermion states.

Relations (14) mean that anomalous modes generally change stepwise from a vertex to a neighboring vertex. Hence, the derivatives  $\partial_a \psi_i^{\mathcal{A}}$  of anomalous modes also generally change stepwise from a vertex to a neighboring vertex. Otherwise, Eqs. (8) and (10) would provide the equation  $i\gamma^a \partial_a \psi^{\mathcal{A}} = \epsilon \psi^{\mathcal{A}}$ , where the left-hand side is continuous, while the right-hand side is discontinuous. Moreover, the derivatives of anomalous modes in various directions are incommensurable.

Further, we will show that the effective equation in the continuum limit that describes anomalous modes has the form

$$i\alpha^a(x) \partial_a g^{\mathcal{A}}(x) = \epsilon g^{\mathcal{A}}(x), \tag{15}$$

where  $\alpha^a(x)$  are random functions in the sense indicated below. Indeed, let  $\psi_{sj}^{\mathcal{A}(0)}$ ,  $s = 1, 2, \dots$ , be a complete set of zeroth anomalous modes.<sup>2</sup> Any linear combination of zeroth modes is evidently also a zeroth mode. For this reason, we seek a soft anomalous mode “growing” from zeroth anomalous modes in the form  $\psi_j^{\mathcal{A}} = \sum_s g_{sj}^{\mathcal{A}} \psi_{sj}^{\mathcal{A}(0)}$ , where the numerical field  $g_{sj}^{\mathcal{A}}$  is slowly varying. To derive an equation for the field  $g_{sj}^{\mathcal{A}}$ , we substitute the expression for a soft anomalous mode into Eq. (8):

$$\begin{aligned} & \frac{i}{4} \sum_{j(i)} S_{ij}^a \gamma^a \sum_{s'} [(g_{s'j}^{\mathcal{A}} - g_{s'i}^{\mathcal{A}}) + g_{s'i}^{\mathcal{A}}] \psi_{s'j}^{\mathcal{A}(0)} \\ &= \frac{i}{4} \sum_{j(i)} S_{ij}^a \gamma^a \sum_{s'} \psi_{s'j}^{\mathcal{A}(0)} (g_{s'j}^{\mathcal{A}} - g_{s'i}^{\mathcal{A}}) \\ &= \epsilon v_i \sum_{s'} g_{s'i}^{\mathcal{A}} \psi_{s'i}^{\mathcal{A}(0)}. \end{aligned} \tag{16}$$

<sup>2</sup> Zeroth modes satisfy Eq. (8) with zero right-hand sides.

The first equality in Eq. (16) follows from the fact that  $\psi_{sj}^{\mathcal{A}(0)}$ ,  $s = 1, 2, \dots$ , are zeroth modes. According to the second equality in Eq. (16), the eigenvalue  $\epsilon$  for slowly varying fields  $g_{si}^{\mathcal{A}}$  can be arbitrarily small. In this case, Eq. (16) is reduced to the form

$$\begin{aligned} \frac{i}{4v_i} \sum_{s'} \left[ \sum_{j(i)} (\bar{\psi}_{si}^{\mathcal{A}(0)} S_{ij}^a e_{ij}^b \gamma^a \psi_{s'j}^{\mathcal{A}(0)}) \right] \partial_b g_{s'i} \\ = \epsilon \left[ \sum_{s'} \bar{\psi}_{si}^{\mathcal{A}(0)} \psi_{s'i}^{\mathcal{A}(0)} \right] g_{s'i}^{\mathcal{A}}. \end{aligned}$$

The multiplication of this equation by the matrix  $[\bar{\psi}_{si}^{\mathcal{A}(0)} \psi_{s'i}^{\mathcal{A}(0)}]^{-1}$  reduces it to Eq. (15), where

$$\begin{aligned} \alpha_{ss'}^a &= \frac{1}{4v_i} \sum_{s''} [\bar{\psi}_{si}^{\mathcal{A}(0)} \psi_{s''i}^{\mathcal{A}(0)}]^{-1} \\ &\times \left[ \sum_{j(i)} (\bar{\psi}_{s''i}^{\mathcal{A}(0)} S_{ij}^a e_{ij}^b \gamma^a \psi_{s'j}^{\mathcal{A}(0)}) \right]. \end{aligned} \quad (17)$$

Thus, the operator on the right-hand side of Eq. (15) is a first-order differential operator with variable matrix coefficients that acts on a multicomponent function  $g_s(x)$ ,  $s = 1, 2, \dots$ . Since Eq. (8) and effective equation (15) follow from Hermitian action (2) and Eq. (16), respectively, the operator on the left-hand side of Eq. (15) is Hermitian.

Quantities (17) are irregular functions that depend strongly and locally on the positions of the vertices of the complex. We demonstrate this for 2D gravity on a 2D complex when formulas are transparent. Let the vertex  $a_i$  be at the origin; vertices  $a_j$ ,  $j = 1, 2, 3, 4$ , be its nearest neighbors; and  $e_{ij}^a = (x_j, y_j)$  be the Cartesian coordinates of the corresponding vertex. We assume that  $\psi_{sk}^{\mathcal{A}(0)} = \pm 1$ ,  $\gamma^1 = \sigma^1$ , and  $\gamma^2 = \sigma^2$ .<sup>3</sup> In this case, if  $\psi_1^{\mathcal{A}(0)} = \psi_3^{\mathcal{A}(0)} = -\psi_2^{\mathcal{A}(0)} = -\psi_4^{\mathcal{A}(0)} = 1$ , then

$$\begin{aligned} \sum_{j=1}^4 (\bar{\psi}_{si}^{\mathcal{A}(0)} S_{ij}^b e_{ij}^a \gamma^b \psi_{s'j}^{\mathcal{A}(0)}) \sim ((x_3 - x_1)(y_4 - y_2) \\ + (x_4 - x_2)(y_3 - y_1), 2(y_3 - y_1)(y_4 - y_2)). \end{aligned} \quad (18)$$

It is seen that the components of vector (18) depend strongly on dynamical variables (fields  $e_{ij}^a$ ) and this dependence is spatially local. It is important that the variables  $\{e_{ij}^a\}$  in integral (4) in the theory under consideration can independently vary over a wide range without a change in the action. This statement is exact

<sup>3</sup> Solutions of such a type for zeroth modes were presented in [6, 7] on corresponding complexes.

in the continuum limit for the case where only long-wavelength field modes with wavelengths much longer than the lattice step are taken into account [see Eq. (6), the preceding formulas, and [6, 7)]. Indeed, continuum action (6) is expressed in terms of the 1-forms  $\omega_{Am\mu}$  and  $e_{Am\mu}$ , which are determined from Eqs. (5). These 1-forms obviously do not change [and thereby action (6) does not change] when the right-hand sides of Eqs. (5) vary with simultaneous corresponding variation in the differentials  $dx_{Ami}^\mu$ . The described invariance of the action is associated with the gauge invariance of the theory (which is also certainly exact on a lattice).

Thus, the components  $\alpha^a(x)$  in Eq. (15) are functions of  $x$  that depend strongly and locally on the integration variables  $\{e_\xi\}$  in gauge (4).

Let these components be representable in the form

$$\alpha^a(x) = \beta^a(x) + \lambda \rho^a, \quad (19)$$

where  $\rho_{ss'}^a$  is the constant matrix,  $\lambda$  is the small numerical parameter, and all odd powers of  $\beta(x)$  in the integrand in Eq. (4) are equal to zero:

$$\langle |\beta(x_1) \dots \beta(x_{2n+1})| \rangle_{e_\xi} = 0, \quad n = 0, 1, \dots \quad (20)$$

Points  $x_1, \dots, x_{2n+1}$  can partially or completely coincide with each other. Averaging in Eq. (20) is performed by means of functional integral (4). The subscript  $\{e_\xi\}$  indicates that integration is performed only with respect to the variables  $\{e_\xi\}$ .<sup>4</sup> We also assume that the parameter  $\lambda$  is small so that the expansion in this parameter is meaningful. The last assumption is justified because, according to the above discussion, the quantities  $\alpha(x)$  depend strongly and locally on the variables  $\{e_\xi\}$ , whereas action (2) depends only slightly on these variables.

When the problem of the  $S$  matrix (which is meaningful only in the continuum limit) is solved in the theory under consideration, all  $S$ -matrix elements must be averaged over the variables  $\{e_\xi\}$  before the calculation of probabilities and cross sections. Therefore, if the vertices describing the interaction are universal (i.e., independent of the microstructure of the lattice not only for normal but also for anomalous modes),<sup>5</sup> the propagators of the matter fields in such a theory must be averaged over the variables  $\{e_\xi\}$ . Indeed, in this case, the diagrammatic technique can be obtained in this case as a result of the expansion in a functional differential operator acting on the transition amplitude for the matter fields in the quadratic (free) approximation against the background of the external field sources. In this case, the square transition amplitude must be averaged

<sup>4</sup> Owing to constraints (7), the variables  $\{\Omega_\xi\}$  are insignificant in the problem under consideration.

<sup>5</sup> This is the case in theories on a regular lattice with action (1). When this condition for interaction of anomalous modes is violated, the notion of Wilson fermion doubling is likely meaningless.

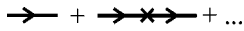


Fig. 3.

with a weight over the variables  $\{e_{\mathcal{E}}\}$  before the expansion in interaction.

It is necessary to obtain the propagator

$$\langle \Psi^{\mathcal{A}} \bar{\Psi}^{\mathcal{A}} \rangle_{e_{\mathcal{E}}} = \Psi^{\mathcal{A}(0)} \langle (-i\alpha^a \partial_a)^{-1} \rangle_{e_{\mathcal{E}}} \bar{\Psi}^{\mathcal{A}(0)} \quad (21)$$

that describes the propagation of anomalous modes. Thus, the problem is reduced to the study of the Green's function that corresponds to the operator on the left-hand side of Eq. (15) and is averaged over the variables  $\{e_{\mathcal{E}}\}$  by taking into account condition (20):<sup>6</sup>

$$\langle (-i\alpha^a \partial_a)^{-1} \rangle_{e_{\mathcal{E}}}. \quad (22)$$

5. We first consider the case  $\lambda = 0$ . To perform the necessary averaging in Eq. (22), we use the well-known formula

$$\mathcal{P} \frac{1}{\tau} = \frac{1}{2i} \int_0^{+\infty} ds [e^{is\tau} - e^{-is\tau}]. \quad (23)$$

This formula implies that  $\tau \neq 0$  or  $\tau^{-1} \neq \pm\infty$ . Using Eq. (23), we represent operator (22) (for the case  $\lambda = 0$  before averaging over the variables  $\{e_{\mathcal{E}}\}$ ) in the form

$$\langle x | (-i\beta^a \partial_a)^{-1} | y \rangle = \frac{1}{2i} \int_0^{+\infty} ds \langle x | [e^{s\beta^a \partial_a} - e^{-s\beta^a \partial_a}] | y \rangle. \quad (24)$$

This relation is meaningful for  $x \neq y$ , because its left-hand side is finite in this case. However, representation (24) is meaningless for  $x = y$ . Then, let us average the terms in the square brackets in Eq. (24) over the variables  $\{e_{\mathcal{E}}\}$ . In this case, it is only important that, owing to Eq. (20), the result of such averaging of each of these terms is a function of  $(\pm s)^2 = s^2$  but not of  $(\pm s)$ . Therefore, the terms in the square brackets in Eq. (24) cancel each other after the averaging over the variables  $\{e_{\mathcal{E}}\}$  and thereby the propagator describing the propagation of anomalous modes is proportional to the  $\delta$  function of the variable  $x$ :

$$\langle \langle x | (-i\beta^a \partial_a)^{-1} | y \rangle \rangle_{e_{\mathcal{E}}} \sim a \delta^{(4)}(x - y). \quad (25)$$

We remind the reader that  $a$  is a certain constant that has the length dimension and is on the order of the effective lattice step.

<sup>6</sup> It is necessary to point to a functional difference of this computational procedure from that used in problems of the localization of particles in random potentials. The physical difference between these situations is that the parameters characterizing the randomness of a potential in the latter case are not dynamical degrees of freedom, whereas the positions of the vertices of the complex are dynamical variables.

We now estimate quantity (22) for nonzero  $\lambda$  by taking into account that it can be expanded in the parameter  $\lambda$ . This problem is easily solved by using field theory methods. Figure 3 shows the sum of the diagrams that corresponds to quantity (22). The solid line and cross correspond to unperturbed propagator (25) and the operator  $i\lambda\rho^a\partial_a$ , respectively. Then, using the conventional diagrammatic technique rules, one can represent quantity (25) in the form of the series of diagrams shown in Fig. 3.

As a result, the  $\delta$  function of the free propagator is "smeared" and the desired propagator describing the propagation of anomalous modes appears to be exponentially decreasing in the  $x$  space:

$$\langle \langle \Psi^{\mathcal{A}}(x) \bar{\Psi}^{\mathcal{A}}(y) \rangle \rangle_{e_{\mathcal{E}}} \sim \exp\left[-\frac{|x-y|}{a\lambda}\right]. \quad (26)$$

At the same time, according to Eq. (11), as the distance increases, the free propagator describing the propagation of normal modes in the  $x$  representation decreases according to the power law

$$(i\gamma^a \partial_a)^{-1}(x, y) = \frac{\not{x} - \not{y}}{2\pi^2((x-y)^2)^2}. \quad (27)$$

Comparing Eqs. (26) and (27), we conclude that Wilson fermion doubling is absent in the theory under consideration even when the complex allows the existence of soft anomalous modes.

6. We briefly summarize the conclusions as follows.

(i) In [6, 7], simplicial complexes on which Wilson fermion doubling was absent, as well as complexes on which Wilson fermion doubling formally occurred, were presented.

(ii) On complexes that formally allow fermion doubling, this phenomenon is really absent because normal and anomalous fermion modes propagate differently in spacetime. Normal modes (in the long-wavelength limit) have definite energy and momentum. On the contrary, anomalous modes cannot have definite energy and momentum and their propagators decrease exponentially in spacetime at scales comparable with the characteristic lattice scale. Thus, the statements made in [6, 7] are significantly enhanced.

Certain general consequences of the above results are as follows.

Let us assume that one Weyl field is introduced on the lattice in case (ii) by introducing the projection operator  $(1/2)(1 \pm \gamma^5)$  into the fermion action in Eqs. (2) and (3). Since the lattice fermion action is invariant under global  $\gamma^5$  transformations and the lattice fermion measure is in addition invariant under local  $\gamma^5$  transformations, the total fermion current is strictly conserved. However, this does not mean that each of the currents of normal and anomalous modes is conserved separately. On the contrary, it has been well known for a long time that, when  $S$  matrix elements are calculated

by using causal Feynman propagators, the Weyl-field current is not conserved due to the gauge anomaly. This phenomenon is interpreted in the theory under consideration as the mutual transfer of the axial charge between normal and anomalous modes.

We also emphasize that the theory under consideration does not exclude the case where the axial charges of normal and anomalous modes are conserved separately (see [7]). This means that the axial anomaly is absent. Such a regime can be realized only in problems where the use of Feynman propagators is incorrect, for example, at the universe inflation stage when the problem of the  $S$  matrix is meaningless.

This work was supported by the Russian Foundation for Basic Research (project no. 04-02-16970) and by the Council of the President of the Russian Federation for Support of Young Scientists and Leading Scientific Schools (project no. NSh-2044.2003.2 for Belavin's scientific school).

## REFERENCES

1. K. G. Wilson, Erice Lecture Notes (1975).
2. J. Kogut and L. Susskind, Phys. Rev. D **11**, 395 (1975).
3. L. Susskind, Phys. Rev. D **16**, 3031 (1977).
4. M. Lüscher, hep-th/0102028.
5. H. B. Nielsen and M. Ninomiya, Nucl. Phys. B **185**, 20 (1981); Nucl. Phys. B **193**, 173 (1981).
6. S. N. Vergeles, Pis'ma Zh. Éksp. Teor. Fiz. **76**, 3 (2002) [JETP Lett. **76**, 1 (2002)].
7. S. N. Vergeles, Zh. Éksp. Teor. Fiz. **124**, 1203 (2003) [JETP **97**, 1075 (2003)].
8. S. N. Vergeles, Zh. Éksp. Teor. Fiz. **120**, 1069 (2001) [JETP **93**, 926 (2001)].
9. S. N. Vergeles, hep-th/0411096.

*Translated by R. Tyapaev*

# Hydraulic Jump as a White Hole<sup>†</sup>

G. E. Volovik

*Low Temperature Laboratory, Helsinki University of Technology, FIN-02015 HUT, Finland*  
*Landau Institute for Theoretical Physics, Moscow, 119334 Russia*

Received October 24, 2005

In the geometry of the circular hydraulic jump, the velocity of the liquid in the interior region exceeds the speed of the capillary-gravity waves (ripples), whose spectrum is “relativistic” in the shallow water limit. The velocity flow is radial and outward, and thus the relativistic ripples cannot propagate into the interior region. In terms of the effective  $2 + 1$  dimensional Painlevé–Gullstrand metric appropriate for the propagating ripples, the interior region imitates a white hole. The hydraulic jump represents the physical singularity at the white-hole horizon. The instability of the vacuum in the ergoregion inside the circular hydraulic jump and its observation in recent experiments on superfluid  $^4\text{He}$  by Rolley *et al.* [3] are discussed. © 2005 Pleiades Publishing, Inc.

PACS numbers: 04.70.–s, 67.40.Hf

## 1. INTRODUCTION

Starting with the pioneering acoustic black hole [1], there appeared many suggestions to simulate the black and white holes in various laboratory systems (see review paper [2] and the references therein). Here, we discuss the most perspective analog, which has been actually realized in recent experiments with superfluid  $^4\text{He}$  [3]: the circular hydraulic jump in superfluid  $^4\text{He}$  simulates the  $2 + 1$  dimensional white hole for the surface waves with a “relativistic” spectrum in the shallow liquid.

In Section 2, we discuss the effective space–time emerging for the surface waves—ripples—in the shallow water limit. In Section 3, we introduce the interaction of ripples with the walls. The walls provide the absolute reference frame. In the region where the flow of the liquid with respect to this frame exceeds the Landau critical velocity for ripplon radiation, the surface of the liquid becomes unstable. For the relativistic ripples, the boundary of this region serves as an analog of a black-hole or white-hole horizon. The instability of the liquid towards generation of ripples inside the horizon is the main mechanism of the decay of this  $2 + 1$  dimensional analog of a black or white hole. Similar instability of the vacuum inside an astronomical black hole is possible. In Section 4, we show that the hydraulic jump is the realization of the white hole horizon for the relativistic ripples in normal liquids. In Section 5, the discussion is extended for the hydraulic jump in superfluids in relation to the recent experiment [3]. Some open questions require further investigations.

## 2. EFFECTIVE METRIC FOR RIPPLONS

The general dispersion relation  $\omega(\mathbf{k})$  for ripples—the waves on the surface of a liquid—is

$$M(k)(\omega - \mathbf{k} \cdot \mathbf{v})^2 = \rho g + k^2 \sigma. \quad (1)$$

Here,  $\sigma$  is the surface tension,  $\rho$  is mass density of the liquids,  $\rho g$  is the gravity force, and  $\mathbf{v}$  is the velocity of the liquid along the surface. The quantity  $M(k)$  is the  $k$ -dependent mass of the liquid that is forced into motion by the oscillating surface:

$$M(k) = \frac{\rho}{k \tanh kh}, \quad (2)$$

where  $h$  is the thicknesses of the layer of the liquid.

The spectrum (1) becomes “relativistic” in the shallow water limit  $kh \ll 1$ ,  $k \ll k_0$ :

$$(\omega - \mathbf{k} \cdot \mathbf{v})^2 = c^2 k^2 + c^2 k^4 \left( \frac{1}{k_0^2} - \frac{1}{3} h^2 \right), \quad (3)$$

$$c^2 = gh, \quad k_0^2 = \rho g / \sigma.$$

If the  $k^4$  corrections are ignored, the spectrum of ripples in the  $k \rightarrow 0$  limit is described by the effective metric [4]

$$g^{\mu\nu} k_\mu k_\nu = 0, \quad k_\mu = (-\omega, k_x, k_y), \quad (4)$$

with the following elements

$$g^{00} = -1, \quad g^{0i} = -v^i, \quad g^{ij} = c^2 \delta^{ij} - v^i v^j. \quad (5)$$

The interval describing the effective  $2 + 1$  space–time in which ripples propagate along geodesics and the

<sup>†</sup>The text was submitted by the author in English.

corresponding covariant components of the effective metric are

$$ds^2 = g_{\mu\nu} dx^\mu dx^\nu, \quad g_{00} = -1 + \frac{v^2}{c^2}, \quad (6)$$

$$g_{0i} = -\frac{v^i}{c}, \quad g_{ij} = \frac{1}{c^2} \delta_{ij}.$$

As distinct from the original acoustic metric introduced by Unruh [1], here  $c$  is the speed of gravity waves. It is typically much smaller than the speed of sound, which allows us to avoid the different hydrodynamic instabilities inherent to the acoustic analogs of the horizon.

The spectrum (1) is valid for the perfect fluid, where dissipation due to friction and viscosity is neglected, and it must be modified when the dissipation is added. For the ripples propagating at the interface between two superfluids, the dissipation leads to a simple extra term on the right-hand side of Eq. (1) [5, 6]:

$$M(k)(\omega - \mathbf{k} \cdot \mathbf{v})^2 = \rho g + k^2 \sigma - i\Gamma \omega. \quad (7)$$

For the ripples at the interface between  ${}^3\text{He-A}$  and  ${}^3\text{He-B}$ , the friction parameter  $\Gamma > 0$  depends on the temperature and is proportional to  $T^3$  at low  $T$ . The important property of the added dissipative term is that it introduces the reference frame of the horizontal wall. The  $\omega$ -dependence of the dissipative term in Eq. (7), which has no Doppler shift, implies that this spectrum is written in the frame of the wall. We may expect that, under some conditions, this description is applicable to the normal viscous liquid, where the phenomenological parameter  $\Gamma$  is determined by the Reynolds number of the flowing liquid and probably depends on  $\omega$  and  $k$ .

### 3. INSTABILITY IN THE ERGOREGION

If the non-zero  $\Gamma$  is taken into account, from the spectrum  $\omega(k)$  in Eq. (7), it follows that the instability to the formation of the surface waves occurs when the velocity  $v$  of the flow with respect to the wall exceeds the critical velocity  $v_L$ . At  $v = v_L$ , the imaginary part  $\text{Im} \omega(k_c)$  of the energy spectrum of the critical ripplon with momentum  $k_c$  crosses zero and becomes positive; i.e., the attenuation of ripples at  $v < v_L$  due to dissipation transforms to amplification at  $v > v_L$  [5, 6]. The critical velocity  $v_L$  and the momentum of the critical ripplon  $k_c$  do not depend on the friction parameter  $\Gamma$ . They are different in the “relativistic” and “non-relativistic” regimes:

$$v_L = c, \quad k_c = 0, \quad \text{if } hk_0 < \sqrt{3}, \quad (8)$$

$$v_L = c\sqrt{2/hk_0}, \quad k_c = k_0, \quad \text{if } hk_0 \gg 1. \quad (9)$$

In both regimes, the frequency of the critical ripplon is  $\omega(k_c) = 0$ ; i.e., the critical ripplon must be stationary in the wall frame.

The fact that the threshold velocity  $v_L$  does not depend on  $\Gamma$  demonstrates that the main role of the dissipative term is to provide the reference frame of the wall with which the liquid interacts. The flow of a superfluid liquid with respect to this reference frame does not experience any dissipation if its velocity is below  $v_L$ . The dissipation starts above the instability threshold when the surface of the liquid is perturbed; i.e., ripples are radiated due to the interaction of the liquid with the wall. This indicates that the critical velocity of the flow with respect to the wall coincides with the Landau criterion for ripplon nucleation:

$$v_L = \min_k \frac{E(k)}{k}, \quad E(k) = \sqrt{(\rho g + \sigma k^2)/M(k)}. \quad (10)$$

In the case of the interface between  ${}^3\text{He-A}$  and  ${}^3\text{He-B}$ , the critical velocity of instability towards the growth of the critical ripplon has been measured in the nonrelativistic deep-water regime  $hk_0 \gg 1$  [7], and has been found in good agreement with the theoretical estimate of the Landau velocity (modified for the case of two liquids [5, 6]) without any fitting parameter.

The region where the flow velocity  $v$  exceeds  $v_L$  represents the ergoregion, since, in the wall frame, the energy of the critical ripplon is negative in this region,  $E(k) + \mathbf{k} \cdot \mathbf{v} < 0$ . For the relativistic ripples, the ergoregion—the region where  $v$  exceeds  $c$ —is expressed in terms of the effective metric in Eq. (6): in the ergoregion the metric element  $g_{00}$  changes sign and becomes positive. If the flow is perpendicular to the ergosurface (the boundary of the ergoregion), then the ergosurface serves as the event horizon for ripples. It is the black hole horizon if the liquid moves into the ergoregion, since ripples cannot escape from the ergoregion (if the nonrelativistic  $k^4$  corrections to the spectrum are ignored). Correspondingly, if the liquid moves from the ergoregion, the boundary of the ergoregion represents the white hole horizon.

The discussed instability of the flow towards formation of ripples in the supercritical region does not depend on whether the horizon is of a black hole or of a white hole. This mechanism also does not resolve between the ergosurface and the horizon. The instability comes from the interaction with the fixed reference frame and occurs in the region where the energy of the critical fluctuation is negative in this frame. Such a kind of instability is also called the Miles instability [8]. In principle, the Miles instability may take place behind the horizon of the astronomical black holes if there exists the fundamental reference frame related for example with Planck physics [5, 8]. It may lead to the decay of the black hole much faster than the decay due to Hawking radiation.

#### 4. WHITE-HOLE HORIZON IN THE HYDRAULIC JUMP

The situation with a white hole horizon is achieved in the so-called hydraulic jump first discussed by Rayleigh in terms of the shock wave [9]. The circular hydraulic jump occurs when the vertical jet of liquid falls on a flat horizontal surface. The flow of the liquid at the surface exhibits a ring discontinuity at a certain distance  $r = R$  from the jet (observation of noncircular hydraulic jumps with sharp corners has been reported in [10]). At  $r = R$  there is an abrupt increase in the depth  $h$  of the liquid (typically by an order of magnitude) and correspondingly a decrease in the radial velocity of the liquid. The velocity of the liquid in the interior region ( $r < R$ ) exceeds the speed of “light” for ripples  $v > c = \sqrt{hg}$ , while outside the hydraulic jump ( $r > R$ ) one has  $v < c = \sqrt{hg}$ . Since the velocity flow is radial and outward, the interior region imitates the “white-hole” region. The interval of the 2 + 1 dimensional effective space–time in which the “relativistic” ripples “live” is

$$ds^2 = -c^2 dt^2 + (dr - v(r)dt)^2 + r^2 d\phi^2. \quad (11)$$

The similar 3 + 1 dimensional space–time in general relativity, the so-called Painlevé–Gullstrand metric [11]

$$ds^2 = -c^2 dt^2 + (dr - v(r)dt)^2 + r^2 (d\theta^2 + \sin^2 \theta d\phi^2), \quad (12)$$

$$v^2(r) = \frac{2GM}{r},$$

is popular now in black hole physics (see [12] and the references therein).

In general relativity, the metric is continuous across the horizon. In our case, there is a real physical singularity at the white-hole horizon—the jump in the effective metric (6). However, the discussed mechanism of the Miles instability in the ergoregion (or behind the horizon) does not depend on whether the horizon, or ergosurface, is smooth or singular.

A similar condensed matter analog of the black-hole horizon with the physical singularity at the horizon has been also been discussed by Vachaspati [13]. At the boundary between two superfluids, the speed of sound (and, thus, the acoustic metric) has a jump:  $c_1 \neq c_2$ . The acoustic black or white horizon occurs if the superfluid velocity of the flow through the phase boundary is subsonic in one of the superfluids but supersonic in the other one:  $c_1 < v < c_2$ .

#### 5. HYDRAULIC JUMP IN SUPERFLUIDS

The analogy between the instability of the surface inside the hydraulic jump and the instability of the vacuum behind the horizon can be useful only if the liquid simulates a quantum vacuum. For that, the liquid must be quantum, and its flow should not exhibit any friction in the absence of a horizon. That is why the full analogy could occur if one uses either a flow of quantum liquid

with a high Reynolds number, or a superfluid liquid that has no viscosity. Quantum liquids such as superfluid or normal  $^3\text{He}$  and  $^4\text{He}$  are good candidates.

The first observation of the circular hydraulic jump in superfluid liquid (superfluid  $^4\text{He}$ ) was reported in [3]. The surface waves generated in the ergoregion (in the region inside the jump) were observed. The critical ripplon appeared to be stationary in the wall frame in agreement with the Miles instability towards ripplon radiation inside the ergoregion discussed in Section 3. This is the first experiment where the analog of the instability of the vacuum inside the horizon has been simulated. The growths of the critical ripplon is saturated due to the nonlinear effects, and then the whole pattern remains stationary (though not static). This is different from the case of the instability observed at the interface between  $^3\text{He-A}$  and  $^3\text{He-B}$ , where the instability is not saturated and leads to the crucial rearrangement of the vacuum state: Quantized vortices penetrate into the  $^3\text{He-B}$  side from the  $^3\text{He-A}$ , they partially screen the  $^3\text{He-B}$  flow and reduce its velocity back below the threshold for the ripplon formation [7].

Under the conditions of experiment [3], the hydraulic jump in the superfluid  $^4\text{He}$  is very similar to that in the normal liquid  $^4\text{He}$ . The position  $R$  of the hydraulic jump as a function of the temperature does not experience discontinuity at the superfluid transition. This suggests that quantized vortices are formed that provide mutual friction between the superfluid and normal components. As a result, even below the  $\lambda$  point, the liquid moves as a whole, though with a lower viscosity because of the reduced fraction of the normal component.

To avoid the effect of the normal component, it would be desirable to reduce the temperature or to conduct similar experiments in a shallow superfluid  $^3\text{He}$ .

The advantage of superfluid  $^3\text{He}$  is that, as distinct from superfluid  $^4\text{He}$ , vortices are not easily formed there: the energy barrier for vortex nucleation in  $^3\text{He-B}$  is about  $10^6$  times bigger than the temperature [14]. In addition, in superfluid  $^3\text{He}$ , the normal component of the liquid is very viscous compared to that in superfluid  $^4\text{He}$ . In the normal state, the kinematic viscosity is  $\nu \sim 10^{-4} \text{ cm}^2/\text{s}$  in liquid  $^4\text{He}$ , and  $\nu \sim 1 \text{ cm}^2/\text{s}$  in liquid  $^3\text{He}$ . That is why in many practical arrangements the normal component in superfluid  $^3\text{He}$  remains at rest with respect to the reference frame of the wall and, thus, does not produce any dissipation if the flow of the superfluid component is subcritical. One can also exploit thin films of a superfluid liquid where the normal component is fixed. The ripples there represent the so-called third sound (recent discussion on the third sound propagating in superfluid  $^3\text{He}$  films can be found in [15]). In 1999, Seamus Davis suggested using the third sound in superfluid  $^3\text{He}$  for simulation of the horizons [16].

In normal liquids, it is the viscosity that determines the position  $R$  of the hydraulic jump (see [17, 18]). The open question is what is the dissipation mechanism that determines the position  $R$  of the white-hole horizon in a superfluid flow with a stationary or absent normal component when its viscosity is effectively switched off. Since there is no dissipation of the superfluid flow if its velocity is below  $v_L$ , one may expect that the same mechanism, which is responsible for dissipation in the presence of the horizon, also determines the position  $R$  of the horizon. If so, the measurement of  $R$  as function of the parameters of the system will give the information on various mechanisms of decay of a white hole. If the Miles vacuum instability towards ripplon radiation inside the horizon is saturated as in experiment [3], another mechanisms will intervene such as the black-hole laser [19], and even the quantum mechanical Hawking radiation of riplons. The latter should be enhanced at the sharp discontinuous horizon of the hydraulic jump and maybe near the sharp corners of the noncircular (polygonal) hydraulic jump observed in [10].

It is also unclear whether it is possible to approach the limit of a smooth horizon without the shock wave of the hydraulic jump and whether it is possible to construct the inward flow of a liquid that would serve as an analog of the black hole horizon.

I thank Etienne Rolley and Michael Pettersen who sent me their experimental results prior to publication and Marc Rabaud and Tomas Bohr for discussions. This work was supported in part by the Council of the President of the Russian Federation for Support of Young Scientists and Leading Scientific Schools (project no. NSh-2338.2003.2 for Starobinsky's scientific school), and by the European Science Foundation (COSLAB Program).

## REFERENCES

1. W. G. Unruh, Phys. Rev. Lett. **46**, 1351 (1981).
2. C. Barcelo, S. Liberati, and M. Visser, gr-qc/0505065.
3. E. Rolley, C. Guthmann, M. S. Pettersen, and C. Chevalier, in *Proceedings of the 24th Conference on Low Temperature Physics* (in press); physics/0508200.
4. R. Schützhold and W. G. Unruh, Phys. Rev. D **66**, 044019 (2002).
5. G. E. Volovik, *The Universe in a Helium Droplet* (Clarendon, Oxford, 2003).
6. G. E. Volovik, JETP Lett. **75**, 418 (2002); cond-mat/0202445; JETP Lett. **76**, 240 (2002); gr-qc/0208020.
7. R. Blaauwgeers, V. B. Eltsov, G. Eska, *et al.*, Phys. Rev. Lett. **89**, 155301 (2002).
8. R. Schützhold and W. G. Unruh, Phys. Rev. Lett. **95**, 031301 (2005).
9. L. Rayleigh, Proc. R. Soc. London, Ser. A **90**, 324 (1914).
10. C. Ellegaard, A. E. Hansen, A. Haaning, *et al.*, Nature **392**, 767 (1998); Nonlinearity **12**, 1 (1999).
11. P. Painlevé, C. R. Acad. Sci. **173**, 677 (1921); A. Gullstrand, Ark. Mat., Astron. Fys. **16** (8), 1 (1922).
12. A. J. S. Hamilton and J. P. Lisle, gr-qc/0411060; M. Visser and A. Nielsen, gr-qc/0510083.
13. T. Vachaspati, J. Low Temp. Phys. **136**, 361 (2004).
14. Ü. Parts, V. M. H. Ruutu, J. H. Koivuniemi, *et al.*, Europhys. Lett. **31**, 449 (1995).
15. A. Vorontsov and J. A. Sauls, J. Low Temp. Phys. **134**, 1001 (2004); cond-mat/0309599.
16. Seamus Davis, private communication at *NEDO 2nd International Workshop on Quantum Fluids and Solids* (Hawaii, 1999).
17. T. Bohr, P. Dimon, and V. Putkaradge, J. Fluid Mech. **254**, 635 (1993); T. Bohr, C. Ellegaard, A. E. Hansen, and A. Haaning, Physica B (Amsterdam) **228**, 1 (1996).
18. S. B. Singha, J. K. Bhattacharjee, and A. K. Ray, cond-mat/0508388.
19. S. Corley and T. Jacobson, Phys. Rev. D **59**, 124011 (1999).

# Parton Distribution Functions from the Precise NNLO QCD Fit<sup>†</sup>

S. I. Alekhin

*Institute for High Energy Physics, Protvino, Moscow region, 142281 Russia*

Received October 6, 2005

We report on the parton distribution functions (PDFs) determined from the NNLO QCD analysis of the world inclusive DIS data with account for the precise NNLO QCD corrections to the evolution equations kernel. The value of the strong coupling constant  $\alpha_s^{\text{NNLO}}(M_Z) = 0.1141 \pm 0.0014$  (exp.), in fair agreement with the one obtained using the earlier approximate NNLO kernel by van Neerven-Vogt. The intermediate bosons rates calculated in the NNLO using the obtained PDFs are in agreement with the latest Run II results. © 2005 Pleiades Publishing, Inc.

PACS numbers: 06.20.Jr, 12.38.Bx, 13.60.Hb

The inclusion of the higher-order QCD corrections for most of the high-energy processes is important due to the value of the strong coupling constant  $\alpha_s$  that is not small for realistic kinematics. This is also true for the deep-inelastic lepton-nucleon scattering (DIS) process, which provides valuable information about the structure of the nucleon. However, since the next-to-next-to-leading order (NNLO) corrections were completely calculated only lately, most often the analysis of the DIS data was performed in the next-to-leading (NLO) approximation or, at best, with the approximate NNLO evolution kernels derived in [1] on the basis of calculations [2, 3]. With the recently calculated exact expressions for the NNLO evolution kernels [4] one can improve the available extractions of the NNLO parton distribution functions (PDFs) based on the approximate evolution kernels by getting rid of the error due to the kernel uncertainty. Even so, consistent extraction of the NNLO PDFs from the global fits including the jet production data [5] is still unfeasible since the NNLO coefficient functions for the jet production process are not completely calculated. In this letter, we describe the NNLO PDFs obtained from the updated analysis of the world data on inclusive DIS process [6], where the NNLO coefficient functions are known and full account of the NNLO corrections is possible.

We use for the analysis the charged-leptons proton/deuteron data on the DIS cross sections collected in the SLAC-CERN-HERA experiments [7] with the cuts  $Q^2 > 2.5 \text{ GeV}^2$ ,  $W > 1.8 \text{ GeV}$ , and  $x < 0.75$  imposed in order to reject the kinematical regions problematic for the perturbative QCD (pQCD) and where the nuclear corrections are particularly big. The HERA data with  $Q^2 > 300 \text{ GeV}^2$  were also cut off since they have a marginal impact on the precision of the PDFs obtained but complicate the analysis due to account of the  $Z$  boson

contribution being required for these kinematics. The pQCD evolution input for the  $u$ -,  $d$ -,  $s$ -quarks and gluons at  $Q_0^2 = 9 \text{ GeV}^2$  is

$$xu_V(x, Q_0) = \frac{2}{N_V} x^{a_u} (1-x)^{b_u} (1 + \gamma_2^u x), \quad (1)$$

$$xu_S(x, Q_0) = \frac{A_S}{N_S} \eta_u x^{a_s} (1-x)^{b_{su}}, \quad (2)$$

$$xd_V(x, Q_0) = \frac{1}{N_V^d} x^{a_d} (1-x)^{b_d}, \quad (3)$$

$$xd_S(x, Q_0) = \frac{A_S}{N_S^d} x^{a_s} (1-x)^{b_{sd}}, \quad (4)$$

$$xs_S(x, Q_0) = \frac{A_S}{N_S^s} \eta_s x^{a_s} (1-x)^{(b_{su} + b_{sd})/2}, \quad (5)$$

$$xG(x, Q_0) = A_G x^{a_G} (1-x)^{b_G} (1 + \gamma_1^G \sqrt{x} + \gamma_2^G x), \quad (6)$$

where the indices  $V$  and  $S$  correspond to the valence and sea distributions correspondingly. The normalization factors  $N_{u,d}^V$  and  $A_G$  are calculated from other parameters using the fermion number and momentum conservation. The value of the parameter  $N_S$  is defined from the condition that  $A_S$  gives the total momentum carried by the sea quarks. The value of  $\eta_s$  is fixed at 0.42. For the PDFs parameters obtained in our fit, this choice provides the value of the strange sea suppression factor equal to 0.41 at  $Q_0^2 = 20 \text{ GeV}^2$ , in agreement with the CCFR/NuTeV analysis of [8]. The  $b$ - and  $c$ -quarks contributions are accounted for in the massive scheme with the  $O(\alpha_s^2)$  correction of [9] included. For the lowest  $Q/W$  data used in the fit, the power corrections are

<sup>†</sup>The text was submitted by the author in English.

important, and, therefore, we take into account the target-mass correction by Georgi-Politzer [10] and the dynamical twist-4 terms in the structure functions  $F_{2,T}$  parameterized in a model-independent way as the piece-linear functions of  $x$ .

The parameters of the PDFs obtained in the NNLO fit with their errors due to the statistical and systematical uncertainties in the data that are given in Table 1. These PDFs are comparable to the ones in [6] extracted using the approximate NNLO kernel within the errors due to the NNLO kernel uncertainty estimated in [1]. However, at small  $x$  and  $Q$ , where the NNLO corrections are enhanced, the impact of the new calculations is nonnegligible. With the exact NNLO corrections, the QCD evolution of the gluon distribution at small  $x$  gets weaker and as a result, at small  $x/Q$ , the gluon distribution obtained using the precise NNLO kernel is quite different from the approximate one. In particular, while the approximate NNLO gluon distribution is negative at  $Q^2 < 1.3 \text{ GeV}^2$ , the precise one remains positive even below  $Q^2 = 1 \text{ GeV}^2$  (see Fig. 1). For the NLO case, the positivity of the gluons at small  $x/Q$  is even worse than for the approximate NNLO case due to the approximate NNLO corrections that dampen the gluon evolution at small  $x$  too; therefore, the account of the NNLO corrections is crucial in this respect (cf. discussion of [11]). The positivity of the PDFs is not mandatory beyond the leading order; however, it allows probabilistic interpretation of the parton model and facilitates modeling of the soft processes, such as the underlying events in the hadron-hadron collisions at high energies. The change of the gluon distribution at small  $x/Q$  as compared to the fit with the approximate NNLO evolution is rather due to the change in the evolution of the kernel than due to the shift in the fitted parameters of the PDFs. This is clear from the comparison of the exact NNLO gluon distribution to one obtained from the approximate NNLO fit and evolved to low  $Q$  using the exact NNLO kernel (see Fig. 1). In the vicinity of the crossover of the gluon distribution to the negative values, its relative change due to the variation of the evolution kernel is quite big and, therefore, the further fixation of the kernel at small  $x$  discussed in [12] can be substantial for the low  $Q$  limit of the PDFs.

For the higher-mass kinematics at the LHC numerical impact of the NNLO, the kernel update is not dramatic. The change in the Higgs and  $W/Z$  boson production cross sections due to the more precise definition of the NNLO PDFs is comparable to the errors coming from the PDFs uncertainties. The NNLO predictions for the longitudinal DIS structure function  $F_L$  at  $x \sim 10^{-5}$  measured by the  $H1$  collaboration [13] also does not change too much since they are given by the Mellin convolution of PDFs with the coefficient functions and are defined by the gluon distribution at relatively big

**Table 1.** The PDFs parameters and  $\chi^2/\text{NDP}$  obtained in the fit. The errors in the parameters are obtained by propagation of the statistical and systematical errors in the data

Valence quarks:	$a_u$	$0.724 \pm 0.027$
	$b_u$	$4.0194 \pm 0.050$
	$\gamma_2^u$	$1.04 \pm 0.35$
	$a_d$	$0.775 \pm 0.073$
	$b_d$	$5.15 \pm 0.15$
Gluon:	$a_G$	$-0.118 \pm 0.021$
	$b_G$	$9.6 \pm 1.2$
	$\gamma_1^G$	$-3.83 \pm 0.51$
	$\gamma_2^G$	$8.4 \pm 1.7$
Sea quarks:	$A_S$	$0.1586 \pm 0.0089$
	$a_s$	$-0.2094 \pm 0.0044$
	$b_{sd}$	$5.6 \pm 1.2$
	$\eta_u$	$1.12 \pm 0.11$
	$b_{su}$	$10.39 \pm 0.88$
$\chi^2/\text{NDP}$		$2534/2274$

values of  $x$ . The obtained value of the strong coupling constant

$$\alpha_s^{\text{NNLO}}(M_Z) = 0.1141 \pm 0.0014(\text{stat} + \text{syst}),$$

is in fair agreement with  $\alpha_s^{\text{NNLO}}(M_Z) = 0.1143 \pm 0.0014$  (stat + syst) obtained in the fit of [6] with the approxi-

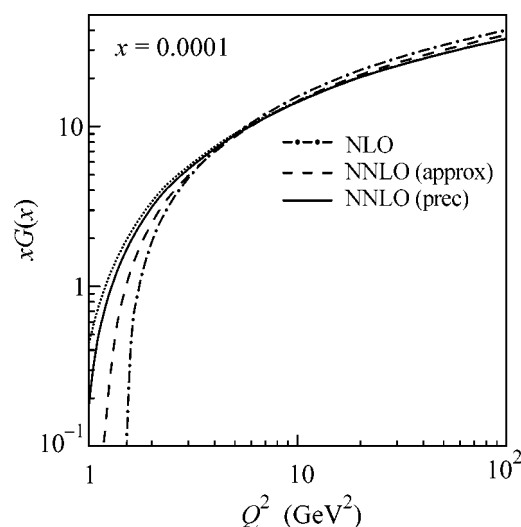


**Fig. 1.** The gluon distributions obtained in the different variants of the analysis (solid: the fit with the exact NNLO evolution; dashes: the fit with approximate NNLO evolution; dots: the approximate NNLO gluons evolved with the exact NNLO kernel; dashed-dots: the NLO fit).

**Table 2.** The NNLO inclusive rates (in nb) for the intermediate bosons production in the hadron–hadron collisions. The errors are due to the total PDFs uncertainties

	$W^\pm$	$Z$
$\bar{p}p$ (1.96 TeV)	$26.11 \pm 0.44$	$7.78 \pm 0.11$
$pp$ (14 TeV)	$197.0 \pm 5.3$	$57.7 \pm 1.5$

mate NNLO kernel and with the results of the exact NNLO analysis of the nonsinglet DIS data [14].

The errors in the PDFs parameters given in Table 1 are calculated as a propagation of the experimental errors for the data points used in the fit. We calculate these errors using the covariance matrix method [15] taking into account the statistical and systematic errors in the data and the correlations of the latter as well. We also take into account the theoretical errors due to the possible variations of the strange suppression factor  $\eta_s$  and the  $c$  quark mass  $m_c$ . For this purpose, we recalculate the error matrix for the PDF parameters with  $\eta_s$  and  $m_c$  released. Since the parameters  $\eta_s$  and  $m_c$  are not constraint by the charged-leptons inclusive DIS data, we confine their variation adding to the data sample two “measurements”:  $\eta_s = 0.42 \pm 0.1$  and  $m_c = 1.5 \pm 0.25$  GeV with the errors in these measurements representing our current understanding of the uncertainties in these parameters. In this approach, the theoretical

errors are included into the total error in the PDFs and their correlations with other sources of the PDFs uncertainties are automatically taken into account. The NNLO PDFs grid for the range of  $Q^2 = 0.8\text{--}2 \times 10^8$  GeV<sup>2</sup> and  $x = 10^{-7}\text{--}1$  with the total uncertainties in the PDFs supplied is available directly<sup>1</sup> and through the LHAPDF library.<sup>2</sup> The LO and NLO PDFs grids are also supplied to provide a tool for checking the sensitivity of different calculations to the QCD order of the PDFs.

The NNLO inclusive rates for the intermediate boson production at the FNAL  $\bar{p}p$  collider and the LHC calculated using this grid and the code of [16] with the corrections of [17] are given in Table 2. The masses and widths of the  $W/Z$  bosons were set as  $M_W = 80.425$  GeV,  $M_Z = 91.188$  GeV,  $\Gamma_W = 2.124$  GeV,  $\Gamma_Z = 2.495$  GeV, and the squared sine of the Weinberg angle  $x_W(M_Z) = 0.2312$ , and the squared cosine of the Cabibbo angle  $c_C = 0.9498$  [18]. The errors quoted in Table 2 are due to the total uncertainty in the PDFs including the theoretical errors considered. The calculations are in agreement with the latest run II results of [19] within the errors (see Fig. 2). The errors in the data of run II are bigger than the ones in the calculations; therefore, the latter can be used for better calibration of the luminosity, which gives the main contribution to the measurements error.

In summary, we provide an update of the analysis of the world DIS inclusive data on the proton/deuteron targets with full account of the NNLO QCD corrections including the recent calculations of the exact NNLO evolution kernel. The value of  $\alpha_s$  is in fair agreement with the earlier version of the fit based on the approximate NNLO kernels. With the exact NNLO corrections applied, we observe improvement in the positivity of the gluon distributions extrapolated to small  $x$  and  $Q$ : Now we have gluons positive up to  $Q = 1$  GeV, i.e., throughout kinematical region where the parton model is applicable. The NNLO  $W/Z$ -bosons rates calculated using the PDFs obtained are in agreement with the recent run II results and can be used for better calibration of the Fermilab experiments in view of the uncertainty in the calculations due to PDFs that are smaller than the experimental ones. Since these PDFs are extracted from the data for one single process, they can be used for the quantitative studies of the PDFs universally, which is an advantage as compared to the ones determined from the global fits.

## ACKNOWLEDGMENTS

I am indebted to S. Forte, S. Moch, R. Petri, and A. Vogt for stimulating discussions and to S. Kulagin for development of the Mathematica package for access to the PDFs grid. This work was supported by the Rus-

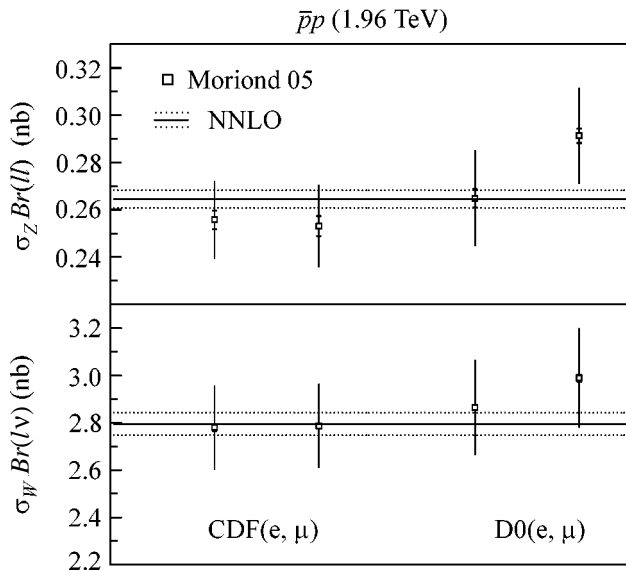


**Fig. 2.** The NNLO calculation of the  $W/Z$  rates for run II at Fermilab compared to the data. The dotted lines give the uncertainty in the calculations due to errors in the PDFs; the error bars of the data points give the total error including the one due to the luminosity uncertainty. The branching ratios of the  $W/Z$  lepton decays  $Br(W \rightarrow l\nu) = 0.107$  and  $Br(Z \rightarrow ll) = 0.034$  were applied.

<sup>1</sup> <http://sirius.ihep.su/~alekhin/pdfa02>

<sup>2</sup> <http://durpdg.dur.ac.uk/lhapdf/>

sian Foundation for Basic Research (project no. 03-02-17177) and by the Council of the President of the Russian Federation for Support of Young Scientists and Leading Scientific Schools (project no. NSh-1695.2003.2 for Zaitsev's Scientific School).

## REFERENCES

1. W. L. van Neerven and A. Vogt, Phys. Lett. B **490**, 111 (2000); hep-ph/0007362.
2. A. Retey and J. A. Vermaseren, Nucl. Phys. B **604**, 281 (2001); hep-ph/0007294; S. A. Larin, P. Nogueira, T. van Ritbergen, and J. A. M. Vermaseren, Nucl. Phys. B **492**, 338 (1997); hep-ph/9605317.
3. S. Catani and F. Hautmann, Nucl. Phys. B **427**, 475 (1994); hep-ph/9405388.
4. S. Moch, J. A. M. Vermaseren, and A. Vogt, Nucl. Phys. B **688**, 101 (2004); hep-ph/0403192; A. Vogt, S. Moch, and J. A. M. Vermaseren, Nucl. Phys. B **691**, 129 (2004); hep-ph/0404111.
5. A. D. Martin, R. G. Roberts, W. J. Stirling, and R. S. Thorne, Phys. Lett. B **604**, 61 (2004); hep-ph/0410230.
6. S. Alekhin, Phys. Rev. D **68**, 014002 (2003); hep-ph/0211096.
7. L. W. Whitlow, E. M. Riordan, S. Dasu, *et al.*, Phys. Lett. B **282**, 475 (1992); A. C. Benvenuti *et al.* (BCDMS Collab.), Phys. Lett. B **223**, 485 (1989); A. C. Benvenuti *et al.* (BCDMS Collab.), Phys. Lett. B **237**, 592 (1990); M. Arneodo *et al.* (New Muon Collab.), Nucl. Phys. B **483**, 3 (1997); hep-ph/9610231; C. Adloff *et al.* (H1 Collab.), Eur. Phys. J. C **21**, 33 (2001); hep-ex/0012053; S. Chekanov *et al.* (ZEUS Collab.), Eur. Phys. J. C **21**, 443 (2001); hep-ex/0105090.
8. M. Goncharov *et al.* (NuTeV Collab.), Phys. Rev. D **64**, 112006 (2001); hep-ex/0102049.
9. E. Laenen, S. Riemersma, J. Smith, and W. L. van Neerven, Nucl. Phys. B **392**, 229 (1993).
10. H. Georgi and H. D. Politzer, Phys. Rev. D **14**, 1829 (1976).
11. J. Huston, J. Pumplin, D. Stump, and W. K. Tung, hep-ph/0502080.
12. G. Altarelli, R. D. Ball, and S. Forte, Nucl. Phys. B **674**, 459 (2003); hep-ph/0306156.
13. E. M. Lobodzinska, hep-ph/0311180.
14. J. Blumlein, H. Bottcher, and A. Guffanti, Nucl. Phys., Proc. Suppl. **135**, 152 (2004); hep-ph/0407089.
15. S. I. Alekhin, hep-ex/0005042.
16. R. Hamberg, W. L. van Neerven, and T. Matsuura, Nucl. Phys. B **359**, 343 (1991); Nucl. Phys. B **644**, 403(E) (2002).
17. R. V. Harlander and W. B. Kilgore, Phys. Rev. Lett. **88**, 201801 (2002); hep-ph/0201206.
18. S. Eidelman *et al.* (Particle Data Group), Phys. Lett. B **592**, 1 (2004).
19. A. M. Bellavance (D0-Run II Collab.), hep-ex/0506025.

## Features of Dusty Structures in the Upper Earth's Atmosphere

B. A. Klumov<sup>a</sup>, S. V. Vladimirov<sup>b</sup>, and G. E. Morfill<sup>a</sup>

<sup>a</sup> *Max-Planck-Institut für Extraterrestrische Physik, D-85740 Garching, Germany*  
e-mail: klumov@mpe.mpg.de

<sup>b</sup> *School of Physics, The University of Sydney, New South Wales 2006, Australia*

Received October 11, 2005

The features of the Earth's dusty ionosphere are considered using as an example the summer polar mesosphere. The effect of the optical properties of microparticles on their heating and photoelectron emission under the action of solar radiation is analyzed in detail. Certain photochemical consequences of the presence of dust in the upper atmosphere are studied. In particular, it is shown that microparticles can noticeably reduce the concentration of water vapor in the upper atmosphere and this decrease in turn limits the particle sizes. The influence of the effect under consideration on the behavior of the charged component of the upper atmosphere is discussed. © 2005 Pleiades Publishing, Inc.

PACS numbers: 52.27.Lw, 92.60.Mt, 94.20.–y

The processes in a multicomponent plasma containing dust particles are attracting considerable attention at present [1–4]. Interest in dusty plasma is stimulated both by its great abundance in nature and by the significant (determining in some cases) effect of dust particles on the state of the medium where they are present. Microparticles may play an important role in the Earth's ionosphere. Dust particles enter the upper atmosphere of the Earth due to the bombardment by micrometeorites (which then burn at altitudes of 80–100 km) and due to the convective transfer of particles of soot of volcanic origin and/or due to aerosol from the lower atmosphere. The concentration of particles with a characteristic size of about several nanometers is thought to vary in a range of  $10\text{--}10^3\text{ cm}^{-3}$  in dependence on the season and the micrometeorite activity [5]. Under ordinary conditions, such particles do not significantly affect the state of the ionospheric plasma and the photochemistry of the upper atmosphere. However, in the summer polar mesosphere at altitudes near 80–90 km, when the ambient air temperature is below 150 K and the water vapors present at these altitudes are supersaturated [6], the effect of the microparticles increases sharply (see, e.g., [7]). In this case, an important feature of the mesosphere is the presence of thin (compared to the atmosphere altitude scale) dust layers<sup>1</sup> at altitudes of 80–85 km that are known as noctilucent clouds or NLCs and at altitudes of 85–95 km that are known as polar mesosphere summer echoes or PMSEs. Noctilucent clouds consist of submicron-sized particles of water ice (with possible dust inclusions) [8] and are easily seen by optical methods. Polar mesosphere summer echoes consisting of charged nanoparti-

cles cannot be observed by optical methods and are manifested as strong radio reflections observed with radars at frequencies between 50 and 1000 MHz [9]. The strong correlation between the observations of NLCs and PMSEs implies that they have a common origin. For this reason, NLCs and PMSEs are frequently considered together under the common term *polar mesospheric clouds* (PMCs).

In this work, a model is presented for describing dusty structures in the summer polar mesosphere. This model takes into account the effect of solar radiation on the heating and charging of microparticles and the segmentation of particles in the gravitational field and the changes in the water vapor concentration in the mesosphere that are consistent with the growth of particles.

Figure 1 shows the parameters of the summer polar mesosphere that are important for the physics of polar mesospheric clouds. The conditions for the growth of particles are satisfied for altitudes near 80–90 km, where the local water vapors are supersaturated. Taking into account the presence of nanoparticles in the mesosphere, the most probable mechanism of the growth of particles is the heterogeneous nucleation on particles. The concentration of nanoparticles in the mesosphere is estimated as  $n_{\text{PMC}} \sim 10\text{--}10^3\text{ cm}^{-3}$  using data on the meteorite flux on the Earth that is  $\sim 100\text{ ton/day}$ .<sup>2</sup> One of the key parameters is the illumination intensity of the mesosphere by solar radiation. The inset in Fig. 1 shows the characteristic spectra of solar radiation as functions of the altitude for a zenith angle of  $85^\circ$  that is characteristic of the summer polar mesosphere. We note that short-wavelength radiation with wavelengths  $\lambda \leq 170\text{ nm}$  (i.e., with photon energies  $h\nu \geq 7.3\text{ eV}$ )

<sup>1</sup> The characteristic vertical scale of such layers is  $0.1\text{--}1\text{ km} \ll H_A \approx 7.5\text{ km}$ , where  $H_A$  is the height scale in the mesosphere.

<sup>2</sup> The distribution of meteorites of sizes  $a$  is close to the power law  $\propto a^{-n}$ ; centimeter-sized bodies primarily precipitate.

almost does not penetrate to the mesosphere, being strongly absorbed at altitudes  $H \approx 100$  km, except for the Ly $\alpha$  ( $\lambda \approx 121$  nm) atomic-hydrogen line, which is noticeably suppressed but is present at PMC altitudes.

Particles absorbing solar radiation can be heated. The heating value depends on the reflective index and shape of a microparticle, the altitude, the solar zenith angle, etc. When the temperature of ice particles<sup>3</sup> exceeds  $\approx 150$  K, they begin to be evaporated. This effect can be estimated from the balance equation for the temperature  $T_d$  of a dust particle (see, e.g., [10]). We write the balance equation in the form

$$P^{\text{sol}} + P^{\text{rad}} + P^{\text{col}} = 0, \quad (1)$$

where  $P^{\text{sol}}$  is the energy flux of solar radiation absorbed by the particle,  $P^{\text{rad}}$  describes the thermal radiation of the microparticle, and  $P^{\text{col}}$  describes the cooling of the dust particle due to collisions with neutrals. The expressions for  $P^{\text{sol}}$  and  $P^{\text{rad}}$  have the form

$$P^{\text{sol}} = \pi a^2 h c \int \sigma_{\text{abs}}(\lambda, a, m) (\Phi_{\lambda}^{\text{sol}}(H, \alpha_{za}) + \Phi_{\lambda}^{\text{sca}}(H, \alpha_{za})) d\lambda / \lambda,$$

$$P^{\text{rad}} = \pi a^2 h c \int \sigma_{\text{abs}}(\lambda, a, m) B_{\lambda}(T_d) d\lambda / \lambda,$$

where  $\sigma_{\text{abs}}$  is the absorption efficiency (the cross section for the absorption of radiation by the dust particle of the radius  $a$  normalized to  $\pi a^2$ ),  $m = n + ik$  is the complex refractive index of the microparticle material,  $\alpha_{za}$  is the solar zenith angle,  $B_{\lambda}$  is the spectral flux of the thermal radiation from the particle,  $\Phi_{\lambda}^{\text{sol/sca}}$  are the spectral fluxes of the direct (scattered by the atmosphere) solar radiation at the altitude  $H$ ,  $c$  is the speed of light, and  $h$  is Planck's constant. The rate of the cooling of dust particles by neutrals is estimated by the expression  $P^{\text{col}} \approx 4\pi a^2 \alpha_T n_n v_{\text{th}} k_B (T_d - T_n)$ , where  $\alpha_T$  is the coefficient (probability) of thermal accommodation (on the order of unity);  $n_n$  is the concentration of neutrals in the mesosphere ( $n_n \sim 3 \times 10^{14} \text{ cm}^{-3}$  at PMC altitudes);  $v_{\text{th}}$  and  $T_n$  are the thermal velocity and temperature of neutrals, respectively; and  $k_B$  is the Boltzmann constant. The numerical solution of the transport equation for solar radiation in the Earth's atmosphere shows that  $\Phi_{\lambda}^{\text{sol}}$  and  $\Phi_{\lambda}^{\text{sca}}$  may be of the same order of magnitude at the mesosphere altitudes under the PMC conditions. We note that the contribution of the thermal radiation of the Earth to the balance equation for  $T_d$  can be disregarded.

The dependence of the absorption efficiency on the refractive index, size of a dust particle, and the radiation wavelength is complex. Figure 2 shows the absorption (scattering) efficiencies  $\sigma_{\text{abs/sca}}$  calculated for 121-nm radiation according to the Mie theory as functions of  $a$

<sup>3</sup> Hereinafter, the term ice is used for water ice.

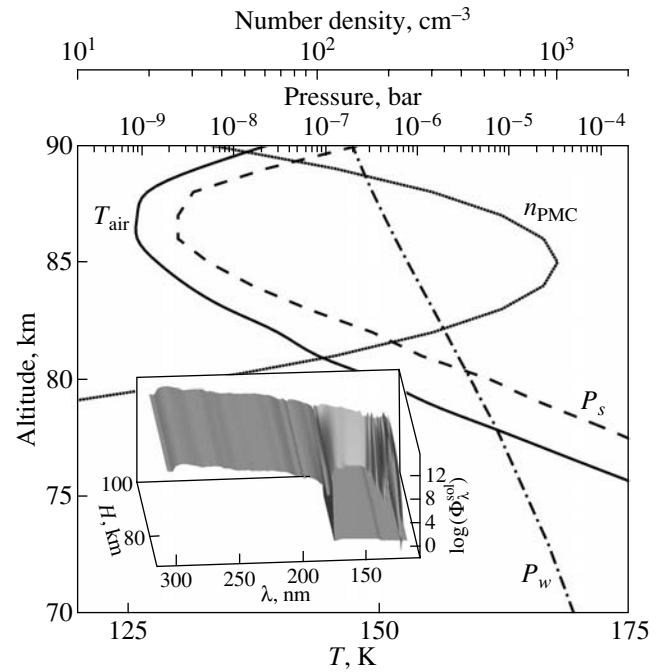


**Fig. 1.** Parameters of the summer polar mesosphere such as the vertical profiles of the temperature  $T_{\text{air}}$ , the pressure of saturated water vapor over the ice surface  $P_s$ , the partial pressure of water vapor  $P_w$ , and the nanoparticle concentration. Water vapor is supersaturated at altitudes of 80 to 90 km, and, owing to this fact, nanoparticles grow and polar mesospheric clouds are formed. The inset shows the spectral flux of solar radiation  $\Phi_{\lambda}^{\text{sol}}$  in the mesosphere vs. the altitude  $h$ . Radiation with  $\lambda < 170$  nm almost does not penetrate (except for the Ly $\alpha$  hydrogen line) at mesosphere altitudes, being absorbed at altitudes  $\approx 100$  km.

for spherical microparticles of various compositions. We note that  $\sigma_{\text{abs}}$  for an ice-coated silicon particle differs slightly from  $\sigma_{\text{abs}}$  for an ice particle. The inset shows the complex refractive index as a function of the photon energy for several compounds. We point to a very small imaginary part of the refractive index  $k$  (which determines the absorption of radiation by a particle) in the optical range for ice particles. The values of  $k$  for the other compounds under consideration are relatively large.

Figure 3 shows  $\sigma_{\text{abs}}$  for microparticles of various compositions as a function of the photon energy  $h\nu$  and particle size  $a$ . The noticeable absorption of solar radiation by submicron potassium is observed for photons with energies  $\sim 1\text{--}3$  eV, which easily penetrate to the mesosphere. At the same time, ice particles quite efficiently absorb short-wavelength ( $h\nu \geq 8$  eV) and IR ( $h\nu \leq 0.5$  eV) radiation. The results shown in the inset can be used to estimate the heating and charging mesospheric dust particles. It is convenient to introduce the dimensionless efficiency parameter  $\eta(a, m)$  of the absorption of solar radiation energy by a particle as

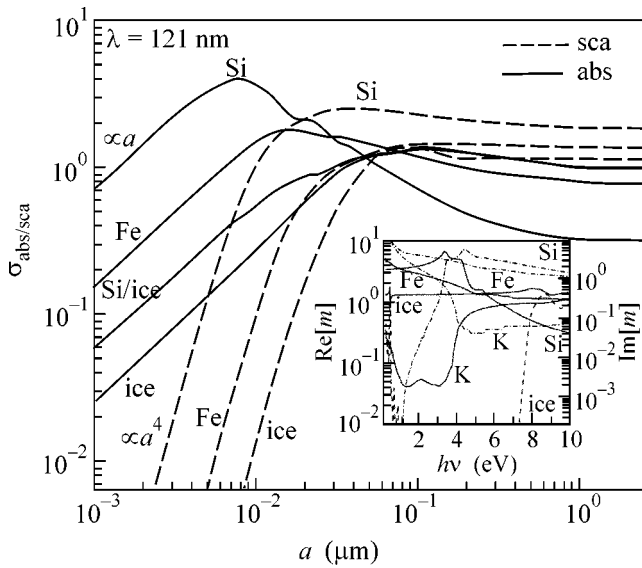


**Fig. 2.** Optical properties of microparticles various composition as calculated using the Mie theory. The efficiencies of scattering  $\sigma_{\text{sca}}$  and absorption  $\sigma_{\text{abs}}$  of 121-nm radiation versus the particle size  $a$  for various microparticle materials: ice, iron, silicon, and ice-coated silicon (at the corresponding radius ratio 1 : 2). The known scaling is shown for small  $a$  values ( $\sigma_{\text{sca}} \propto a^4$  and  $\sigma_{\text{abs}} \propto a$ ). The inset shows the (solid lines) real and (dash-dotted line and dashed line for ice) imaginary parts of the complex refractive index  $m$  vs. the photon energy for several compounds that can be present in a dust particle. The  $m$  values for ice were obtained at a temperature of 130 K, which is close to the temperature of the summer polar mesosphere [12].

$\eta(a, m) = S_0^{-1} \int \sigma_{\text{abs}} F_{\lambda}^0 d\lambda$ , where  $F_{\lambda}^0$  is the extra-atmospheric spectral energy flux<sup>4</sup> and  $S_0 \approx 1366 \text{ W m}^{-2}$  is the solar constant. For ice submicron-sized particles,  $\eta$  increases almost linearly with the particle radius:  $\eta(a = 0.025 \mu\text{m}) \approx 10^{-4}$ , whereas  $\eta(a = 0.8 \mu\text{m}) \approx 3 \times 10^{-3}$ . The estimate for the heating value  $\Delta T_d$  of such particles from the relation  $\eta_{\text{ice}} S_0 \approx P^{\text{col}}$  provides  $\Delta T_d \sim 3 \text{ K}$ ; i.e., the heating of ice submicron particles in the mesosphere is insufficient for their evaporation. For particles consisting of potassium, the situation changes radically: in this case,  $\eta_K \sim 0.1$ –1, the  $\eta_K$  value is maximal for particles with  $a \approx 30 \text{ nm}$  ( $\eta_{\text{Fe}}$  for iron microparticles has a maximum for  $a \approx 150 \text{ nm}$ ), and it is necessary to take into account the radiative cooling of such a particle. This circumstance determines the heating value  $T_d \approx 270 \text{ K}$ . Figure 4 shows the dependence of  $\Delta T_d = T_d - T_n$  on the parameter  $\eta$  for certain altitudes at which PMCs are located. This dependence summarizes the above estimates. The inset shows the dependence  $\eta(a)$  for certain compounds. These dependences make it possible to determine how microparticles of various

<sup>4</sup> The main contribution to the heating of microparticles comes from radiation of the optical and near IR ranges that is almost not absorbed in the mesosphere.

compositions are heated under the action of solar radiation in the mesosphere. The influence of the photoelectric effect on the charging of dust particles is discussed below.

The kinetic equation describing the evolution of the microparticle distribution function  $f_d(H, a, v, t)$  at the altitude  $H$  has the form

$$\frac{\partial f_d}{\partial t} + \frac{\alpha_w}{4} m_w v_w^T \rho_d (n_w - n_w^s) \frac{\partial f_d}{\partial a} + v \frac{\partial f_d}{\partial H} + \left[ g - \frac{\pi \rho c_s a^2 F_d (v + v_{\text{wind}})}{m_d} \right] \frac{\partial f_d}{\partial v} = 0. \quad (2)$$

Here,  $\rho$  and  $\rho_d$  are the densities of air and microparticle material, respectively;  $m_d$  is the microparticle mass;  $\alpha_w$  is the probability of the accommodation of water molecules colliding with a dust particle ( $\alpha_w \sim 1$  for supersaturated water vapors);  $v_w^T$  is the thermal velocity of water molecules;  $c_s$  is the local speed of sound;  $v_{\text{wind}}$  and  $v$  are the vertical velocities of the wind and particle, respectively;  $F_d$  is the factor (on the order of unity)

depending on the shape of a particle; and  $n_w$  and  $n_w^s$  are the concentrations of water vapor and saturated water vapors in the mesosphere, respectively. The second term in the equation describes the growth/evaporation of ice microparticles in dependence on the water vapor saturation, and the last term in Eq. (2) describes the sedimentation/rise of a dust particle interacting with neutrals (neutral drag). In the summer polar mesosphere, the average velocity component (directed against gravity) of neutral gas is  $\langle v_{\text{wind}} \rangle \approx 1$ –10 cm/s.

The solution of kinetic equation (2), together with the following equation describing the content of water vapors,

$$\frac{\partial n_w}{\partial t} + \frac{\partial \Gamma_w}{\partial h} = -P_w - n_w L_w - \pi \alpha_w v_w n_w \langle a^2 n_d \rangle, \quad (3)$$

where  $\Gamma_w$  is the vertical diffusion flow of water vapors (see, e.g., [11]) and  $P_w$  and  $L_w$  are photochemical sources and sinks of water vapors in the mesosphere (the last term on the right-hand side describes the loss of water molecules on growing dust particles), determines the characteristic size of particles in the summer polar mesosphere. Figure 5 shows the time dependence of the characteristic size of the particle and the concentration of water vapors for various particle concentrations  $n_d$  at  $v_{\text{wind}} \approx 5 \text{ cm/s}$ . It is clearly seen that the growth of particles leads to a decrease in the water concentration in the mesosphere, which in turn limits the further growth of microparticles. Thus, for typical PMC parameters, the effect of the mesosphere dehydration in the dust cloud limits the size of the particles in dependence on their concentration at a level of 0.05–0.1  $\mu\text{m}$ . We note that the effect of the mesosphere dehydration under the PMC conditions was revealed in [13], where

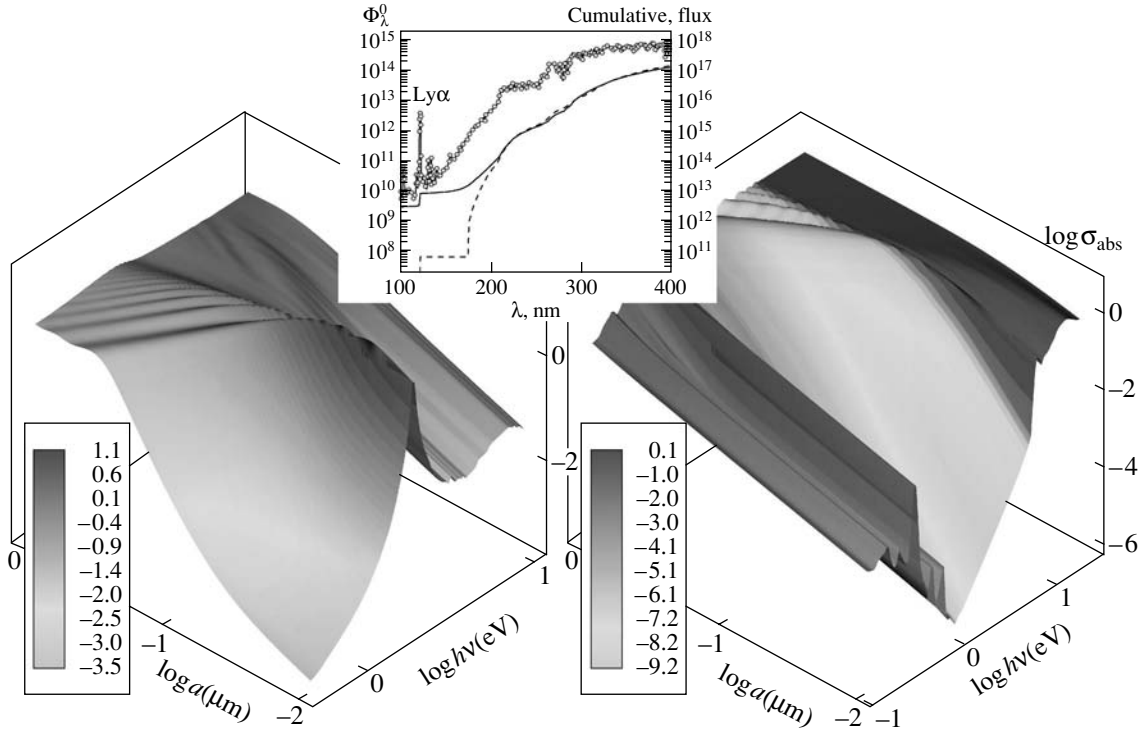


**Fig. 3.** Efficiency  $\sigma_{\text{abs}}$  of the absorption of radiation by a microparticle consisting of (left panel) potassium and (right panel) ice vs. the photon energy and particle size. The inset shows the spectral fluxes of solar radiation: (solid line) extra-atmospheric  $\Phi_{\lambda}^0$  and (dashed line) cumulative  $\Phi(H, \lambda) = \int_0^{\lambda} \Phi_{\lambda}^0 d\lambda$  at an altitude of 85 km.

the behavior of particles was simulated by molecular dynamics.

The recombination of the ionosphere plasma on the surface of microparticles can noticeably change the ionization properties of the summer polar mesosphere. Such an effect of dust particles on the ionization balance can be estimated from the system of the continuity equations for the electron concentration  $n_e$ , concentrations of simple  $n_i^s$  and cluster  $n_i^c$  positive ions, as well as for the charge  $Z_d^a$  of the microparticle with the radius  $a$ , which are written in the local approximation [14]:

$$\begin{aligned} \frac{\partial n_e}{\partial t} &= q_e - \alpha_s^{\text{rec}} n_e n_i^s - \alpha_c^{\text{rec}} n_e n_i^c \\ &+ \pi \langle v^{\text{photo}} a^2 n_d \rangle - \pi \langle v_e a^2 n_d \rangle, \\ \frac{\partial n_i^s}{\partial t} &= q_e - \alpha_s^{\text{rec}} n_e n_i^s - \beta_c n_i^s - \pi \langle v_s a^2 n_d \rangle, \\ \frac{\partial n_i^c}{\partial t} &= \beta_c n_i^s - \alpha_c^{\text{rec}} n_e n_i^c - \pi \langle v_c a^2 n_d \rangle, \\ \frac{\partial Z_d^a}{\partial t} &= v^{\text{photo}} + v_s + v_c - v_e. \end{aligned} \quad (4)$$

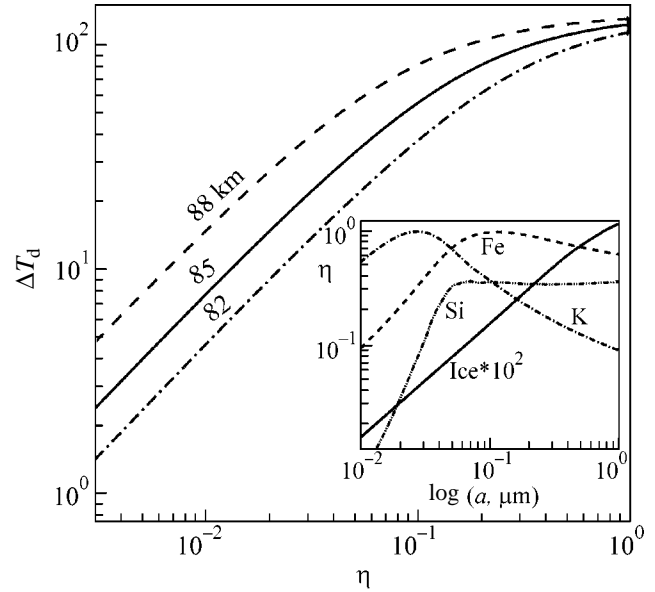


**Fig. 4.** Heating  $\Delta T_d$  of a dust microparticle in the mesosphere at the altitudes of polar mesospheric clouds vs. the parameter  $\eta(a, m) = S_0^{-1} \int \sigma_{\text{abs}}(a, m) F_{\lambda}^0 d\lambda$ , where  $S_0 = \int F_{\lambda}^0 d\lambda \approx 1366 \text{ W m}^{-2}$  is the solar constant. The inset shows the dependence  $\eta(a)$  for certain compounds.

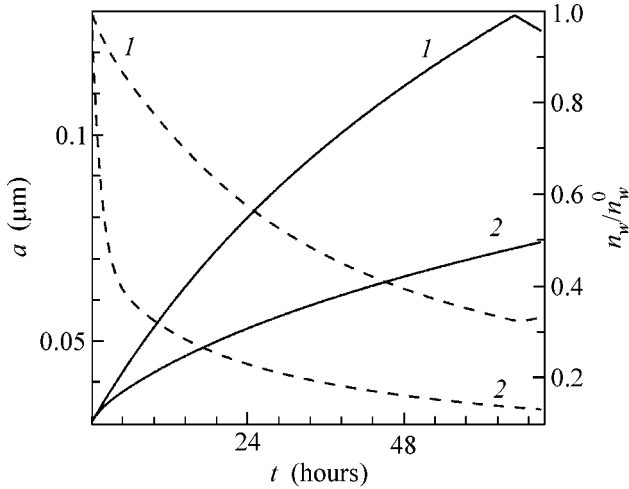


**Fig. 5.** Time dependences of (dashed lines) the relative concentration  $n_w(t)/n_w(0)$  of water vapors and (solid lines) the radius  $a$  of a microparticle in the dust cloud for the particle concentrations  $n_d = (1)$  10 and  $(2)$  100  $\text{cm}^{-3}$ .

Here,  $\alpha_{s/c}^{\text{rec}}$  are the recombination coefficients for simple (cluster) ions; the terms  $v_j$  ( $j = e, s, c$ ) describe the losses of electrons, as well as simple and cluster ions, respectively, on dust particles;  $\beta_c$  is the rate of the conversion of simple ions to cluster ions; and  $v_e^{\text{photo}}$  describes the creation of photoelectrons when solar radiation is absorbed by a single particle with the radius  $a$ . The expression determining  $v_e^{\text{photo}}$  has the form

$$v_e^{\text{photo}} = \pi a^2 \int_0^{\lambda_w} \sigma_{\text{abs}}(\lambda, a, m) \Phi_{\lambda}(H, \alpha_{za}) Y(\lambda, m, a) d\lambda, \quad (5)$$

where  $\lambda_w$  is the maximum (threshold) radiation wavelength for the photoelectric effect. For example,  $\lambda_w$  for ice, iron, sodium, potassium, aluminum, and silicon corresponds to a photon energy of 8.7, 4.7, 2.4, 2.3, 4.1, and 4.85 eV, respectively. The photoelectron production probability  $Y(\lambda, m, a)$  entering into Eq. (5) increases rapidly with the photon energy in the above-threshold region ( $|d\lambda/\lambda_w| \leq 1$ ) and is often estimated by the expression  $Y(\lambda) = Y_{\infty}(1 - \lambda/\lambda^*)$  (see, e.g., [15]), which interpolates the experimental data. The characteristic values are  $Y_{\infty} \sim 1$  and  $\lambda^* \approx \lambda_w$ . It is worth noting that  $Y$  increases when the size of a microparticle decreases. This dependence is explained by the fact that the photon mean free path  $l_v$  in the matter is usually much longer than the electron mean free path  $l_e$  and thereby experiments with bulky samples provide underestimated values  $Y_b$  for the photoelectron yield, because some photoelectrons do not leave a sample. For  $a \sim l_e$ , the yield of photoelectrons may be higher than  $Y_b$  by a factor of 2–3 [16]. We note that solar radiation with wavelengths  $\lambda \leq 170$  nm (i.e., with photon energies

$h\nu \geq 7.3$  eV) is almost completely absorbed at altitudes above the mesosphere except for the Ly $\alpha$  ( $\lambda \approx 121$  nm) atomic-hydrogen line. The damping of the Ly $\alpha$  line at PMC altitudes can be determined from Fig. 3. The ionization rate induced by the photoelectric effect on submicron ice particles can be estimated as  $v_{\text{ice}}^{\text{photo}} \approx \pi a^2 n_d \sigma_{\text{abs}} \Phi_{\text{Ly}\alpha} Y_{\text{ice}}$ . For  $n_d \sim 10^2 \text{ cm}^{-3}$  and  $a \approx 0.1 \text{ }\mu\text{m}$   $v_{\text{ice}}^{\text{photo}} \sim 10\text{--}100 \text{ cm}^{-3} \text{ s}^{-1}$ , which is much higher than the equilibrium ionization rate  $q_e = \alpha^{\text{rec}} n_e^2 \sim 0.1\text{--}10 \text{ cm}^{-3} \text{ s}^{-1}$ . We emphasize that even nanosized ice particles can make certain contribution to the ionization of the mesosphere, because  $\sigma_{\text{abs}} \sim a$  (see Fig. 2). If a dust particle consists of potassium, the role of photoelectrons becomes decisive beginning with moderate concentrations of submicron particles  $n_d \sim 1 \text{ cm}^{-3}$ . Indeed, the cumulative flux of photons is  $\Phi(\lambda_w^K) \sim 10^{17} \text{ cm}^{-2} \text{ s}^{-1}$ ; for such photons,  $\sigma_{\text{abs}} \sim 0.1\text{--}1$  over a wide  $a$  range and the photoemission rate induced by dust particles is very high,  $v_K^{\text{photo}} \approx \pi(a^2 n_d(a) \sigma_{\text{abs}}(a) \Phi(\lambda_w^K) Y_K) \sim 10^3 \text{ cm}^{-3} \text{ s}^{-1}$  even for small values  $Y_K \sim 10^{-4}$ . Such a high rate of the formation of electrons gives rise to a number of interesting photochemical effects. The electron concentration in the cloud of such dust particles increases, whereas the concentration of ions (primarily cluster ions) decreases due to the enhancement of electron–ion recombination. It is remarkable that such a behavior of the charged component under the PMC conditions is observed experimentally (see, e.g., [9]). Microparticles additionally acquire a considerable positive charge, which easily gives rise to polar mesosphere summer echoes—radio reflections from the dusty layer.

Thus, the effect of the composition and optical properties of microparticles on the formation of dust layers in the mesosphere has been analyzed in detail. The parameters of the heating of dust particles and photoemission of electrons under the action of solar radiation have been determined. Certain photochemical consequences of the presence of dust in the upper atmosphere have been analyzed. In particular, it has been shown that microparticles may significantly reduce the concentration of water vapors in the upper atmosphere, and this decrease, in turn, limits the size of particles. It has been shown that the composition of microparticles can determine the ionization features of the summer polar mesosphere.

This work was supported in part by der Max-Planck Gesellschaft (Max Planck Society, Germany) and by the Australian Research Council.

## REFERENCES

1. V. E. Fortov, A. G. Khrapak, S. A. Khrapak, *et al.*, *Usp. Fiz. Nauk* **174**, 495 (2004) [*Phys. Usp.* **47**, 447 (2004)].
2. S. V. Vladimirov and K. Ostrikov, *Phys. Rep.* **393**, 175 (2004).

3. V. E. Fortov, A. V. Ivlev, S. A. Khrapak, *et al.*, Phys. Rep. **421**, 1 (2005).
4. S. V. Vladimirov, K. Ostrikov, and A. A. Samarian, *Physics and Applications of Complex Plasmas* (Imperial College Press, London, 2005).
5. R. P. Turco, O. B. Toon, R. C. Whitten, *et al.*, Planet. Space Sci. **30**, 1147 (1982).
6. M. Gadsden and W. Schröder, *Noctilucent Clouds* (Springer, Berlin, 1989).
7. B. A. Klumov, S. I. Popel, and G. Morfill, Zh. Éksp. Teor. Fiz. **127**, 171 (2005) [JETP **100**, 152 (2005)].
8. U. von Zahn, G. Baumgarten, U. Berger, *et al.*, Atmos. Chem. Phys. **4**, 2449 (2004).
9. M. Rapp and F.-J. Lübken, Atmos. Chem. Phys. **4**, 2601 (2004).
10. G. Grams and G. Fiocco, J. Geophys. Res. **82**, 961 (1977).
11. B. J. Murray and J. M. C. Plane, Atmos. Chem. Phys. **5**, 1027 (2005).
12. M. L. Clapp, R. E. Miller, and D. R. Worsnop, J. Phys. Chem. **99**, 6317 (1995).
13. U. Berger and U. von Zahn, J. Geophys. Res. **107A**, 1366 (2002).
14. B. A. Klumov, S. I. Popel, and R. Bingham, Pis'ma Zh. Éksp. Teor. Fiz. **72**, 524 (2000) [JETP Lett. **72**, 364 (2000)].
15. B. T. Draine, Astron. J. Suppl. **36**, 595 (1978).
16. W. D. Watson, J. Opt. Soc. Am. **63**, 164 (1973).

*Translated by R. Tyapayev*

# Induced Soliton in a Fluid

N. K. Shelkownikov

Faculty of Physics, Moscow State University, Vorob'evy gory, Moscow, 119992 Russia

e-mail: shelkownikov@phys.msu.ru

Received March 29, 2005; in final form, October 11, 2005

The process of the generation and interaction of solitons in a circular wind–water tunnel is considered. It has been found that solitons with particle-like properties are formed in the channel under the action of a wind. In the presence of surfactants at the upper boundary or flotation, the phases of capillary and gravity–capillary waves are absent in the process of the soliton generation and the soliton formation time increases. © 2005 Pleiades Publishing, Inc.

PACS numbers: 91.10.Hm, 92.60.–e

Processes occurring in seas and oceans are caused to a great extent by the wave motion of water. Long waves such as tsunamis of seismic and meteorological origins (so-called meteotsunamis) provide a particularly strong effect on the dynamics. Meteotsunamis are tsunamis whose appearance nature is unclear [1]. In this work, we consider meteotsunamis caused by the action of a wind on the water surface, which can be described by the Korteweg–de Vries (KdV) equation with a right side, i.e., by the perturbed KdV equation. When investigating tsunami waves, the KdV equation  $u_t - \delta u u_x + u_{xxx} = 0$  is usually used. The solution of this equation is a solitary wave, the so-called KdV one-soliton solution:

$$u = -\frac{c}{2} \operatorname{sech}^2 \left[ \frac{\sqrt{c}}{2} (x - ct) \right] \quad (1)$$

where  $c$  and  $h$  are the velocity and height of the solitary wave.

The current revival of interest in the KdV equation and its solutions in the form of cnoidal and solitary waves discovered by Russell [2] was begun with the work by Fermi, Pasta, and Ulam, who studied the problem of the appearance of thermal chaos in a chain of nonlinearly coupled oscillators. The absence of the energy thermalization (energy distribution over all modes), as well as the recurrence of the system to the initial state with one excited basic mode, was revealed. Later, this recurrence was called the Fermi–Pasta–Ulam recurrence [3]. Those investigations were further continued in numerical experiments by Zabusky and Kruskal [4], who passed from the discrete problem in the form of a chain of pointlike oscillators to a continuous model. For convenience, they analyzed the evolution of waves on a closed circular trajectory for a plasma. The calculations showed that the initial sinusoidal profile of the wave is transformed in time to a chain of pulses propagating to the right. The largest pulse appeared to be on the extreme right, whereas the other

pulses retain their individuality and propagate with velocity proportional to their amplitudes. Each pulse can be approximately described by the solitary-wave solution of the KdV equation. Zabusky and Kruskal showed that the collision between pulses occurs such that the first pulse that has a large amplitude overtakes the other pulses and successively collides with each of them. In the process of these collisions, the pulses maintain their characteristics (height, width, and velocity). The only result of a collision is a phase shift: the larger pulse is shifted forward with respect to the situation before the interaction, whereas the lower pulse is shifted backward. Owing to such a particle-like behavior of the pulses, Zabusky and Kruskal called them “solitons” (from solitary waves).

More recently, solitons were studied by many researchers [5]. In particular, Berezin and Karpman [6] numerically showed that the initial perturbation decayed into four solitons and a low-amplitude short-wave packet. Gardner, Green, Kruskal, and Miura [7] obtained an analytical solution of the Cauchy problem for the KdV equation under an arbitrary initial condition. Hammack and Segur [8] conducted a series of experiments in a basin 31.6 m in length, 61 cm in depth, and 39.4 cm in width. A vertical plunger at one of the ends of the basin induced a rectangular-pulse perturbation of the water surface. As this pulse propagates, it decays into separate solitons.

Weidman and Maxworthy [9] experimentally studied the cases of strong and weak interactions between solitons. They applied the term weak interaction to a head-on collision between two counterpropagating solitons that occurs for a short time, whereas the term strong interaction was referred to a long-term collision between two pulses propagating in one direction. It was found that the phase shift of solitons due to interaction differs from the value calculated using the theory of solitary waves.

Renouard, Seabro-Santos, and Temperville [10] simulated the soliton solutions of the KdV equation in a  $36 \times 0.55 \times 1.3$ -m laboratory channel. They studied solutions of the problems of the reflection of a soliton from the channel wall, collision between two solitons, passage of a soliton over an obstacle in the form of an underwater mountain and vertical bank, and viscous damping of solitons.

The wind field effect on the development of meteotsunamis was analyzed by Pelinovskii [1]. In order to describe this mechanism, the Reynolds equation was used. In addition to the convenient boundary conditions, the following condition of tangential stress continuity was imposed on the bottom and free surface of a viscous fluid:

$$\rho v_t \frac{\partial u}{\partial z} = T_s \quad (z = h), \quad \rho v_t \frac{\partial u}{\partial z} = T_b \quad (z = -h). \quad (2)$$

Here,  $v_t = \nu + K_z$ , where  $\nu$  is the molecular viscosity coefficient and  $K_z$  is the turbulent viscosity coefficient. The surface stress  $T_s$  is induced by the wind field and the bottom stress  $T_b$  ensures the dissipation of the wave energy. The equation is closed by taking into account the continuity equation. The surface stress is usually parameterized as  $T_s/\rho = c^*W|W|$ , where  $W$  is the wind velocity,  $c^*$  is the constant factor, and the other symbols are commonly accepted. It is thought that tsunamis can be generated by inhomogeneities of the wind field, for example, in a typhoon.

Shuleikin [11] much contributed to the investigation of the wind effect on the wave generation. He created a circular tunnel with an outer diameter of 40 m and an inner diameter of 38 m. The height of the tunnel from the bottom to the roof was equal to 5.6 m. A wind was generated by fans placed on the roof at identical distances between them. Shuleikin found the equation of the family of curves to which the profiles of wind waves, including trochoidal waves, belong, but he did not study solitary waves as follows from [11].

According to the above brief review of experimental investigations of solitons in a fluid, solitons were usually induced by means of wavemakers. In such a situation, it is important to experimentally reveal the possibility of generating solitons by a wind. To this end, we carried out special investigations in a circular wind-water tunnel (Fig. 1) with an outer diameter of 2.4 m, a width of 0.2 m, and a height of 0.4 m. As a result, a soliton arising under the action of the wind was found. Figure 2a shows a photograph covering the entire period between two successive passages of the same soliton (the circular channel swept in time). The investigations were conducted using both video and a string wave recorder. Capillary, gravity-capillary, and surface gravity waves, which increase in time, are observed in the process of the development of the soliton under the action of the wing. Further, two solitons interacting with each other were formed from the entire variety of wind waves. When their amplitudes were comparable

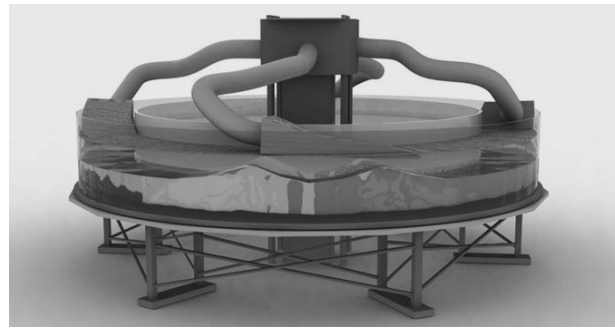


Fig. 1.

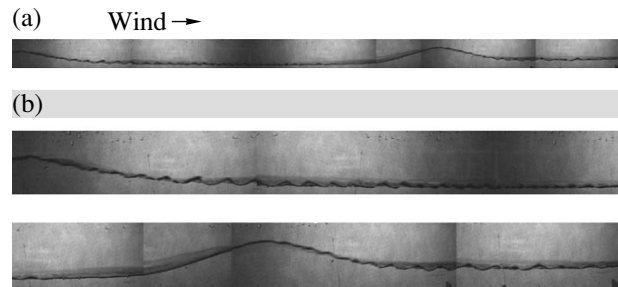


Fig. 2. Photographs covering the entire period between two successive passages of the same soliton (the circular channel swept in time) in the (a) ordinary and (b) increased form.

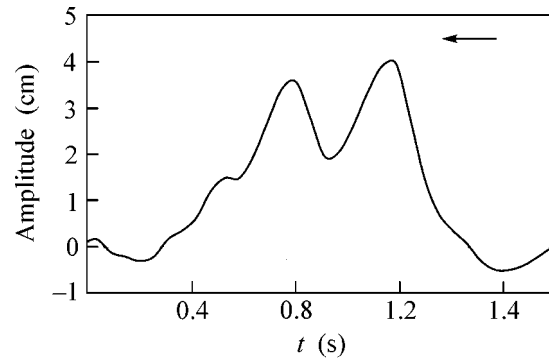


Fig. 3. Interaction between two wind solitons in the circular wind-water tunnel as detected by a wave recorder.

with each other, solitons do not pass through each other, they approach each other to a minimum distance of about 70 cm (Fig. 3), and the first soliton after the interaction is shifted forward and the second (back) soliton lags behind the first at a distance of about 1.5 m. This behavior is due to a complex nonlinear interaction between solitons, which are stable localized “pulses” covering the entire water height from the surface to the bottom. In this case, the vertical component of the velocities of particles on the leading front of soliton 2

and the back front of soliton 1 are directed up- and downward, respectively. Such a counterpropagating motion can destroy the leading front of soliton 2 and reduce its amplitude and velocity. After such an interaction, the trailing soliton with the minimum amplitude grows under the action of the wind, its velocity increases, and it begins to overtake the first soliton. The growth of the second soliton increases the screening of the first soliton from the wind effect. As a result, the velocity of the second soliton continues to increase, whereas the velocity of the first soliton decreases slightly. Correspondingly, their repeated interaction occurs after the second soliton, as well as its velocity, decreases again and lags behind the first soliton to the extreme left position (1.5 m). Then, the entire cycle is repeated. Such a periodic interaction between two solitons can be observed for several minutes (one interaction cycle lasted about 20 s) until the second soliton after a certain interaction lags so strongly (by more than half the tunnel length) that it appears to be ahead of the first soliton. (For convenience, we hold the enumeration of the solitons.) In this case, the first soliton moving behind the second soliton begins to screen the latter soliton whose velocity and amplitude appear to be lower than those of the first soliton. As a result, the first soliton with higher amplitude already passes through the second soliton rather than repulses from it. After double such interaction, only a small perturbation remains from the second soliton. This perturbation disappears after several interactions and one soliton remains. In the intervals of its motion, a weak wind excitement arises and is absorbed by the incident soliton. For illustration, Fig. 2b is drawn in an increased scale. As is seen, wind waves appear on the smooth fluid surface after the passage of the soliton. The amplitude of these waves increases until the passage of the second soliton that smoothes them. In this process, changes in the soliton parameters are not observed. A soliton arising at the fluid depth  $H = 11$  cm and wind velocity  $W_a = 12$  m/s moves with a velocity of 1 m/s. The length of this soliton at the zero level is equal to 90 cm and its height is equal to 8 cm. After the disappearance of the wind, the soliton profile is smoothed at the initial stage of damping, becomes more symmetric, and almost coincides with the soliton profile calculated using the KdV theory.

In the presence of surfactants at the upper boundary, the process of the soliton formation changes due to the absence of capillary and gravity–capillary waves. Moreover, long gravity waves are generated whose amplitude increases with time, and the soliton formation occurs according to the above scheme. The soliton formation in the presence of floatation (e.g., ice pieces) occurs similarly. In the both cases, the duration of the soliton formation process increases approximately by an order of magnitude and can reach 1.5 h. In the both cases of the presence of surfactants and floatation that exceed the respective critical values, no soliton is formed. This result is important for understanding the

possibility of forming solitons (meteotsunamis) in the presence of oil films and broken ice on the surface of the ocean.

In conclusion, it is worth noting that the formation of solitons in the case under consideration occurs under shallow water conditions under close values of nonlinearity and dispersion. For this reason, solitons are stable. In deep water, wind can induce groups of waves and envelope solitons, which are unstable due to high dispersion. Figuratively speaking, a soliton is induced in shallow water, whereas a group of waves is generated in deep water.

The above consideration leads to the following conclusions.

(i) The phenomenon of the transformation of various-scale wind waves into a determined pulse in the form of a soliton has been found under laboratory conditions. This pulse exists until wind exists in the tunnel. The recurrence phenomenon is not observed. The observed process of the formation of a wave–wind soliton is important for not only the theory of solitary waves but also for the determination of the nature of so-called killer waves [11].

(ii) It has been shown that multiple interaction occurs between two wind solitons close in amplitude, which exhibit particle-like properties. In the case of different amplitudes, the larger soliton passes through the smaller soliton many times and this process gives rise to the disappearance of the latter. This interaction variant is present when, after the sequential collision, the smaller (rear) soliton lags so strongly (by more than half the tunnel length) that it appears ahead of the larger soliton.

(iii) It has been found that the development of a wind soliton in the presence of floatation begins with the generation of long surface gravity waves passing over the phase of capillary and gravity–capillary waves. When these waves are developed, the above mechanism of the soliton formation starts. A similar process of the soliton formation is observed in the presence of surfactants. In both these cases, the time of the soliton formation increases by an order of magnitude and reaches 1.5 h on average. No soliton is formed at the critical level of floatation and concentration of surfactants. This result is important for understanding the possibility of forming solitons in the form of meteotsunamis in the presence of the pollution of the ocean surface, particularly in the shelf zone, as well as in seas covered by broken ice.

## REFERENCES

1. E. N. Pelinovskii, *Hydrodynamics of Seismic Sea Waves* (Inst. Prikl. Fiz. Ross. Akad. Nauk, Nizhni Novgorod, 1996), p. 276 [in Russian].
2. J. S. Russell, in *Reports of 14th Meeting of the British Association for the Advancement of Science* (John Murray, London, 1844), p. 311.

3. A. Fermi, J. Pasta, and S. Ulam, *Studies of Nonlinear Problems*, Los Alamos Report LA-1940 (Los Alamos Scientific Laboratory, Los Alamos, NM, 1955).
4. N. J. Zabusky and M. D. Kruskal, *Phys. Rev. Lett.* **15**, 240 (1965).
5. *Solitons*, Ed. by R. K. Bullough and P. J. Coudrey (Springer, New York, 1980; Mir, Moscow, 1983).
6. Yu. A. Berezin and V. I. Karpman, *Zh. Éksp. Teor. Fiz.* **51**, 1557 (1966) [*Sov. Phys. JETP* **24**, 1049 (1967)].
7. C. S. Gardner, J. M. Green, M. Kruskal, and R. M. Miura, *Phys. Rev. Lett.* **19**, 1095 (1967).
8. J. L. Hammack and H. Segur, *J. Fluid Mech.* **65**, 289 (1974).
9. P. D. Weidman and T. Maxworthy, *J. Fluid Mech.* **85**, 417 (1978).
10. D. P. Renouard, F. J. Seabro-Santos, and A. M. Temperville, *Dyn. Atmos. Oceans* **9**, 341 (1985).
11. V. V. Shuleïkin, *Physics of the Sea* (Nauka, Moscow, 1968) [in Russian].

*Translated by R. Tyapaev*

## CaCuMn<sub>6</sub>O<sub>12</sub> vs. CaCu<sub>2</sub>Mn<sub>5</sub>O<sub>12</sub>: A Comparative Study<sup>†</sup>

O. Volkova<sup>a</sup>, E. Goodilin<sup>a</sup>, A. Vasiliev<sup>a</sup>, D. Khomskii<sup>b</sup>, N. Tristan<sup>c</sup>, P. Kersch<sup>c</sup>,  
Yu. Skourski<sup>c</sup>, K.-H. Mueller<sup>c</sup>, and B. Buechner<sup>c</sup>

<sup>a</sup> Moscow State University, Moscow, 119992 Russia

<sup>b</sup> Koeln University, D-50937 Koeln, Germany

<sup>c</sup> Leibniz Institute for Solid State and Materials Research, D-01171 Dresden, Germany

Received October 4, 2005

The ferrimagnetic compounds Ca(Cu<sub>x</sub>Mn<sub>3-x</sub>)Mn<sub>4</sub>O<sub>12</sub> of the double distorted perovskites AC<sub>3</sub>B<sub>4</sub>O<sub>12</sub> family exhibit a rapid increase of the ferromagnetic component in magnetization at partial substitution of square coordinated (Mn<sup>3+</sup>)<sub>C</sub> for (Cu<sup>2+</sup>)<sub>C</sub>. In the transport properties, this is seen as a change of the semiconducting type of resistivity for the metallic one. The evolution of magnetic properties of Ca(Cu<sub>x</sub>Mn<sub>3-x</sub>)Mn<sub>4</sub>O<sub>12</sub> is driven by strong antiferromagnetic exchange interaction of (Cu<sup>2+</sup>)<sub>C</sub> with (Mn<sup>3+</sup>/Mn<sup>4+</sup>)<sub>B</sub> coordinated octahedra. The competing interactions of (Mn<sup>3+</sup>)<sub>C</sub> with (Mn<sup>3+</sup>/Mn<sup>4+</sup>)<sub>B</sub> lead to the formation of noncollinear magnetic structures that can be aligned by magnetic fields. © 2005 Pleiades Publishing, Inc.

PACS numbers: 72.80.Ga, 75.10.-b, 75.47.Gk

Nowadays, along with continuing studies of colossal negative magnetoresistance in traditional manganese-based perovskites, this effect is actively investigated in more exotic systems such as Cu-doped spinels FeCr<sub>2</sub>S<sub>4</sub> or pyrochlore Tl<sub>2</sub>Mn<sub>2</sub>O<sub>7</sub> [1, 2]. The final goal of these studies is a magnetoresistance of about a few percent at elevated temperatures. Among the most promising candidates for that are the double distorted perovskites of the general formula Ca(Cu<sub>x</sub>Mn<sub>3-x</sub>)Mn<sub>4</sub>O<sub>12</sub>. The rich physics of these compounds follows from multiple and competing interactions of different magnetoactive ions in different crystallographic positions.

These compounds belong to the structural type AC<sub>3</sub>B<sub>4</sub>O<sub>12</sub> of the cubic symmetry  $Im\bar{3}$  [3]. The A position is twelve-coordinated and can be occupied by any large size ion independent of its valence state (e.g., Na<sup>+</sup>, Ca<sup>2+</sup>, Y<sup>3+</sup>, or Th<sup>4+</sup>). The C position is square coordinated and is preferable for the Jahn-Teller ions (e.g., Cu<sup>2+</sup>, Mn<sup>3+</sup>). The B position is octahedrally coordinated and can be occupied by both Mn<sup>3+</sup> and Mn<sup>4+</sup> ions. The tilted corner sharing octahedra BO<sub>6</sub> form the rigid perovskite framework while the CO<sub>4</sub> squares are not connected to each other.

The magnetic and transport properties of the AC<sub>3</sub>B<sub>4</sub>O<sub>12</sub> compounds with various compositions were the subject of several experimental and theoretical studies [4–13]. At substitution of Cu<sup>2+</sup> for Mn<sup>3+</sup> in the C position, the Curie temperature within the Ca(Cu<sub>x</sub>Mn<sub>3-x</sub>)Mn<sub>4</sub>O<sub>12</sub> family rapidly increases reaching  $T_C = 355$  K in CaCu<sub>3</sub>Mn<sub>4</sub>O<sub>12</sub> [6]. This process is accompanied by a

change of the manganese valence state in the B position from Mn<sup>3+</sup> to Mn<sup>4+</sup>. In Ca(Cu<sub>2.5</sub>Mn<sub>0.5</sub>)Mn<sub>4</sub>O<sub>12</sub>, a noncollinear magnetic structure was established in neutron scattering measurements [11, 12]. It was found that the magnetic moments of Cu<sup>2+</sup> in the C position are oriented antiparallel to the magnetic moments of Mn<sup>3+/4+</sup> in the B position, while the magnetic moments of Mn<sup>3+</sup> in the C position are tilted from this alignment. The evolution of the physical properties within the Ca(Cu<sub>x</sub>Mn<sub>3-x</sub>)Mn<sub>4</sub>O<sub>12</sub> family with the increase of the copper content is not fully investigated. In particular, the mechanisms responsible for the formation of collinear or noncollinear magnetic structures are not clarified yet. In this work, we report on a comparative study of two isostructural compounds CaCuMn<sub>6</sub>O<sub>12</sub> and CaCu<sub>2</sub>Mn<sub>5</sub>O<sub>12</sub> whose properties, in a sense, differ qualitatively.

In this study, the magnetization, the specific heat, and the resistivity were investigated on ceramic samples of the title compounds. The samples were obtained by aerosol spray pyrolysis of nitrate solutions with subsequent annealing at 850°C for 48 hours. The magnetization up to 5 T in the temperature range 2–350 K was measured by an MPMS Quantum Design magnetometer. The magnetization in fields up to 50 T was measured in a pulsed field facility. The specific heat was measured in a quasi-diabatic relaxation type Termis calorimeter in the temperature range 5–273 K. The resistivity was measured using a standard four-probe method.

The temperature dependences of the magnetization  $M$  in CaCuMn<sub>6</sub>O<sub>12</sub> (1) and CaCu<sub>2</sub>Mn<sub>5</sub>O<sub>12</sub> (2) taken at  $H = 0.1$  T are shown in Fig. 1. Both curves present fer-

<sup>†</sup>The text was submitted by the authors in English.

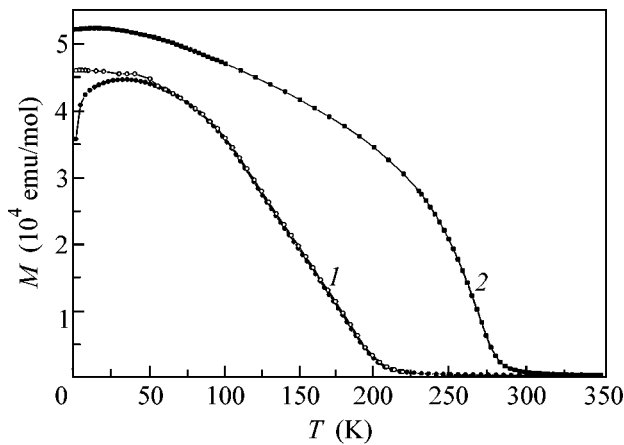


**Fig. 1.** Temperature dependence of magnetization of CaCuMn<sub>6</sub>O<sub>12</sub> (1) and CaCu<sub>2</sub>Mn<sub>5</sub>O<sub>12</sub> (2),  $H = 0.1$  T.

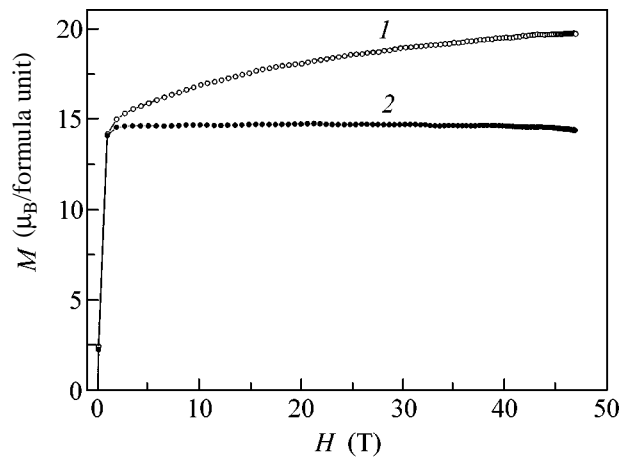


**Fig. 2.** Magnetization curves of CaCuMn<sub>6</sub>O<sub>12</sub> (1) and CaCu<sub>2</sub>Mn<sub>5</sub>O<sub>12</sub> (2) at  $T = 5$  K.

romagnetic-like upturns at  $T_{C1} = 190$  K and  $T_{C2} = 295$  K for the former and latter compounds, respectively. As is shown for CaCuMn<sub>6</sub>O<sub>12</sub>, a ZFC–FC hysteresis of magnetization is observed.

The field dependences of the magnetization in CaCuMn<sub>6</sub>O<sub>12</sub> (1) and CaCu<sub>2</sub>Mn<sub>5</sub>O<sub>12</sub> (2) measured at  $T = 5$  K in a pulsed magnetic field are shown in Fig. 2. These dependences differ qualitatively. In both compounds, the magnetization rapidly increases in a weak magnetic field reaching values of about  $15 \mu_B$  per formula unit. However, for a further increase of the magnetic field,  $M_1$  continually rises, while  $M_2$  saturates.  $M_1$  saturates at about 45 T reaching a value of about  $20 \mu_B$  per formula unit.

The temperature dependences of the specific heat  $C$  in CaCuMn<sub>6</sub>O<sub>12</sub> (1) and CaCu<sub>2</sub>Mn<sub>5</sub>O<sub>12</sub> (2) are shown in Fig. 3. The  $C$  vs.  $T$  dependences are in good correspondence with the  $M$  vs.  $T$  dependences. At  $T < T_{C1}$ ,  $C_1$  clearly exceeds  $C_2$ , which indicates the dominance of the magnetic specific heat contribution in CaCuMn<sub>6</sub>O<sub>12</sub>. At  $T > T_{C1}$ , the opposite situation is realized; i.e.,  $C_2$  exceeds  $C_1$ . In this temperature range, the magnetic specific heat contribution exists only in CaCu<sub>2</sub>Mn<sub>5</sub>O<sub>12</sub>. The  $C/T$  vs.  $T^2$  dependences shown in the inset to Fig. 3 indicate that the specific heat of CaCu<sub>2</sub>Mn<sub>5</sub>O<sub>12</sub> includes the electronic contribution  $C_{el} = \gamma T$  shown with a black line unlike that of CaCuMn<sub>6</sub>O<sub>12</sub>. The value of  $\gamma = 0.164$  J/mol K<sup>2</sup> was used to estimate the charge carriers concentration, which amounts at low temperatures to  $\sim 10^{19}$  cm<sup>-3</sup>.

Most clearly, the difference in the physical properties of CaCuMn<sub>6</sub>O<sub>12</sub> (1) and CaCu<sub>2</sub>Mn<sub>5</sub>O<sub>12</sub> (2) is seen in the temperature dependences of resistivity shown in Fig. 4. While the  $\rho_1$  vs.  $T$  dependence is of the semiconducting type, the  $\rho_2$  vs.  $T$  dependence is of the metallic type. The  $\log \rho_1$  vs.  $1/T$  dependence in CaCuMn<sub>6</sub>O<sub>12</sub>

shown in the inset to Fig. 4 indicates that the activation energy for current carriers changes from 60 meV at  $T > T_{C1}$  to 40 meV at  $T < T_{C1}$ . The magnetic phase transition at  $T_{C2}$  is well pronounced in the  $\rho_2$  vs.  $T$  dependence. Note that the absolute values of resistivity of these compounds differ by several orders of magnitude.

Thus, the comparison of CaCuMn<sub>6</sub>O<sub>12</sub> and CaCu<sub>2</sub>Mn<sub>5</sub>O<sub>12</sub> indicates that the compound with higher copper content possesses a higher Curie temperature and a lower saturation magnetization. Besides, these two compounds differ in the type of conductivity that is semiconducting in the former compound and metallic in the latter compound.

To treat these observations, one has to consider the exchange interactions between the various magnetic ions in the  $C$  and  $B$  positions and the magnetic interactions within the  $B$  position. The simplest situation is realized, evidently, in the parent compound of this family CaMn<sub>7</sub>O<sub>12</sub>, which orders predominantly antiferromagnetically at  $T_N = 49$  K [14]. Taking into account the rather low value of  $T_N$ , one can assume that the magnetism in this compound is suppressed by a weak overlap of the magnetoactive orbitals of  $(Mn^{3+})_C$  and  $(Mn^{3+}/Mn^{4+})_B$  and by the competition of the superexchange and double exchange interactions of  $(Mn^{3+}/Mn^{4+})_B$ .

The substitution of  $(Mn^{3+})_C$  for  $(Cu^{2+})_C$  leads to a rapid increase of a ferromagnetic component in magnetization. Apparently, the strongest exchange interaction in Ca(Cu <sub>$x$</sub> Mn <sub>$3-x$</sub> )Mn<sub>4</sub>O<sub>12</sub>, which dominates the magnetic behavior in these compounds, is an antiferromagnetic interaction between  $(Cu^{2+})_C$  and  $(Mn^{3+}/Mn^{4+})_B$  ions. This follows both from the existing experimental data [11, 12] and from the ab initio calculations [10]. The explanation of the strength of this interaction follows directly from the crystal and electronic structure in these systems. For the  $Cu^{2+}$  ions in square coordina-

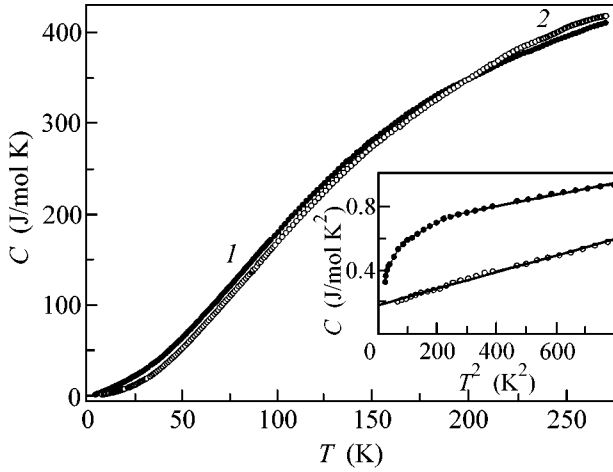


**Fig. 3.** Temperature dependence of specific heat in  $\text{CaCuMn}_6\text{O}_{12}$  (1) and  $\text{CaCu}_2\text{Mn}_5\text{O}_{12}$  (2).

tion, the active hole orbital is the  $d_{x^2-y^2}$ . This orbital has a rather strong overlap with the  $p_x, p_y$  orbitals of the  $\text{O}^{2-}$  ions, which in turn overlap with the  $d_{xz}, d_{yz}$  orbitals of  $t_{2g}$  manifold of  $(\text{Mn})_B$  with the hopping matrix element  $t_{pd\pi}$ . The angle  $(\text{Cu})_C\text{--O--}(\text{Mn})_B$  equal to the  $109^\circ$  bond in  $\text{CaCuMn}_6\text{O}_{12}$  and the  $110^\circ$  bond in  $\text{CaCu}_2\text{Mn}_5\text{O}_{12}$  is not far from a  $90^\circ$  one. Thus, the exchange path gives rather strong antiferromagnetic coupling according to the Goodenough-Kanamori-Anderson rules. It is very similar to  $90^\circ t_{2g}\text{--}e_g$  exchange.

One can estimate  $J \sim t_{pd\sigma}^2 t_{pd\sigma}^2 / \Delta^2 (\Delta + \Delta' + U_p)$ , where  $\Delta$  is the charge-transfer energy from oxygen to Mn or Cu (which is smaller), and  $\Delta'$  is the charge-transfer energy to another ion (if  $\Delta$  is O–Mn excitation, then  $\Delta'$  is that for O–Cu). All the other exchange processes between C and B sites are smaller. In the compounds studied, one should also discuss the  $e_g\text{--}e_g$  exchange  $(\text{Cu})_C\text{--}(\text{Mn}^{3+})_B$  as well as the different contributions due to the pairs  $(\text{Mn}^{3+})_C\text{--}(\text{Mn}^{3+}/\text{Mn}^{4+})_B$ . It is difficult to calculate quantitatively these processes, since they depend on the type of  $e_g$  occupation in  $(\text{Mn}^{3+})_B$ . Due to the almost square coordination of  $(\text{Mn}^{3+})_C$ , one can conclude that the electron at the  $e_g$ -levels of  $(\text{Mn}^{3+})_C$  would occupy the  $d_{z^2}$  orbital. In any case, such an analysis shows that there are different contributions to the exchange  $(\text{Mn}^{3+})_C\text{--}(\text{Mn}^{3+}/\text{Mn}^{4+})_B$ , which have a tendency to cancel one another, so that the resulting exchange is difficult to predict, and one can expect it to be relatively small.

There remains the exchange interactions between  $(\text{Mn}^{3+}/\text{Mn}^{4+})_B$ . Again, in a localized picture, one would have different contributions ( $t_{2g}\text{--}t_{2g}$ ,  $t_{2g}\text{--}e_g$ ,  $e_g\text{--}e_g$ ), which, for the  $\text{Mn}_B\text{--O--Mn}_B$  angle of about  $142^\circ$  (almost half-way between  $180^\circ$  and  $90^\circ$  exchange), are difficult to establish. The comparison with the situation

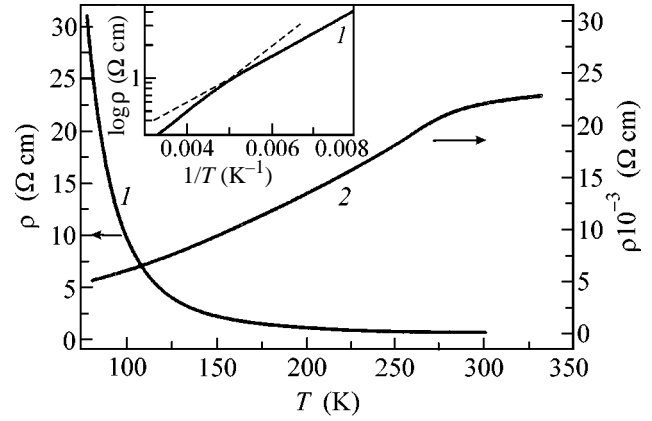


**Fig. 4.** Temperature dependence of resistivity of  $\text{CaCuMn}_6\text{O}_{12}$  (1) and  $\text{CaCu}_2\text{Mn}_5\text{O}_{12}$  (2). The inset: the resistivity of  $\text{CaCuMn}_6\text{O}_{12}$  in logarithmic scale versus inverse temperature.

in ferromagnetic pyrochlore manganite such as  $\text{Ti}_2\text{Mn}_2\text{O}_7$ , in which the Mn–O–Mn angle is comparable and all the Mn are  $\text{Mn}^{4+}$ , shows that even  $t_{2g}\text{--}t_{2g}$  exchange for this geometry may be ferromagnetic, all the more so for the  $e_g$  contribution that would exist for  $(\text{Mn}^{4+})_B\text{--}(\text{Mn}^{3+})_B$  pairs. Thus, in general, we should expect ferromagnetic interactions in the B sublattice, even in a picture of localized electrons. However, probably even more important is the ferromagnetic coupling within the B sublattice due to the double exchange mechanism. Apparently, the systems considered are either metallic or at least small gap semiconductors, and their conductivity is definitely due to  $e_g$ -electron hopping through the  $(\text{Mn})_B$  sublattice. It should be noted that the double exchange interaction may be not the main mechanism of the ferro-, or rather ferrimagnetic behavior of these systems as argued by Zeng [5], it may even be antiferromagnetic. It is mainly the  $(\text{Cu}^{2+})_C\text{--}(\text{Mn})_B$  antiferromagnetic super-exchange that forces the spins of the  $(\text{Mn})_B$  ions to be parallel.

Thus, the resulting picture is the following: in  $\text{Ca}(\text{Cu}_x\text{Mn}_{3-x})\text{Mn}_4\text{O}_{12}$ , there exist a rather strong  $(\text{Cu}^{2+})_C\text{--}(\text{Mn})_B$  antiferromagnetic exchange and substantial ferromagnetic  $(\text{Mn}^{3+}/\text{Mn}^{4+})_B$  coupling.  $(\text{Mn}^{3+})_C$  are coupled to  $(\text{Mn}^{3+}/\text{Mn}^{4+})_B$  by much weaker interaction, the sign of which is difficult to determine. This treatment seems to be consistent with the main experimental observations: the spins of the Cu sublattice are aligned antiparallel to those of  $(\text{Mn})_B$ , and  $(\text{Mn})_C$  may be canted with respect to the total magnetization in small fields [11, 12]. The latter can be easily rotated to the direction parallel to the field and to total magnetization (determined by the  $(\text{Mn})_B$  sublattice) in relatively weak fields.

Apparently, in  $\text{CaCu}_2\text{Mn}_5\text{O}_{12}$ , the saturation  $M_s = 15 \mu_B/\text{f.u.}$  is reached already at low fields  $\sim 1$  T, so that

in this system either the spins of (Mn<sup>3+</sup>)<sub>C</sub> are oriented parallel to the spins of (Mn)<sub>B</sub> from the very beginning or at least may have extremely weak coupling and be easy to rotate.

In CaCuMn<sub>6</sub>O<sub>12</sub>, the magnetization quickly reaches the same value at low fields ~ 1 T, after which it slowly approaches saturation of about 20 μ<sub>B</sub>/f.u. Therefore, one can expect the gradual rotation of (Mn<sup>3+</sup>)<sub>C</sub> spins in this system: there are more of them, and one can assume that their coupling to (Mn)<sub>B</sub> is somewhat stronger. In any case, the magnetic field of about 45 T seems to be sufficient to orient magnetic moments of both types of Mn ferromagnetically but definitely not enough to flip the Cu<sup>2+</sup> spin, which remains antiparallel to the net magnetization. These considerations are consistent with the results of the ab initio calculations, where the antiferromagnetic exchange (Cu<sup>2+</sup>)<sub>C</sub>–(Mn<sup>4+</sup>)<sub>B</sub> was estimated to be 300 K [10].

In conclusion, it is found that two isostructural compounds of the AC<sub>3</sub>B<sub>4</sub>O<sub>12</sub> family, namely, CaCuMn<sub>6</sub>O<sub>12</sub> and CaCu<sub>2</sub>Mn<sub>5</sub>O<sub>12</sub>, possess drastically different thermodynamic and kinetic properties. The former compound is a semiconductor with a basically noncollinear magnetic structure, while the latter compound is a metal with a presumably collinear magnetic structure. The main role in the magnetism of Cu-substituted double distorted manganites belongs to antiferromagnetic exchange interaction between (Cu<sup>2+</sup>)<sub>C</sub> and (Mn<sup>3+/Mn<sup>4+</sup></sup>)<sub>B</sub>. This is because the magnetoactive e<sub>g</sub> orbital of copper through oxygen p<sub>x</sub>, p<sub>y</sub> orbitals have the strongest overlap with the manifold of the t<sub>2g</sub> orbitals of manganese. The low values of the coercive force in these compounds provide rather high negative magne-

toresistance in sponge ceramics due to the intergranular tunneling in a wide temperature range.

This work was supported by the Russian Foundation for Basic Research (project nos. 03-02-16108 and 04-03-32183). The work of D. Khomskii was supported by SFB 608.

## REFERENCES

1. R. Fichtl, V. Tsurkan, P. Lunkenheimer, *et al.*, Phys. Rev. Lett. **94**, 027601 (2005).
2. M. Venkatesan, P. Velasco, J. A. Alonso, *et al.*, J. Phys.: Condens. Matter **16**, 3465 (2004).
3. B. Bochu, J. L. Buevoz, J. Chenavas, *et al.*, Solid State Commun. **36**, 133 (1980).
4. I. O. Troyanchuk, L. S. Lobanovsky, N. V. Kasper, *et al.*, Phys. Rev. B **58**, 14903 (1998).
5. Z. Zeng, M. Greenblatt, J. E. Sustrum IV, *et al.*, J. Solid State Chem. **147**, 185 (1999).
6. Z. Zeng, M. Greenblatt, M. A. Subramanian, and M. Croft, Phys. Rev. Lett. **82**, 3164 (1999).
7. R. Przenioslo, I. Sosnowska, E. Suard, *et al.*, J. Phys.: Condens. Matter **14**, 5747 (2002).
8. R. Przenioslo, I. Sosnowska, E. Suard, *et al.*, Physica B (Amsterdam) **344**, 358 (2004).
9. R. Przenioslo, M. Regulski, I. Sosnowska, and E. Schneider, J. Phys.: Condens. Matter **14**, 1061 (2002).
10. R. Weht and W. E. Pickett, Phys. Rev. B **65**, 014415 (2001).
11. J. Sanchez-Benitez, J. A. Alonso, M. J. Martinez-Lope, *et al.*, Chem. Mater. **15**, 2193 (2003).
12. J. Sanchez-Benitez, J. A. Alonso, A. de Anders, *et al.*, J. Magn. Magn. Mater. **272–276**, 1407 (2004).
13. A. N. Vasil'ev, O. S. Volkova, and E. A. Goodilin, JETP **101**, 367 (2005).
14. O. Volkova, Yu. Arango, N. Tristan, *et al.*, JETP Lett. **82**, 444 (2005).

# Qualitative Analysis of Spin-Dependent Tunneling in a Ferromagnetic Metal–Insulator–Ferromagnetic Metal Junction

A. I. Khachaturov

Donetsk Physicotechnical Institute, National Academy of Sciences of Ukraine, Donetsk, 83114 Ukraine  
e-mail: khach@hsts.fti.ac.donetsk.ua

Received July 5, 2005; in final form, October 5, 2005

A qualitative analysis of spin-dependent tunneling in ferromagnetic metal–insulator–ferromagnetic metal junctions is performed using the WKB approximation and a parabolic band model. It is shown that, as distinct from other tunneling characteristics, only electrons moving at large angles in the plane of the tunnel barrier contribute to the magnetoresistance. The cause of the rapid decrease in the junction magnetoresistance upon applying a bias voltage across the junction is ascertained. It is shown that this cause is attributed to the mirror character of tunneling and remains valid within the framework of more complicated models. © 2005 Pleiades Publishing, Inc.

PACS numbers: 73.40.–c, 75.70.–i

## 1. INTRODUCTION

Magnetoresistive properties in ferromagnetic metal–insulator–ferromagnetic metal (FM–I–FM) tunnel junctions were discovered as early as in 1975 [1]; however, intensive studies of them were initiated only twenty years later, after a technology was developed for manufacturing such junctions that retained these properties at room temperature [2]. During the subsequent decade, significant efforts were made to understand the main processes responsible for the occurrence of the junction magnetoresistance. The simple models [1, 3] were superseded by sophisticated theoretical constructions [4, 5]. However, in my opinion, in spite of the achieved agreement between the theoretical and experimental data, further advances in the area under study are restrained by the absence of a qualitative model in which the causes of the variation of the magnetoresistance upon varying the potential barrier parameters and the drop in the potential barrier upon applying a bias voltage across the tunnel junction are understood.

In this work, using the WKB approximation and a parabolic band model, I sought to obtain the simplest expression for the junction magnetoresistance based on which the main phenomena that occur upon tunneling between two ferromagnetic metals could be analyzed qualitatively.

The applicability of the approximations selected for studying spin-dependent tunneling was convincingly proved in [6, 7], where junction magnetoresistance values close to those observed experimentally were obtained at rather reasonable values of the barrier parameters. The band structure parameters used in this

case for ferromagnetic iron electrodes were  $E_{F_1} = 2.25$  eV and  $m_1 = 1.27m$  for the spin-up band (subscript 1) and  $E_{F_2} = 0.35$  eV and  $m_2 = 1.36m$  for the spin-down band (subscript 2) and were obtained from first-principles calculations. For the sake of simplicity, the effective electron mass in the insulating layer and in both of the electrode bands in my model was set equal to the free electron mass  $m$ .

## 2. JUNCTION MAGNETORESISTANCE AT ZERO BIAS VOLTAGE

Consider that tunneling is elastic and has a mirror character; that is, in the transition from the initial to final electrode, an electron conserves its total energy  $E$  and the transverse component of the quasi-momentum  $k_{\parallel}$ .

A remarkable feature of the model under consideration is that, as distinct from the Julliere model [1], a difference between the densities of states at the Fermi level for the spin-up bands  $N_1^{\uparrow}(E_F)$  and the spin-down bands  $N_2^{\downarrow}(E_F)$  cannot give rise to the occurrence of the tunnel magnetoresistance. Actually, according to Harrison [8], the current flowing through the potential barrier  $\phi(z)$  from a nondegenerate band can be represented as

$$J(V) = \frac{e}{4\pi^2 h} \int_{-\infty}^{\infty} dE (f_L - f_R) \int dSP(E, k_{\parallel}, V), \quad (1)$$

where  $S$  is the projection of the constant-energy surface

$E = \text{const}$  onto the plane of the barrier  $dS = d^2k_{\parallel}$ ;

$$P(E, k_{\parallel}, V) = \exp\left(-\frac{2}{\hbar} \int_{z_L}^{z_R} \sqrt{2m(\varphi(z, V) - E + E_{\parallel})} dz\right)$$

is the probability of electron tunneling through the barrier in the WKB approximation;  $f_L$  and  $f_R$  are the Fermi-Dirac distribution functions of the left-hand and right-hand electrodes, respectively; and  $z_R$  and  $z_L$  are the turning points on different sides of the barrier. The above equation contains no one-dimensional electron densities of states  $N_L(E_z) \propto (\partial E/\partial k_z)^{-1}$  and  $N_R(E_z) \propto (\partial E/\partial k_z)^{-1}$  associated with the motion along axis  $z$  perpendicular to the plane of the tunnel barrier. The two-dimensional densities of states  $N_L(E_{\parallel})$  and  $N_R(E_{\parallel})$ , which appear in Eq. (1) upon the change of variable from  $dS$  to  $dE_{\parallel}$ , also cannot be responsible for the occurrence of magnetoresistance if only because these values in our model are not only constant but also equal to each other. Actually,

$$N(E_{\parallel}) = \frac{1}{(2\pi)^2} \frac{\partial S}{\partial E_{\parallel}}, \quad (2)$$

where  $S$  is the area enclosed by the equipotential curve  $E_{\parallel} = \text{const}$ . With a quadratic law of dispersion,  $dS = 2\pi k_{\parallel} dk_{\parallel} = 2\pi m dE_{\parallel}/\hbar^2$  and  $N_1(E_{\parallel}) = N_2(E_{\parallel}) = m/2\pi\hbar^2$ .

It turns out that the occurrence of the junction magnetoresistance in the case under consideration is due to a difference between the Fermi radii  $k_{F_1}$  and  $k_{F_2}$ , as a result of which the areas of summation over  $S$  in Eq. (1) at different orientations of the magnetization can significantly differ. Assuming that the temperature  $T = 0$  in Eq. (1) and differentiating this equation with respect to the bias voltage  $V$ , it can be found that the differential conductance of the tunneling junction  $\sigma(V) = dI/dV$  at zero voltage takes the form

$$\sigma(0) = \frac{e^2}{4\pi^2\hbar} \int dSP(E_{F_L}, k_{\parallel}, 0). \quad (3)$$

In order to determine the area of integration in the presented equation, it is necessary to project the Fermi surfaces of the left-hand and right-hand electrodes onto the plane of the tunnel barrier and to find the overlap area of these projections.

In the case of elastic tunneling, an electron passing from the initial to final electrode retains the orientation of its spin. This fact leads to the existence of two independent parallel tunneling channels in tunnel junctions formed by two ferromagnetic metals. It will be considered that an antiparallel configuration is accomplished in the absence of a field in the junctions under study. In this configuration, the magnetization vectors of the ferromagnetic electrodes are oppositely directed. Then, when an electron that belongs to the spin-up band

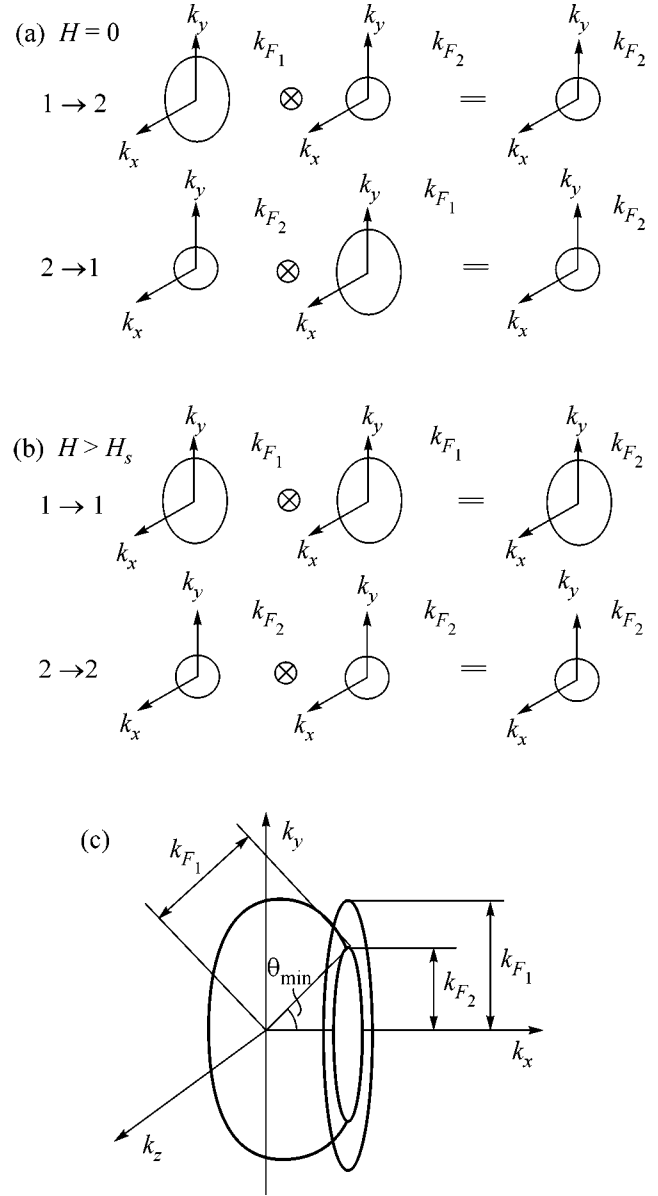


**Fig. 1.** (a) Overlap of the projections of Fermi surfaces onto the plane of the tunnel junction in  $1 \rightarrow 2$  and  $2 \rightarrow 1$  channels at the antiparallel configuration of the magnetizations of electrodes. (b) Overlap of projections of Fermi surfaces onto the plane of the tunnel junction in  $1 \rightarrow 1$  and  $2 \rightarrow 2$  channels at the parallel configuration. (c) Area of the Fermi surface on which electrons that contribute to the junction magnetoresistance JMR(0) at  $V(0)$  are located. The ring determined by the radii  $k_{F_1}$  and  $k_{F_2}$  is the projection of this area onto the plane of the tunnel junction.

passes to the opposite side of the junction, it will find itself in the spin-down band. This channel will be designated by indices  $1 \rightarrow 2$ , and its conductance will be denoted as  $\sigma_{12}(V)$ . Along with this channel, at the antiparallel configuration, there is a  $2 \rightarrow 1$  channel in which an electron initially belonging to the band with a

low Fermi energy  $E_{F_2}$  and a smaller radius  $k_{F_2}$  (spin-down band) finds itself in the band with a higher Fermi energy  $E_{F_1}$  and a larger radius  $k_{F_1}$  (spin-up band). It is seen in Fig. 1a that the overlap area of the constant-energy surfaces  $E = E_{F_1}$  and  $E = E_{F_2}$  is the same in both cases:  $S_{12} = S_{21} = \pi k_{F_2}^2$ . Therefore, in the calculation of the tunnel conductance  $\sigma^{\uparrow\downarrow} = \sigma_{12} + \sigma_{21}$ , summation is carried out over two circles of the small radius  $k_{F_2}$ .

At the parallel configuration of the magnetizations, which is accomplished in the magnetic field  $H > H_s$  ( $H_s$  is the saturation field), electrons from the spin-up band tunnel into the spin-up band ( $1 \rightarrow 1$  channel) and electrons from the spin-down band find themselves in the spin-down band ( $2 \rightarrow 2$  channel). The summation area in the calculation of the conductance  $\sigma^{\uparrow\uparrow} = \sigma_{11} + \sigma_{22}$  consists of the large ( $S_{11} = \pi k_{F_1}^2$ ) and small ( $S_{22} = \pi k_{F_2}^2$ ) circles (Fig. 1b). The difference between the tunnel conductivities in the field  $\sigma^{\uparrow\uparrow}$  and outside the field  $\sigma^{\uparrow\downarrow}$  appears because the total summation area in the former case is larger than in the latter by the ring area  $S_{\text{RING}} = S_{11} - S_{12} = \pi(k_{F_1}^2 - k_{F_2}^2) \propto E_{F_1} - E_{F_2}$ . In other words, the unbalance of electrons responsible for the occurrence of the junction magnetoresistance at zero voltage arises because of the particles whose transverse quasi-momentum components lie inside the ring  $k_{F_2} \leq k_{\parallel} \leq k_{F_1}$ . This ring and the region of the Fermi surface in which these electrons are located are shown in Fig. 1c. In this figure, it is seen that all these electrons move in the plane of the barrier at an angle  $\theta > \theta_{\min} = \arcsin(\sqrt{E_{F_1}/E_{F_2}})$ .

By definition, the junction magnetoresistance (JMR) equals

$$\text{JMR}(V) = \frac{\sigma^{\uparrow\uparrow}(V) - \sigma^{\uparrow\downarrow}(V)}{\sigma^{\uparrow\uparrow}(V)} = \frac{\sigma_{11}(V) - \sigma_{12}(V)}{\sigma_{11}(V) + \sigma_{22}(V)}. \quad (4)$$

With the assumption that  $V = 0$ , Eq. (3) leads to the following equation for the junction magnetoresistance at zero voltage:

$$\text{JMR}(0) = \frac{\int_{(s_1 - s_2)} P(E_{F_1}, k_{\parallel}, 0) dS}{\int_{(s_1)} P(E_{F_1}, k_{\parallel}, 0) dS + \int_{(s_2)} P(E_{F_2}, k_{\parallel}, 0) dS}. \quad (5)$$

After the change of variables from  $dS$  to  $dE_z$ , the equation for the junction magnetoresistance at zero voltage

containing only one-dimensional integrals is obtained

$$\text{JMR}(0) = \frac{\int_0^{E_{F_1} - E_{F_2}} P(E_z, 0) dE_z}{\int_0^{E_{F_1}} P(E_z, 0) dE_z + \int_0^{E_{F_2}} P(E_z, 0) dE_z}. \quad (6)$$

In this case, it was taken into account that  $dE = 0$  in the summation over the Fermi surface and, hence,  $dE_{\parallel} = dE_z$ , from which  $dS = dk_{\parallel}^2 \propto dE_{\parallel} = dE_z$ . If it is assumed that in Eq. (6)  $P(E_z, 0) = \text{const}$ , which is true for a  $\delta$ -shaped potential barrier, the highest possible value will be obtained  $\text{JMR}_{\delta\text{-barrier}}(0) = (E_{F_1} - E_{F_2}) / (E_{F_1} + E_{F_2})$ . For the band parameters used in this paper,  $\text{JMR}_{\delta\text{-barrier}}(0) = 76.5\%$ . For comparison, note that, for a barrier with a height of 3.5 eV and a thickness  $d = 10 \text{ \AA}$ , this value is almost three times lower and equals 25.6%.

The analysis carried out above leads to a nontrivial conclusion emphasizing the singularity of the characteristic under study. At zero voltage, the junction magnetoresistance differs from zero only because of the contribution of electrons whose angle of incidence  $\theta$  on the plane of the tunnel junction exceeds the minimum value  $\theta > \theta_{\min}$ . While the current-voltage characteristic  $I(V)$ , the differential tunnel conductance  $\sigma(V) = dI/dV$ , and the higher derivatives  $d^n I/dV^n - V$  are formed mainly because of electrons moving perpendicularly to the plane of the tunnel junction, the junction magnetoresistance is determined by electrons moving at large angles to the plane of the barrier. It is these electrons that are of main importance in studying JMR. The contribution from electrons normally incident on the plain of the barrier is present only in the denominator of Eq. (5); that is, such electrons can affect the value of the junction magnetoresistance but are not the cause of the appearance of JMR.

### 3. JUNCTION MAGNETORESISTANCE AT FINITE BIAS VOLTAGES

One of the characteristic features that distinguish tunneling into ferromagnetic metals from tunneling into common metals is that the Fermi energies of ferromagnetic electrodes are low and usually are significantly lower than the potential barrier height. The properties of tunnel junctions with low Fermi energies were studied in detail in [9], where it was shown that, in the case when the Fermi energy of the initial electrode exceeds the Fermi energy of the final electrode, the equation for the tunnel current somewhat differs from the standard one [10] in that the lower limit of integration over the energy  $E_z$  differs from zero. The point is that, in this case, part of electrons possessing a large

transverse component of the quasi-momentum  $k_z > k_{F_2}$  cannot satisfy the conditions of mirror tunneling. With regard to the results obtained in [9], contributions to the tunnel current from various channels of FM-I-FM junctions at zero temperature  $T = 0$  can be written in the form

$$I_{mn}(V) = K \left[ \int_{E_{F_m} - eV}^{E_{F_m}} (E_{F_m} - E_z) P(E_z, V) dE_z + eV \int_{L_{mn}(V)}^{E_{F_m} - eV} P(E_z, V) dE_z \right], \quad (7)$$

where  $K = 2\pi em/h^3$ , and  $P(E_z, V)$  is the tunnel barrier penetrability. The lower limit  $L_{mn}(V)$  differs from zero only for the  $1 \rightarrow 2$  channel

$$L_{mn}(V) = \begin{cases} 0, & m \geq n \\ (E_{F_1} - E_{F_2} - eV) \\ \times \Phi(E_{F_1} - E_{F_2} - eV), & m < n, \end{cases} \quad (8)$$

where  $\Phi(E_{F_1} - E_{F_2} - eV)$  is the step Heaviside function.

Differentiating Eq. (6) with respect to the voltage  $V$  gives equations for the differential conductivities of various channels

$$\sigma_{mn}(V) = K \left[ \int_{E_{F_m} - eV}^{E_{F_m}} (E_{F_m} - E_z) \frac{\partial P}{\partial V} dE_z + e \int_{L_{mn}(V)}^{E_{F_m} - eV} \left( P(V) + V \frac{\partial P}{\partial V} \right) dE_z + e^2 V P(E_{\min}, V) \Phi(E_{\min}) \delta_{m-1, n} \right], \quad (9)$$

where  $E_{\min} = E_{F_1} - E_{F_2} - eV$ , and  $\delta_{mn}$  is the Kronecker symbol. Substituting Eq. (9) into Eq. (4) gives

$$\text{JMR}(V) = \frac{\int_0^{E_{\min}} e \left( P(E_z, V) + V \frac{\partial P}{\partial V} \right) dE_z - e^2 V P(E_{\min}, V)}{\sigma_{11}(V) + \sigma_{22}(V)} \Phi(E_{\min}). \quad (10)$$

It is evident in Fig. 2 that the model under consideration correctly describes the drop in the magnetoresistance observed experimentally with increasing voltage

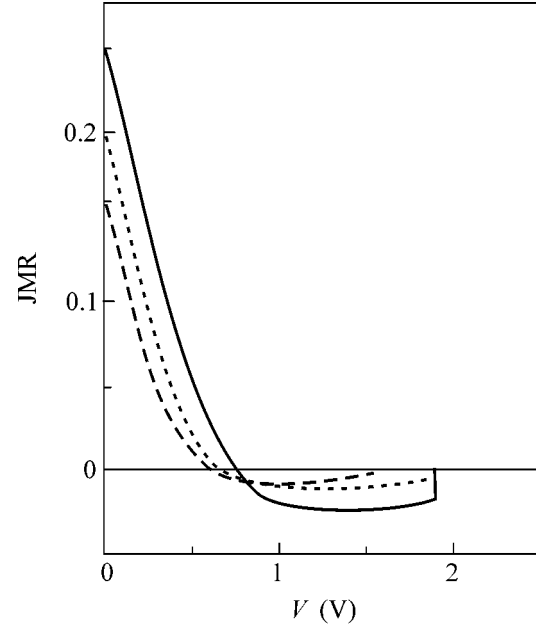


**Fig. 2.** Junction magnetoresistance vs. the bias voltage across the junction for the barrier parameters (solid line)  $\phi = 3.5$  eV,  $d = 10$  Å; (dotted line)  $\phi = 3.5$  eV,  $d = 12$  Å; and (dashed line)  $\phi = 2.5$  eV,  $d = 12$  Å.

across the junction. Moreover, the calculated curves exhibit a negative region in which, after attaining minimum values, these curves increase gradually, approaching zero, and reach zero stepwise at the bias voltage  $eV_0 = E_{F_1} - E_{F_2}$ . The presented curves demonstrate that increasing the height and decreasing the thickness of the barrier not only result in an increase in the absolute values of the magnetoresistance at points  $V = 0$  and  $V = V_0$  but also make its drop more flattened. In other words, with a  $\delta$ -shaped barrier, both the value and the behavior of the magnetoresistance are optimal. In this case, the probability of tunneling  $P(E_z, V)$  in Eq. (9) can be considered to be constant and the dependence of the magnetoresistance on the voltage is transformed into a straight line

$$\text{JMR}_{\delta\text{-barrier}}(V) = \frac{E_{F_1} - E_{F_2} - 2eV}{E_{F_1} + E_{F_2}} \Phi(E_{F_1} - E_{F_2} - eV), \quad (11)$$

which intersects the abscissa axis at the point  $V_0/2$  and attains the maximum absolute values  $|\text{JMR}|_{\max} = (E_{F_1} - E_{F_2}) / (E_{F_1} + E_{F_2})$  at the boundaries of the interval  $(0, V_0)$ .

While the electrons responsible for the appearance of  $\text{JMR}(0)$  at zero voltages lie on an area of the Fermi surface (Fig. 1c), such electrons at finite voltages are arranged inside the region formed by the constant-energy surfaces  $E = E_{F_1}$  and  $E = E_{F_1} - eV$  and two

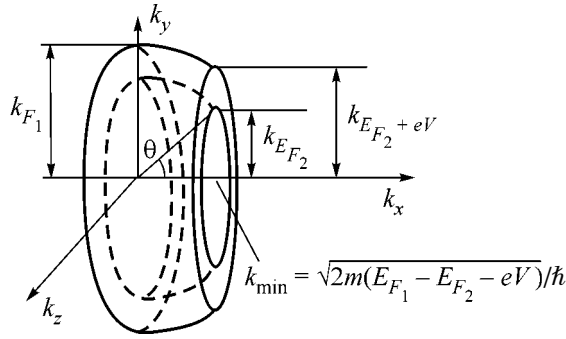


**Fig. 3.** Spherical layer in the reciprocal space of the spin-up band determined by the inequalities  $E_{F_1} - eV < E < E_{F_1}$  and  $0 < E_z < E_{F_1} - E_{F_2} - eV$  is the JMR( $V$ ) formation region. Only electrons whose states are located inside the presented region contribute to the junction tunnel resistance.

planes  $E_z = 0$  and  $E_z = E_{F_1} - E_{F_2} - eV$ . This region will be called the JMR( $V$ ) formation region (Fig. 3). It is because of the contribution  $\sigma_{\text{JMR}}(V)$  introduced by the electrons of this region to the conductance of the  $1 \rightarrow 1$  channel that the difference between  $\sigma_{11}(V)$  and  $\sigma_{12}(V)$  standing in the numerator of Eq. (4) differs from zero

$$\text{JMR}(V) = \frac{\sigma_{\text{JMR}}(V)}{\sigma_{11}(V) + \sigma_{22}(V)}. \quad (12)$$

The tunneling current created by electrons lying in a certain region of the reciprocal space can be represented as an integral over this space whose integrand is a product of the particle flux density from an infinitely small volume  $d^3k$  by the tunneling probability. Because the latter value is constant for a  $\delta$ -shaped barrier, the current in this case is simply proportional to the particle flux density  $W(V)$  and  $\sigma_{\text{JMR}}(V) \propto \partial W / \partial V$ . Therefore, the cause for the decrease in the junction magnetoresistance with increasing bias voltage across the junction is attributed to the topology of the JMR( $V$ ) formation region. Note that the volume of this region  $Q$  varies in a nonmonotonic way  $Q(V) = (\sqrt{2m})^3 eV \sqrt{E_{F_1} - E_{F_2} - eV} / \hbar^3$ , because there are two factors affecting  $Q$ : the first factor leading to an increase is associated with an increase in the cross section of the region under consideration with the plane  $k_z = 0$ , and the second one decreasing  $Q$  is due to a reduction of the distance between the planes  $k_z = 0$  and  $k_z = \sqrt{2m(E_{F_1} - E_{F_2} - eV)} / \hbar$ . The flux density  $W(V)$  of the electrons lying in the JMR( $V$ ) formation region also varies in a nonmonotonic way with increasing  $V$ . It can be easily found, because the section of the JMR region with the plane  $k_z = \text{const}$  is a ring whose area  $2\pi m e V / \hbar^2$  is independent of the place of the section. Taking into

account that the number of electron states on this ring is proportional to  $eV / (2\pi)^2$ , one finds that

$$W \propto \int_0^{E_{F_1} - E_{F_2} - eV} eV k_z dk_z \propto eV (E_{F_1} - E_{F_2} - eV).$$

The above analysis indicates that, in the case under study, the JMR region is organized in such a way that the flux created by the particles lying inside the region varies according to a quadratic law, increasing at  $eV < (E_{F_1} - E_{F_2})/2$  and decreasing at  $eV > (E_{F_1} - E_{F_2})/2$ . Because of this, the conductance  $\sigma_{\text{JMR}}(V)$  and, hence, the quantity under study  $\text{JMR}_{\delta\text{-barrier}}$  in the entire range of voltages  $[0, E_{F_1} - E_{F_2}]$  decreases by the linear law  $\text{JMR}_{\delta\text{-barrier}}(V) \propto \sigma_{\text{JMR}} \propto \partial W / \partial V \propto E_{F_1} - E_{F_2} - eV$ .

The cause by which the behavior of the curves in Fig. 2 differs from the linear law given by Eq. (11) is associated with the fact that the tunneling probability for potential barriers with finite parameters increases exponentially. At low bias voltages  $V$ , this growth is small; however, it starts to play a dominant role at large voltages: the conductance  $\sigma_{\text{JMR}}$  ends its decrease due to a decrease in the derivative of the flux density  $\partial W / \partial V$  and, along with the value under study, starts to grow.

## CONCLUSIONS AND SUMMARY

Up to the present day, the Julliere model [1] has been the only qualitative model of spin-dependent tunneling in FM-I-FM tunnel junctions. A difference between the electron densities of states at the level of Fermi bands with different orientations of spins serves as the cause for the appearance of the junction tunnel resistance in this model. The Julliere model gives the values of the junction magnetoresistance that agree by the order of magnitude with the values measured experimentally. However, this model cannot explain the drop observed experimentally in the JMR with increasing bias voltage across the junction. This drop was a subject of detailed investigations in many theoretical and experimental works [3]; however, in spite of considerable efforts spent in this direction, no common opinion on this issue has been elaborated so far.

The main advantage of the model considered in this work is that it is quasi-three-dimensional, while the Julliere model, as well as an overwhelming majority of the other works devoted to this issue, is essentially one-dimensional. Because of this, the proposed model contains an additional cause for the occurrence of the junction tunnel magnetoresistance that has not been considered previously. This cause is due to the mirror character of the tunneling and is an inherent property of the tunnel structures under study. It turns out that, because of features of the band structure of ferromagnetic metals, the number of electrons participating in tunneling in FM-I-FM junctions at the parallel polarization

always exceeds the corresponding number at the anti-parallel polarization. These electrons are located in a certain region of the reciprocal space that is organized in such a way that the derivative of their flux density  $\partial W/\partial V$  decreases linearly with increasing voltage  $V$ . It is this circumstance that is a qualitative cause for the drop of JMR at small bias voltages, where the change in the barrier penetrability is small and it may be considered that the quantity under study  $\text{JMR} \propto \partial W/\partial V$ . The subsequent growth of the junction magnetoresistance is related to the fact that the exponentially growing penetrability of the tunnel barrier starts to play a dominant role in its behavior as  $V$  increases.

In conclusion, the effect of the approximation used in this work on the obtained results will be discussed.

As was shown in many works, the use of more complicated models than WKB leads to a dispersion of the tunnel barrier penetrability  $P(E_z, E_{\parallel}, V)$  at which electrons with nonzero values of  $k_{\parallel}$  possess a larger probability than electrons with small transverse momenta (see, for example, [5, 11]). This fact can only improve the workability of the proposed approach. While the necessary twenty or thirty percent of the  $\text{JMR}(0)$  value is attained in the WKB approximation only at high and thin barriers and chiefly at a small value of  $E_{F_2}$ , these restrictions are removed at the dispersion indicated above.

The rejection of the parabolic band model will lead to the fact that the JMR formation region depicted in Fig. 3 will have a more complicated shape. However, the very fact of its existence is due to the mirror character of tunneling and is independent of the approxima-

tions used. Therefore, there is every reason to believe that the variation rate of its volume will also determine the form of the dependence of JMR on  $V$  in the cases when the dispersion law differs from a parabolic one.

I am grateful to M.A. Belogolovskii, Yu.V. Medvedev, and V.M. Svistunov for useful comments and discussion of the results of this work.

#### REFERENCES

1. M. Julliere, Phys. Lett. A **54**, 225 (1975).
2. J. S. Moodera, L. R. Kinder, T. M. Wong, and R. Meservey, Phys. Rev. Lett. **74**, 3273 (1995).
3. J. S. Moodera, J. Nassar, and G. Mathon, Annu. Rev. Mater. Sci. **29**, 381 (1999).
4. W. H. Butler, X.-G. Zhang, T. C. Schulthess, and J. M. MacLaren, Phys. Rev. B **63**, 054416 (2001).
5. C. Zhang, X.-G. Zhang, P. S. Krstić, *et al.*, Phys. Rev. B **69**, 134406 (2004).
6. F. Montaigne, M. Hehn, and A. Schuhl, Phys. Rev. B **64**, 14402 (2001).
7. A. H. Davies and J. M. MacLarren, J. Appl. Phys. **87**, 5224 (2000).
8. W. A. Harrison, Phys. Rev. **123**, 85 (1961).
9. A. I. Khachaturov, Fiz. Nizk. Temp. **31**, 109 (2005) [Low Temp. Phys. **31**, 85 (2005)].
10. R. B. Floyd and D. G. Walmsley, J. Phys. C **11**, 4601 (1978).
11. S. S. Liu and G. Y. Guo, J. Magn. Magn. Mater. **209**, 135 (2000).

*Translated by A. Bagatur'yants*

# Thermally Activated Negative Photoconductivity below 6 K in $p$ -GaAs/Al<sub>0.5</sub>Ga<sub>0.5</sub>As Heterostructures and the Effect of Uniaxial Compression

N. Ya. Minina<sup>a,\*</sup>, A. A. Il'evskii<sup>a</sup>, and W. Kraak<sup>b</sup>

<sup>a</sup> Faculty of Physics, Moscow State University, Vorob'evy gory, Moscow, 119992 Russia

\* e-mail: min@mig.phys.msu.ru

<sup>b</sup> Institute of Physics, Humboldt University, D-1055 Berlin, Germany

Received September 26, 2005; in final form, October 11, 2005

Thermally activated negative photoconductivity is observed in  $p$ -GaAs/Al<sub>0.5</sub>Ga<sub>0.5</sub>As:Be heterostructures under illumination with red light at temperatures below 6 K. As the temperature decreases, the concentration and mobility of 2D holes in the quantum well drop sharply, particularly under uniaxial compression. The phenomenon is quantitatively described under the assumption that a layer of deep donor-like traps with a low thermal activation barrier  $E_B = 3.0 \pm 0.5$  meV exists at a distance of about 7 nm from the heterojunction and that this barrier does not change with strain. Presumably, the traps may be the  $p$ -type dopant Be atoms diffusing from the active layer and occupying interstitial positions. © 2005 Pleiades Publishing, Inc.

PACS numbers: 73.40.Hb

Negative photoconductivity may occur in various heterostructures, including GaAs/Al<sub>x</sub>Ga<sub>1-x</sub>As with both  $p$ - [1, 2] and  $n$ -type [3] conductivities and different layer configurations, at various temperatures (from liquid helium to room temperature) under illumination with various wavelengths. Unlike the much-investigated positive delayed photoconductivity in  $n$ -GaAs/Al<sub>x</sub>Ga<sub>1-x</sub>As:Si with deep DX centers [4], the negative photoconductivity was given no unique interpretation: in some cases, it was attributed to the spatial separation of electron-hole pairs under illumination [5] while, in other cases, to the presence of deep donor centers [1]. Presumably, the nature of this phenomenon may be different depending on the specific situation.

This paper reports on the observation of a thermally activated negative photoconductivity (TANP) in  $p$ -GaAs/Al<sub>0.5</sub>Ga<sub>0.5</sub>As:Be heterostructures at temperatures below 6 K. The TANP dramatically increases under uniaxial compression: under a pressure of  $P = 4.4$  kbar, the resistivity of the samples becomes 200 times as great as the dark resistivity at  $P = 0$  at the same temperature of 1.5 K. The rather low temperature of the transition to the TANP state and the sharp increase in resistivity attract particular interest in studying the unusual behavior of the system.

We investigated the transport characteristics of 2D holes in the quantum well (QW) at the  $p$ -GaAs/Al<sub>0.5</sub>Ga<sub>0.5</sub>As:Be heterojunction, namely, their resistivity, concentration, and mobility, both in the dark and under illumination with a red light-emitting diode (LED), in the temperature range from 1.5 to 20 K. To

study the effect of an additional perturbation on the 2D holes in the QW, we applied uniaxial compression up to 4.4 kbar.

A single  $p$ -GaAs/Al<sub>0.5</sub>Ga<sub>0.5</sub>As:Be heterostructure was grown at the University of Copenhagen from molecular-beam epitaxy on a GaAs substrate in the [001] direction with the following layer sequence: a 0.7- $\mu$ m buffer layer, a 48-nm undoped Al<sub>0.5</sub>Ga<sub>0.5</sub>As spacer, a 40-nm active layer of Be-doped ( $1 \times 10^{24}$  m<sup>-3</sup>) Al<sub>0.5</sub>Ga<sub>0.5</sub>As, and a 10-nm capping layer of Be-doped ( $1 \times 10^{24}$  m<sup>-3</sup>) GaAs. Samples with the dimensions of  $0.5 \times 0.8 \times 3.0$  mm were split off from a disk along the [110] direction, and a mesa in the Hall configuration along the [1-10] direction was etched in the central part of every sample. At the temperature  $T = 1.5$  K, the 2D hole concentration in the dark was  $p = 3.1 \times 10^{15}$  m<sup>-2</sup>, and their mobility was  $\mu = 7.0$  m<sup>2</sup>/(V s). The uniaxial compression up to  $P = 4.4$  kbar was applied along the [110] direction by the method described in [6]. For illuminating the samples, we used a red LED with the characteristic photon energy  $h\nu = 1.96$  eV. Illumination with far-red ( $h\nu = 1.65$  eV) and infrared light ( $h\nu = 1.35$  eV) did not lead to the appearance of negative photoconductivity.

At a temperature of 1.5 K, when the sample is illuminated with the red LED, its conductivity  $\rho_{xx}$  increases several times and then remains constant. However, after the diode is turned off, the resistivity slowly relaxes to the dark resistivity value. The photoresistivity exhibits a thermal-activation behavior, which becomes much more pronounced under uniaxial deformation (Fig. 1). The temperature dependence of the dark resistivity

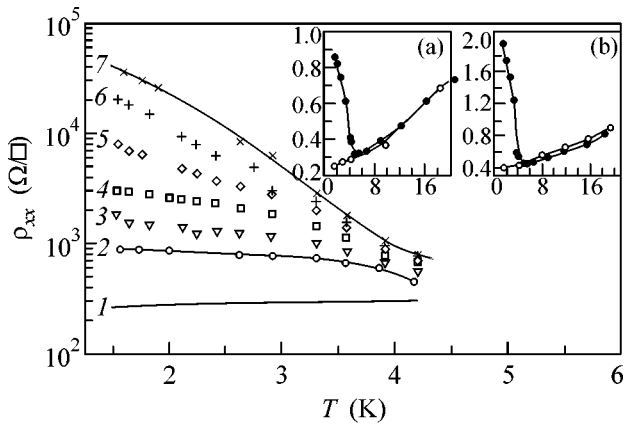


**Fig. 1.** Temperature dependences of (1) resistivity in the dark at  $P = 0$  and (2–7) under illumination at  $P = (2)$  0, (3) 1.7, (4) 2.9, (5) 3.8, (6) 4.2, and (7) 4.4 kbar. The insets show the dependences for  $P = (a)$  0 and (b) 2.1 kbar (open circles) in the dark and (closed circles) under illumination.

(curve 1 in Fig. 1, insets (a) and (b)) is of a metallic character. As one can see from Fig. 1 (insets (a) and (b)), the difference between the dark and illuminated states vanishes at  $T \geq 6$  K, and the  $\rho_{xx}(T)$  dependences

obtained for the illuminated and dark states coincide both under pressure and at  $P = 0$ .

The hole concentration  $p$  in the QW and its temperature dependence  $p(T)$  were measured by the Hall effect and verified by the Shubnikov–de Haas oscillations and the quantum Hall effect. The numerical values of concentration that were calculated for the dark and metastable TANP states from the Hall effect and the quantum effects coincide within the experimental error of 2–3%. This confirms that the measured Hall concentration  $p$  is only associated with 2D holes in the QW. Figure 2a shows the temperature dependences of concentration,  $p(T)$ , obtained in the illuminated state under different pressures. These dependences exhibit the following characteristic features: (i) the  $p(T)$  dependence is much weaker than the  $\rho_{xx}(T)$  dependence; (ii) as in the case of  $\rho_{xx}(T)$ , the difference between the concentrations in the dark and under illumination vanishes at  $T \geq 6$  K, except for the slight positive photoconductivity in the GaAs layer; (iii) the shape of the  $p(T)$  dependence is the same for different pressures; and (iv)  $p(T)$  evidently tends to saturation at the lowest temperatures, and the difference between the dark concentration and the saturation concentration is the same for different pressures. Under uniaxial compression, the concentra-

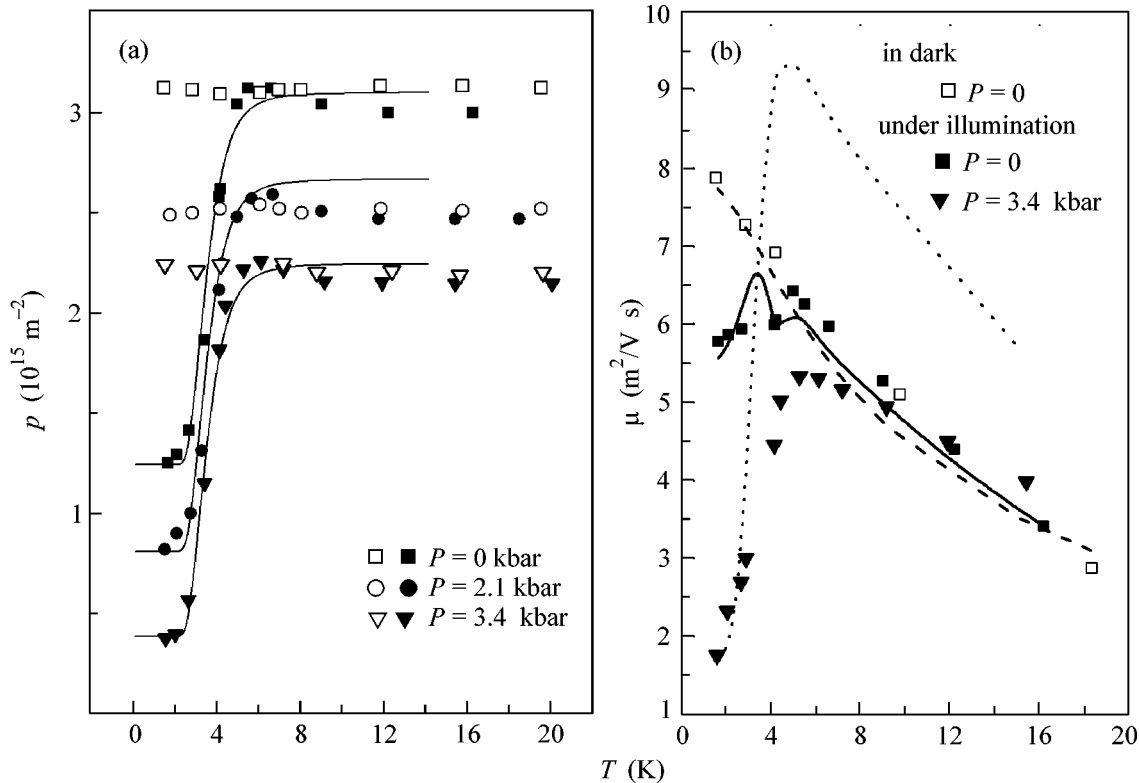


**Fig. 2.** Temperature dependences of the (a) concentration and (b) mobility of 2D holes as measured (open points) in the dark and (closed points) under illumination for various uniaxial compressions. The solid lines in panel (a) are numerical fits. In panel (b), the dashed line shows the calculation for the dark state at  $P = 0$ ; the solid and dotted lines refer to the calculations for  $P = 0$  and 3.4 kbar, respectively.

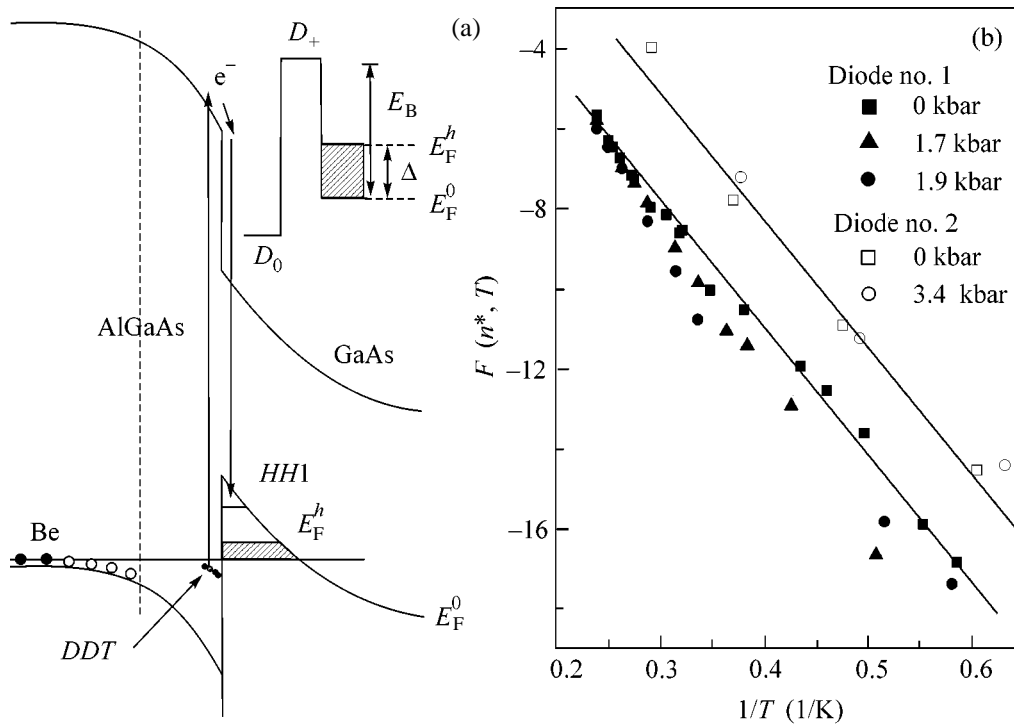


**Fig. 3.** (a) Band structure at the  $p$ -GaAs/Al<sub>0.5</sub>Ga<sub>0.5</sub>As:Be heterojunction and (inset) a schematic representation of the thermal activation barrier that illustrate the TANP effect: nonequilibrium electrons above the Fermi level are shown by hatching,  $HHI$  is the hole subband of the ground state, and  $DDT$  are deep donor-like traps. (b) Dependences  $F(1/T)$  for the determination of the thermal activation barrier  $E_B$ .

tion of 2D holes in the QW decreases approximately as  $dp/dP \approx -0.2 \times 10^{15} \text{ m}^{-2}/\text{kbar}$  for both illuminated and dark states. From Fig. 2a, one can see that the temperature dependence of 2D hole concentration in the dark is virtually absent, which is typical of GaAs/Al<sub>x</sub>Ga<sub>1-x</sub>As in this temperature region.

The resistivity  $\rho = 1/e\mu$  and the Hall coefficient  $R = 1/pe$  ( $\mu$  is the Hall mobility and  $e$  is the electron charge) were measured with the same temperature and pressure, which allowed us to calculate the mean Hall mobility  $\mu$ . Its temperature dependences for  $P = 0$  and for a uniaxial compression of 3.4 kbar are shown in Fig. 2b. Under illumination, the feature of the  $\mu(T)$  dependence is a maximum at  $T = 6$  K, which corresponds to the transition to the TANP state, and a sharp drop in mobility at  $T < 6$  K, whereas in the dark, the mobility of 2D holes monotonically increases.

As is seen in Fig. 2a, the combined effect of illumination and pressure leads to rather small hole concentrations ( $p = 4.0 \times 10^{14} \text{ m}^{-2}$ ). For such concentrations, in similar  $p$ -type GaAs/Al<sub>x</sub>Ga<sub>1-x</sub>As structures (although at temperatures below 1.5 K), a metal-insulator transition due to the appearance of a strong electron-electron interaction was observed (see, e.g., [7]). Therefore, despite the relatively high temperature  $T > 1.5$  K of our measurements, it is necessary to analyze the results in terms of the temperature dependence of

conductivity  $\sigma$  at a constant 2D carrier concentration  $p$  in the QW, as it was done in [7], where the transition to the dielectric state was revealed. The series of dependences  $\sigma(p)$  at  $T = \text{const}$ , which are easily obtained from the data of Figs. 1 and 2a, shows a metal-type growth of conductivity with decreasing temperature for a fixed 2D hole concentration in the QW for the whole range of measured concentrations  $p$  from  $3.2 \times 10^{15} \text{ m}^{-2}$  to  $4 \times 10^{14} \text{ m}^{-2}$ . In [7], where the measurements were performed in the temperature interval 1.6–0.26 K, a similar behavior was observed above the critical concentration of the metal-insulator transition  $p_K = 5 \times 10^{14} \text{ m}^{-2}$ . The fact that the temperature dependences of resistivity shown in Fig. 1 cannot be described by an exponential function also testifies against the presence of the metal-insulator transition.

Thermal activation regions in the dependences  $\rho(T)$  and  $n(T)$  were also observed earlier in studying the phenomenon of delayed photoconductivity of  $n$ -GaAs/AlGaAs:Si heterostructures with deep DX centers [9]: they occurred in the temperature region where  $kT$  was comparable to the energy barrier between the ground state and the excited state of a DX center. Therefore, in the subsequent analysis of our results, it is reasonable to use the assumption [1] that  $p$ -GaAs/Al<sub>0.5</sub>Ga<sub>0.5</sub>As:Be contains deep donor-like traps (Fig. 3a).

The red radiation with  $h\nu = 1.96$  eV, which was used in our experiments, cannot lead to direct electron transitions from the valence band to the conduction band in  $p$ -GaAs/Al<sub>0.5</sub>Ga<sub>0.5</sub>As with the band gap  $E_G = 2.1$  eV at liquid helium temperatures. However, because of the band discontinuity at the heterojunction, which may reach 0.25 eV at the valence band top, such transitions are possible from the aforementioned deep traps (Fig. 3a). Lying near the heterojunction slightly below the equilibrium Fermi level  $E_F^0$ , these traps are neutral before the illumination is turned on. Under the effect of light, electrons are excited to the conduction band and, under the effect of the electric field at the heterojunction, fall into the QW, where they recombine with 2D holes. This leads to a decrease in their concentration (which was observed in the experiment) and, hence, to a nonequilibrium Fermi energy  $E_F^h$  (Fig. 3a). The ionized states of deep donor-like traps in the spacer can be considered as holes that tunnel back into the QW when the light is turned off and, thus, take part in the relaxation process observed in the experiment.

To take into account the thermal activation effects, we follow the theory of deep donor centers and introduce a barrier between the ground state of a deep trap  $D_0$  and the excited state  $D_+$  due to the illumination (Fig. 3a). Only after a nonequilibrium electron existing to the right of the barrier (Fig. 3a) is trapped by the excited state  $D_+$  near the heterojunction will the initial state  $D_0$  be restored. For this purpose, the electron should overcome the effective barrier  $E_C = E_B - \Delta$ , whose value varies depending on the hole concentration in the QW (see Fig. 3a). For the metastable illuminated state, the detailed balance principle can be represented in the form

$$g(N_{D_0} - n^*) = n^*/\tau, \quad (1)$$

where  $g$  is the optical generation rate,  $N_{D_0}$  is the two-dimensional concentration of deep traps,  $\tau$  is the time of trapping of nonequilibrium electrons at the  $D_+$  level, and  $n^* = p_d - p$  determines the number of excited centers and is equal to the concentration of nonequilibrium electrons behind the barrier ( $p_d$  is the initial 2D hole concentration in the dark). The barrier  $E_B$  is measured with respect to the Fermi level  $E_F^0$ , and the Fermi energy  $E_F^h$  is calculated from the concentration of lighter 2D holes in the spin-split subband [9] in the parabolic approximation.

In the approach developed for analyzing the kinetic phenomena in materials with DX centers, the time constant characterizing the multiphoton capture of nonequilibrium electrons is expressed as [4]

$$\tau = \frac{1}{\sigma v_e n^*}, \quad (2)$$

where  $\sigma = \sigma_\infty \exp(-E_B/kT)$  describes the capture cross section at finite temperature and  $v_e$  is the velocity of nonequilibrium electrons. In our case,  $v_e = v_F^h = Ap^{1/2}$  ( $A = \text{const}$  and  $v_F^h$  is the Fermi velocity of holes in the QW). For our calculations, instead of  $E_B$ , we should use the effective barrier  $E_C = E_B - \Delta$ , where  $\Delta$  represents the variation of  $E_F^h$  from  $E_F^0$  (Fig. 3a); in the isotropic parabolic approximation,  $\Delta = Bn^*$  ( $B$  is a constant involving the effective hole masses from [9]). As a result, the dynamic equilibrium condition given by Eq. (1) can be reduced to the form

$$C(N_{D_0} - n^*) = n^{*2} p^{1/2} \exp\left(-\frac{E_B - \Delta}{kT}\right), \quad (3)$$

where  $C = g/\sigma_\infty A = \text{const}$ . The estimate  $N_{D_0} = 1.9 \times 10^{15} \text{ m}^{-2}$  is obtained from Fig. 2a: if the dependences  $p(T)$  exhibit saturation tending to  $p = p_{\text{sat}}$  at the lowest temperature, this means that all of the states  $N_{D_0}$  are excited and their number is equal to  $N_{D_0} = n^* = p_d - p_{\text{sat}}$ . It should be noted that this value is the same for all of the pressure values given in Fig. 2a. Taking the logarithm of Eq. (3), grouping the terms, and substituting  $\Delta = Bn^*$ , we obtain the expression

$$f(n^*, T) = \ln\left(\frac{(N_{D_0} - n^*)}{n^{*2} p^{1/2}}\right) - \frac{Bn^*}{kT} = -\ln C - \frac{E_B}{kT}, \quad (4)$$

where the function  $f(n^*, T)$  is calculated from experimental data. Plotting its dependence on  $1/T$  (Fig. 3b), we determine the barrier height from its slope:  $E_B = 3.0 \pm 0.5$  eV. Within the aforementioned error, this value is the same for all pressure values indicated in Fig. 2a.

A numerical fitting of Eq. (3) to the experimental dependence  $p(T)$  (the solid lines in Fig. 2a) with the use of two fitting parameters  $C$  and  $E_B$  shows that the best result is achieved for  $E_B = 6$  meV. This value also is the same for all of the pressure values indicated in Fig. 2a. The relatively low sensitivity of the fitting curves in Fig. 2a to the value of the parameter  $E_B$  testifies in favor of the first method of its determination, although the results obtained with the two methods are in satisfactory agreement. The small height of the thermal activation barrier accounts for the fact that the TANP is only observable at liquid helium temperatures.

Another transport characteristic that determines the TANP effect is the mobility (Fig. 2b), which strongly decreases at temperatures below 6 K, especially under uniaxial compression. If the concentration and the effective mass of 2D holes in the QW are known for all temperatures within the interval under study, we can numerically estimate the contribution of different scattering mechanisms to the mean mobility  $\mu$  that was

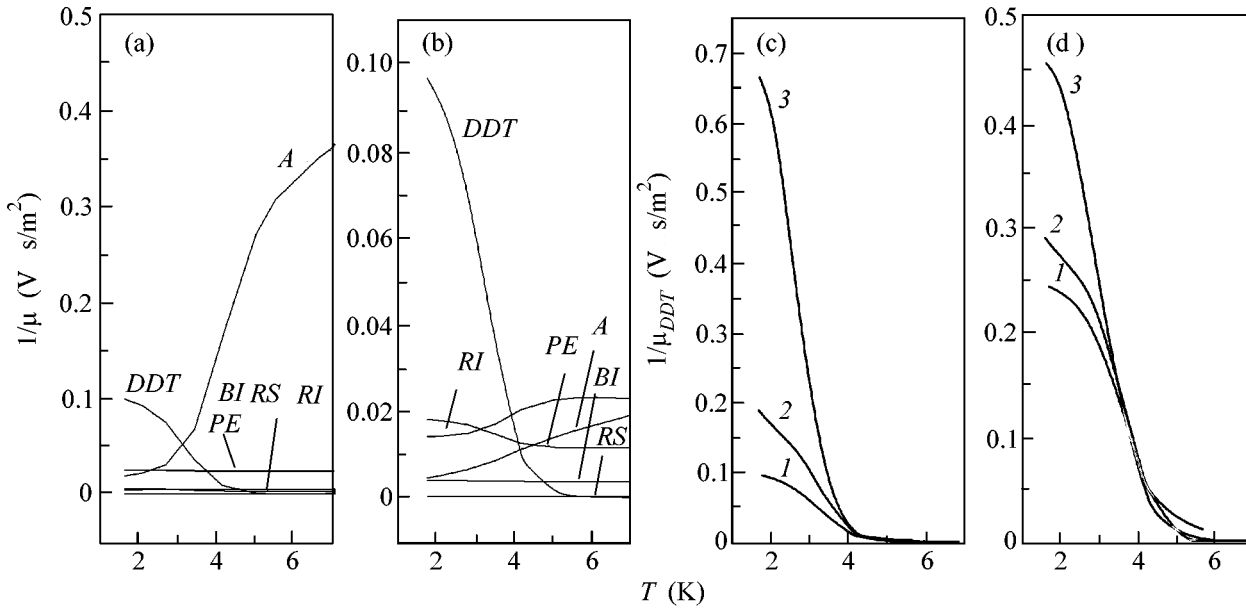


**Fig. 4.** Contributions of different scattering mechanisms to the inverse mobility in the TANP state for holes (a)  $m_0$  and (b)  $m_1$  at  $P = 0$  and the scattering efficiency  $1/\mu_{DDT}$  by ionized traps of holes with masses (c)  $m_0$  and (d)  $m_1$  under pressures  $P = (1) 0$ , (2) 2.1, and (3) 3.4 kbar.

determined experimentally. According to the Mattisen rule, we have

$$\frac{1}{\mu} = \frac{1}{\mu_{RI}} + \frac{1}{\mu_{BI}} + \frac{1}{\mu_A} + \frac{1}{\mu_{RS}} + \frac{1}{\mu_{PE}}, \quad (5)$$

where  $\mu_{RI}$ ,  $\mu_{BI}$ ,  $\mu_A$ ,  $\mu_{RS}$ , and  $\mu_{PE}$  are associated with the scattering by remote impurities (RI), background impurity (BI), acoustic phonons (A), and roughness of the heterojunction (RS), respectively, and with the piezoelectric scattering (PE). In our calculations, we used the approximations and formulas from [10], which were derived for a 2D electron gas at low temperatures; the value of  $\mu_{RS}$  was calculated according to [11]. It should be noted that, in the TANP state, an additional term appears on the right-hand side of Eq. (5):  $1/\mu_{DDT}$ . This term is associated with the scattering by positively charged deep ionized donor-like traps, which occur behind the barrier. Therefore, the value of  $1/\mu_{DDT}$  is calculated in the same way as the value of  $1/\mu_{RI}$ .

The energy spectrum of 2D holes in a triangular QW at the heterojunction in  $p$ -GaAs/AlGaAs is nonparabolic, and, in the samples under study with the total 2D hole concentration  $p = 3.1 \times 10^{15} \text{ m}^{-2}$ , is determined by two groups of carriers in the spin-split subbands  $S_0$  and  $S_1$  with effective masses  $m_0^*$  and  $m_1^*$ . The values of these masses and their dependence on the total 2D hole concentration in the QW were determined according to [9]. Hence, the Mattisen rule was applied to each of the groups of holes separately, and, in the mean mobility  $\mu$

determined experimentally, the hole mobilities in the two subbands were distinguished:

$$\mu = \frac{p_0\mu_0 + p_1\mu_1}{p_0 + p_1}, \quad (6)$$

where the total hole concentration in the two subbands is  $p = p_0 + p_1$ ,  $\mu_0 = \tau/m_0^*$ ,  $\mu_1 = \tau/m_1^*$ , and  $\tau$  is the relaxation time associated with the specific scattering mechanism in Eq. (5). In determining the individual concentrations  $p_0$  and  $p_1$  in the subbands, we had to use the parabolic approximation  $p_0/p_1 = m_0^*/m_1^*$  in spite of the nonparabolic dispersion law of the valence band.

The numerical calculation of the contributions of different scattering mechanisms to the inverse mobility was carried out for the dark and illuminated states at  $P = 0$  and under uniaxial compression in the whole temperature range under study. The calculations demonstrate the significance of the contributions from all of the scattering mechanisms to the mean mobility; they show a good agreement with experimental data (Fig. 2b) and suggest the following conclusions:

(i) In the dark, the monotone increase in the scattering by acoustic phonons with temperature at virtually invariable other mechanisms in the low-temperature region leads to a common monotone dependence  $\mu(T)$  in Fig. 2b (the dashed line).

(ii) Under illumination, the superposition of two main scattering mechanisms,  $1/\mu_A$  and  $1/\mu_{DDT}$ , with different temperature dependences (Figs. 4a and 4b) leads to the formation of a characteristic maximum in the dependence  $\mu(T)$  (Fig. 2b). The inflection with a small

additional minimum observed at 4 K in the dependence corresponding to  $P = 0$  under illumination is caused by the effect of other scattering mechanisms (Fig. 4c), which are characterized by finite values and different temperature dependences in this temperature region.

(iii) Under illumination, the scattering by deep ionized traps predominates below 6 K (Figs. 4a and 4b) and strongly increases under uniaxial compression (Figs. 4c and 4d). The physical reason for the growth of  $1/\mu$  with increasing pressure and decreasing temperature is directly related to the decrease in the 2D hole concentration in the QW and, hence, the screening of positively charged states. At temperatures  $T > 6$  K, in the absence of TANP, the mobility under uniaxial compression is determined by the considerable change in the anisotropy of the energy spectrum of  $p$ -GaAs/Al<sub>0.5</sub>Ga<sub>0.5</sub>As [12], which was ignored in the numerical calculations.

Evidently, the number of excited deep traps  $D^+ = p_d - p$ , as well as their positions and distribution in the spacer, determine the quantity  $1/\mu_{DDT}$ . We considered different types of the distribution of ionized traps from the active layer to the spacer, and the distance of the distribution front from the heterojunction served as the fitting parameter. All of the calculated dependences shown in Figs. 2b and 4 refer to a rectangular distribution of the ionized states of deep traps in the spacer with the edges of the distribution lying at a distance of 7–48 nm from the heterojunction. This distribution may only serve as an estimator.

Since, according to calculations, the distribution of the deep traps begins not from the heterojunction but from the active layer, we can expect that the traps arise as a result of the well-known diffusion of  $p$ -type dopant Be atoms from the active layer. This assumption is supported by [13], where, in Be-doped Al<sub>x</sub>Ga<sub>1-x</sub>As, the presence of deep levels associated with interstitial Be<sub>i</sub> was revealed. In addition, the spectroscopy of deep levels in  $p$ -Al<sub>0.5</sub>Ga<sub>0.5</sub>As with  $p$ -type Be impurity [14] indicated a series of deep traps with hole emission activation energies of 0.14, 0.4, and 0.46 eV. One of these values, namely, 0.14 eV, is suitable for describing the deep donor-like traps revealed in our experiments.

Summarizing the results, we formulate the following conclusions. In  $p$ -GaAs/Al<sub>0.5</sub>Ga<sub>0.5</sub>As with  $p$ -type Be impurity in the active layer, under illumination with a red LED, we observed a thermally activated negative photoconductivity. The effect appears at anomalously low temperatures  $T < 6$  K and is accompanied by a drastic decrease in both concentration and mobility of 2D

holes in the QW. The decrease in concentration can be quantitatively described by the model with deep donor-like traps lying near the heterojunction below the Fermi level if we introduce the barrier  $E_B = 3.0 \pm 0.5$  meV between the ground state of the traps and the state excited by the illumination. Numerical calculations show that the decrease in mobility at  $T < 6$  K is related to the scattering by positively charged excited deep states. The number of such states increases as the temperature decreases, and, to a first approximation, they occur in the spacer at a distance of 7–48 nm from the heterojunction. Presumably, these states may be represented by Be<sub>i</sub> interstitial atoms diffusing into the spacer from the active layer.

This work was supported by the Russian Foundation for Basic Research (project no. 04-02-16861) and by the Council of the President of the Russian Federation for Support of Young Scientists and Leading Scientific Schools (project no. NSh-1786.2003.2 for Brandt's scientific school).

## REFERENCES

1. M. J. Chou, D. C. Tsui, and G. Weinmann, *Appl. Phys. Lett.* **47**, 609 (1985).
2. R. A. Hopfel, *Appl. Phys. Lett.* **52**, 801 (1988).
3. C. S. Chang, H. P. Fetterman, D. Ni, *et al.*, *Appl. Phys. Lett.* **51**, 2233 (1987).
4. P. M. Mooney, *J. Appl. Phys.* **67**, R1 (1990).
5. A. S. Chaves and H. Chacham, *Appl. Phys. Lett.* **66**, 727 (1995).
6. W. Kraak, A. M. Savin, N. Ya. Minina, *et al.*, *JETP Lett.* **80**, 351 (2004).
7. M. Y. Symmons and M. Pepper, *Phys. Rev. B* **80**, 1292 (1998).
8. E. F. Schuber, J. Knecht, and K. Ploog, *Solid State Phys.* **18**, 1215 (1985).
9. T. Ando, *J. Phys. Soc. Jpn.* **54**, 1528 (1985).
10. K. Lee, M. S. Shur, T. J. Drummond, and H. Morkoc, *J. Appl. Phys.* **54**, 6432 (1983).
11. Y. Markus and U. Mierav, *Semicond. Sci. Technol.* **9**, 1297 (1994).
12. K. I. Kolokolov, A. M. Savin, S. D. Beneslavski, *et al.*, *Phys. Rev. B* **59**, 7537 (1999).
13. M. Morita, K. Kobayashi, T. Suzuki, and Y. Okano, *Jpn. J. Appl. Phys.* **28**, 553 (1989).
14. J. Szatkowski, E. Placzek-Popko, K. Sieranski, and O. P. Hansen, *Cryst. Res. Technol.* **31**, 313 (1996).

*Translated by E. Golyamina*

# Nuclear Quadrupole Resonance in the Gamma-Resonance Spectra of Soft Matter

M. A. Chuev

*Institute of Physics and Technology, Russian Academy of Sciences, Moscow, 117218 Russia*

*e-mail: chuev@ftian.oivta.ru*

Received September 30, 2005

It is shown that the harmonic librations (oscillations) of the principal axis of the electric field gradient tensor in “cages” of liquids, glasses, ferroliquids, and other “soft” systems qualitatively change the shape of the Mössbauer spectra of the quadrupole hyperfine structure. In addition to an effective decrease in the quadrupole coupling constant in the fast-libration limit, nuclear quadrupole resonance is predicted, which must be manifested in the Mössbauer spectra at the libration frequency that is approximately equal to the quadrupole splitting of spectral lines. By analogy with nuclear magnetic resonance, simple analytical expressions are derived, which describe resonance Mössbauer spectra in terms of the effective quadrupole coupling constant and the resonance splitting constant for the main lines. The observed features of the formation of quadrupole hyperfine structure spectra can be manifested in the Mössbauer spectra of soft matter and must be taken into account in analysis of experimental data. © 2005 Pleiades Publishing, Inc.

PACS numbers: 33.45.+x, 61.43.-j, 76.80.+y, 78.30.Cp

Normal liquids or glasses can be treated as ensembles of small particles (molecules) that are in constant intense motion due to which they collide with neighboring particles. On average, collisions lead to the reversal of the trajectories of particles so that they effectively move in a “cage” formed by the neighboring particles with a certain characteristic time  $\tau_l$ . Such a process is called librations. Particles can sometimes change positions and begin to oscillate in new cages. Such a structural relaxation or diffusive motion is characterized by its mean time  $\tau_r$ . It is usually supposed that these two types of motions have comparable characteristic times and the particles undergo continuous diffusion.

However, for low temperatures, it is expected that  $\tau_r \gg \tau_l$  and, at least in a short time, each particle undergoes almost harmonic oscillations around the principal axis of the anisotropic tensor of inertia of a molecule. Such a model of harmonic librations is widely used when analyzing the spectra of nuclear quadrupole resonance (NQR), and it has long been known that librations mainly determine the temperature dependence of the frequency of NQR [1]. Recently, such a model was successfully applied to describe inelastic neutron scattering in supercooled water [2]. We note that the time scale of harmonic librations is specified by the angular frequency of the free rotation of molecules, which is determined by the principal values of the tensor of inertia and characteristic collision time, so that the amplitude of harmonic librations can generally be arbitrary.

On the basis of the above grounds, we are going to consider a model of librations in soft matter in the form

of harmonic oscillations around one of the principal axes of the anisotropic tensor of inertia and to derive equations for describing Mössbauer spectra in the presence of quadrupole hyperfine interaction characteristic of liquids [3]. We will consider only axisymmetric quadrupole hyperfine interaction for  $M1$  transitions between excited ( $e$ ) and ground ( $g$ ) nuclear states with the spins  $I_e = 3/2 \rightarrow I_g = 1/2$ , as well as the chaotic distribution of the orientations of the molecular axes and an unpolarized source of gamma radiation.

We assume that the principal axis  $z'$  of the electric field gradient tensor on a nucleus composes a certain angle  $\theta$  with the easy libration axis  $z$  (Fig. 1). In this case, the harmonic librations of the molecule lead to the periodic reorientation of the principal axis of the electric field gradient tensor with the harmonic variation in the azimuth angle  $\phi$ :

$$\phi(t) = \phi_0 \sin(\Omega t + \Delta), \quad (1)$$

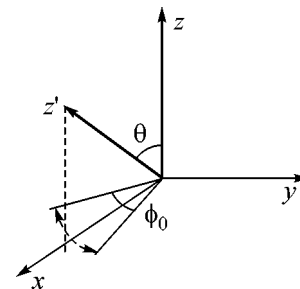


**Fig. 1.** Model of molecular librations with the oscillating principal axis of the electric field gradient tensor.

where  $\phi_0$ ,  $\Omega$ , and  $\Delta$  are the amplitude, frequency, and phase of the librations.

Taking the  $z$  axis as the quantization axis, one can represent the Hamiltonian of the axisymmetric quadrupole hyperfine interaction in the form

$$\hat{H}(t) = q \left[ \hat{I}_{z'(t)}^2 - \frac{1}{3} I(I+1) \right], \quad (2a)$$

where

$$q = \frac{3eQV_{zz}}{4I(2I-1)} \quad (2b)$$

is the quadrupole coupling constant,  $Q$  is the quadrupole moment of the nucleus,  $V_{zz}$  is the principal value of the electric field gradient tensor, and the  $z'$  axis periodically changes its direction according to Eq. (1). For quadrupole hyperfine interaction (2), the ground nuclear state with the spin  $I_g = 1/2$  appears to be degenerate and, correspondingly, Hamiltonian (2) in the molecular coordinate system can be represented in the matrix form only for an excited nuclear state in the basis of the  $z$  projections of the nuclear spin  $I_e = 3/2$ :

$$\hat{H}^{(e)}(t) = \frac{q}{4} \begin{pmatrix} 1 + 3 \cos 2\theta & 2\sqrt{3} \sin 2\theta e^{i\phi} & \sqrt{3}(1 - \cos 2\theta) e^{2i\phi} & 0 \\ 2\sqrt{3} \sin 2\theta e^{-i\phi} & -(1 + 3 \cos 2\theta) & 0 & \sqrt{3}(1 - \cos 2\theta) e^{2i\phi} \\ \sqrt{3}(1 - \cos 2\theta) e^{-2i\phi} & 0 & -(1 + 3 \cos 2\theta) & -2\sqrt{3} \sin 2\theta e^{i\phi} \\ 0 & \sqrt{3}(1 - \cos 2\theta) e^{-2i\phi} & -2\sqrt{3} \sin 2\theta e^{-i\phi} & 1 + 3 \cos 2\theta \end{pmatrix}, \quad (3)$$

where  $\phi \equiv \phi(t)$ .

In order to derive formulas for calculating the absorption spectra in this model, one can use the results obtained in [4–6], where the theory of Mössbauer spectra was developed for the case of the hyperfine magnetic field  $\mathbf{H}_{\text{hf}}(t)$  that acts on the nucleus and periodically varies along an arbitrary time trajectory. This theory was used to calculate the absorption spectra of nanostructured magnetic alloys under the action of an external rf field.

The form of Eqs. (24) and (25) in [5] shows that they can be used to describe the Mössbauer absorption spectra for an arbitrarily hyperfine interaction that periodically varies in time along an arbitrarily determined trajectory. In the case of axisymmetric quadrupole hyperfine interaction (2) with allowance for the degeneration of the ground state of the nucleus, a chaotic distribution of the orientations of the molecular axes, and an unpolarized gamma-radiation source, the expression for the absorption spectrum acquires the simpler form

$$\sigma(\omega) = \frac{\sigma_0 \Gamma_0}{2T_l(2I_e + 1)} \text{Re} \int_0^{T_l} dt_0 \times \int_{t_0}^{t_0 + T_l} \text{Tr} \left\{ \frac{\exp[i\tilde{\omega}(t - t_0)]}{\hat{I} - \exp(i\tilde{\omega}T_l) \hat{G}^{(e)}(t_0, t_0 + T_l)} \hat{G}^{(e)}(t_0, t) \right\} dt, \quad (4)$$

where  $T_l = 2\pi/\Omega$  is the period of librations,  $\hat{I}$  is the identity matrix, and

$$\hat{G}^{(e)}(t_0, t) = \hat{T} \exp \left\{ -i \int_{t_0}^t dt' \hat{H}^{(e)}(t') \right\} \quad (5)$$

is the evolution operator for the excited nuclear state. Using Eqs. (3)–(5), one can calculate a Mössbauer spectrum for the arbitrary model parameters  $q$ ,  $\theta$ ,  $\phi_0$ , and  $\Omega$ . Details of the optimization of the corresponding procedure of calculation by Eqs. (4) and (5) can be found in [6].

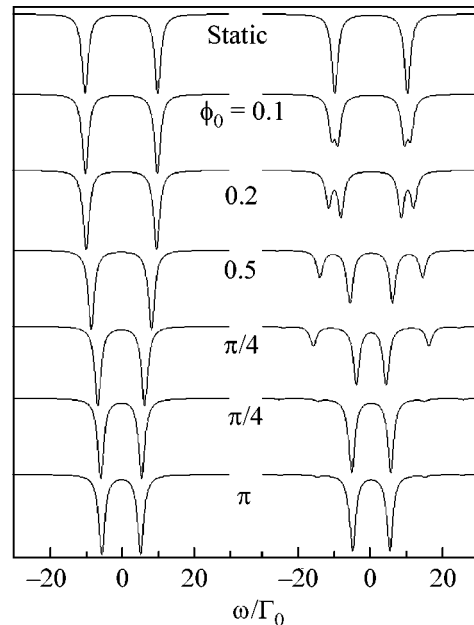


**Fig. 2.** Mössbauer absorption spectra in the case of the librations of the principal axis of the electric field gradient tensor in the plane  $\theta = 90^\circ$  for various amplitudes  $\phi_0$  (left part) in the limit of fast librations ( $\Omega \gg q$ ) and (right part) at the frequency  $\Omega = 2q$ . Here and below,  $q = 10\Gamma_0$  and the dashed line shows the position of one of the lines of the static quadrupole doublet.

Figure 2 shows the most typical Mössbauer spectra for the orientation of the principal axis of the electric field gradient tensor, which is perpendicular to the axis of librations, i.e., for in-plane oscillations ( $\theta = 90^\circ$ ). The left part of Fig. 2 shows the evolution of the shape of the absorption spectrum with varying the amplitude  $\phi_0$  of librations in the fast-oscillation limit when  $\Omega \gg q$ . In the absence of librations, the static Mössbauer spectrum constitutes a standard quadrupole line doublet with a splitting of  $2q$ , which is a superposition of only two Lorentzian lines of the natural width due to the degeneration of the excited nuclear state in the spin projection  $|m_e\rangle$ :

$$\sigma(\omega) = -\frac{\sigma_0 \Gamma_0}{4} \text{Im} \left( \frac{1}{\omega - q + i \frac{\Gamma_0}{2}} + \frac{1}{\omega + q + i \frac{\Gamma_0}{2}} \right). \quad (6)$$

As the amplitude of librations in this limit increases, the effective averaging of the quadrupole hyperfine interaction is observed with a smaller splitting  $2\bar{q}$  of the doublet lines. The effective constant  $\bar{q}$  of the quadrupole hyperfine interaction is easily estimated by considering the librations of the principal axis in the plane and passing to another coordinate system with the quantization axis in the plane of oscillations (Fig. 3).

$$\hat{H}'(t) = q \begin{pmatrix} 1 - \frac{3}{2} \phi_0^2 \sin^2(\Omega t + \Delta) & \sqrt{3} \phi_0 \sin(\Omega t + \Delta) \\ \sqrt{3} \phi_0 \sin(\Omega t + \Delta) & -\left(1 - \frac{3}{2} \phi_0^2 \sin^2(\Omega t + \Delta)\right) \end{pmatrix}. \quad (9)$$

In the limit of fast librations ( $\Omega \gg q$ ), the averaging of the off-diagonal matrix elements of effective Hamiltonian (9) over the oscillation period yields zero, whereas the averaging of its diagonal matrix elements leads to the effective decrease in the constant of the quadrupole hyperfine interaction:

$$\bar{q} = q \left( 1 - \frac{3}{4} \phi_0^2 \right). \quad (10)$$

We note that, in the limit of fast librations ( $\Omega \gg q$ ) with a large amplitude ( $\phi_0 \gg 1$ ), the effective constant of the quadrupole interaction asymptotically approaches a natural limit that is determined by the complete vanishing of the off-diagonal matrix elements of initial Hamiltonian (3) after averaging

$$\bar{q} = \frac{1 + 3 \cos 2\theta}{4} q. \quad (11)$$

Further, we perform the orthogonal transformation of the basis states to the new basis:

$$|i\rangle = \hat{A} |m_e\rangle, \quad (7a)$$

where the matrix elements of the transformation  $\hat{A}$  have the form

$$\begin{aligned} |1\rangle &= \frac{1}{\sqrt{2}} \left( \left| \frac{3}{2} \right\rangle + i \left| -\frac{3}{2} \right\rangle \right) \\ |2\rangle &= \frac{1}{\sqrt{2}} \left( \left| \frac{1}{2} \right\rangle - i \left| -\frac{1}{2} \right\rangle \right) \\ |3\rangle &= \frac{1}{\sqrt{2}} \left( \left| \frac{3}{2} \right\rangle - i \left| -\frac{3}{2} \right\rangle \right) \\ |4\rangle &= \frac{1}{\sqrt{2}} \left( \left| \frac{1}{2} \right\rangle + i \left| -\frac{1}{2} \right\rangle \right) \end{aligned} \quad (7b)$$

In the new basis, Hamiltonian (3) acquires the form of the block matrix

$$\hat{H}^{(e)}(t) = \begin{pmatrix} \hat{H}'(t) & 0 \\ 0 & \hat{H}^{*}(t) \end{pmatrix}, \quad (8)$$

where, in the limiting case of small oscillations ( $\phi_0 \ll 1$ ) with the accuracy to the terms quadratic in  $\phi_0$ ,

In this case,  $\bar{q} = -q/2$  for fast librations in the plane  $\theta = 90^\circ$ , whereas the effective constant  $\bar{q}$  is equal to zero for librations at the “magic” angle  $\theta = 54.7^\circ$ . At the same time, the shape of the Mössbauer spectrum in the limiting case of fast librations ( $\Omega \gg q$ ) is determined by Eq. (6), where  $q$  is replaced by  $\bar{q}$ .

The evolution of the shape of Mössbauer spectra in the model used for librations shows an additional qualitative effect that is expected in spectra when the oscillation frequency is close to the quadrupole splitting:

$$\Omega \approx 2q. \quad (12)$$

As is seen in the right series of spectra in Fig. 2, Mössbauer spectra under condition (12) exhibit the splitting of each of the lines of the static quadrupole doublet (6) and the value  $\delta$  of this splitting increases with the amplitude  $\phi_0$  of the librations. The calculations show that the effect is of a resonance character, which is shown in Fig. 4, where the symmetric resonance splitting of each of the quadrupole doublet lines disappears

at a small detuning of the frequency  $\Omega$  of librations from the exact resonance frequency.

In order to reveal the physical nature of this resonance effect, we consider the limiting case of small oscillations ( $\phi_0 \ll 1$ ) in the plane  $\theta = 90^\circ$ , which are described by the effective Hamiltonian given by Eq. (9). It is easy to see that this Hamiltonian formally describes the NMR with the effective nuclear spin  $I' = 1/2$  in a strong static magnetic field  $\mathbf{h}_0$  along the  $z$  axis and a weak oscillating field  $\mathbf{h}_1(t)$  that is linearly polarized along the  $x$  axis. Following the standard procedure accepted in NMR spectroscopy, one can suppose that the oscillating field  $\mathbf{h}_1(t)$  is the superposition of the right and left circularly polarized components  $\mathbf{h}_1(t)$  only one of which can induce resonance (see, e.g., [7]). In this case, the effective Hamiltonian of quadrupole hyperfine interaction (9) can be represented in the form

$$\hat{H}'(t) = h_0 \hat{I}'_z + h_1 (\hat{I}'_x \cos(\Omega t + \Delta) + \hat{I}'_y \sin(\Omega t + \Delta)), \quad (13)$$

where the intensities of the effective magnetic fields are determined by the parameters of the model of librations

$$h_0 = 2\bar{q}, \quad (14a)$$

$$\bar{q} = \left(1 - \frac{9}{16}\phi_0^2\right)q, \quad (14b)$$

$$h_1 = \sqrt{3}\phi_0 q. \quad (14c)$$

Hamiltonian (13) evidently describes the Zeeman interaction of the effective nuclear spin  $\mathbf{I}'$  with the effective magnetic field  $\mathbf{h}_0 + \mathbf{h}_1(t)$ , which rotates at a small angle to the  $z$  axis with the frequency  $\Omega$ . The theory of Mössbauer spectra for this case was developed in [8]. In complete analogy with the results of those works, it is possible to pass to the coordinate system rotating about the  $z$  axis with the frequency  $\Omega$  by means of unitary transformations using elementary operators of the rotation about the  $z$  axis:

$$\hat{U}(t) = e^{-i\Omega \hat{I}'_z t}. \quad (15)$$

Using these operators, one can perform integration with respect to time in evolution operator (5):

$$\hat{G}^{(e)}(t_0, t) = \hat{U}^+(t_0) e^{-i(t-t_0)\hat{H}'} \hat{U}(t), \quad (16)$$

where

$$\hat{H}' = (h_0 - \Omega)\hat{I}'_z + h_1\hat{I}'_x \quad (17)$$

is the time-independent Hamiltonian of the effective Zeeman interaction in the rotating coordinate system.

Then, following the procedure described in [5, 8], it is easy to represent an analytical solution for the absorption spectrum in the form

$$\sigma(\omega) = -\frac{\sigma_0 \Gamma_0}{4} \text{Im} \sum_{m'\tilde{m}'} \frac{|(m'|\tilde{m}')|^2}{\omega - \tilde{h}\tilde{m}' - \Omega m' + i\Gamma_0/2}. \quad (18)$$

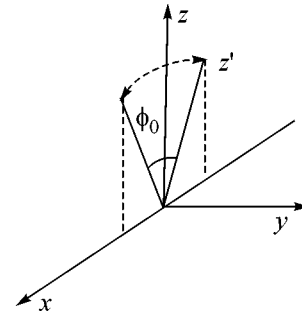


Fig. 3. Model of in-plane oscillations of the principal axis of the electric field gradient tensor.

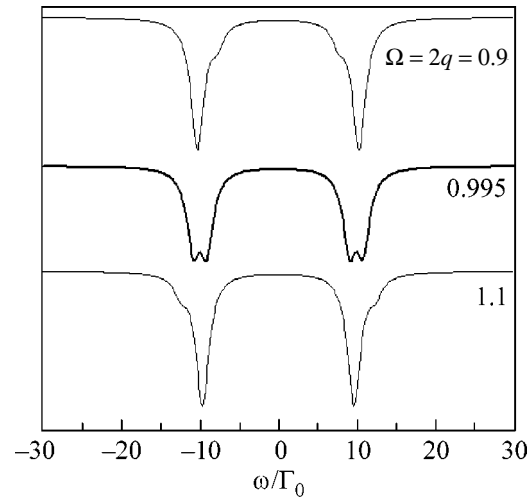


Fig. 4. Mössbauer spectra in the case of the small in-plane ( $\theta = 90^\circ$ ) librations ( $\phi_0 = 0.1$ ) of the principal axis of the electric field gradient near the nuclear quadrupole resonance.

Here,  $m'$  is the projection of the effective spin  $\mathbf{I}'$  onto the  $z$  axis and  $\tilde{m}'$  is the projection of  $\mathbf{I}'$  onto the  $\tilde{z}'$  axis that lies in the  $(x, z)$  plane and is inclined to the  $z$  axis at the angle  $\tilde{\theta}'$  such that

$$\tan \tilde{\theta}' = \frac{h_1}{h_0 - \Omega}, \quad (19)$$

and the effective magnetic field, which is directed along the  $\tilde{z}'$  axis in the rotating coordinate system, is given by the expression

$$\tilde{h} = \sqrt{(h_0 - \Omega)^2 + h_1^2}. \quad (20)$$

We remind that Eq. (18) is valid only in the limiting case of small librations ( $\phi_0 \ll 1$ ) in the plane  $\theta = 90^\circ$  and near resonance, which is determined by the more exact condition

$$\Omega = h_0 = 2\bar{q}. \quad (21)$$

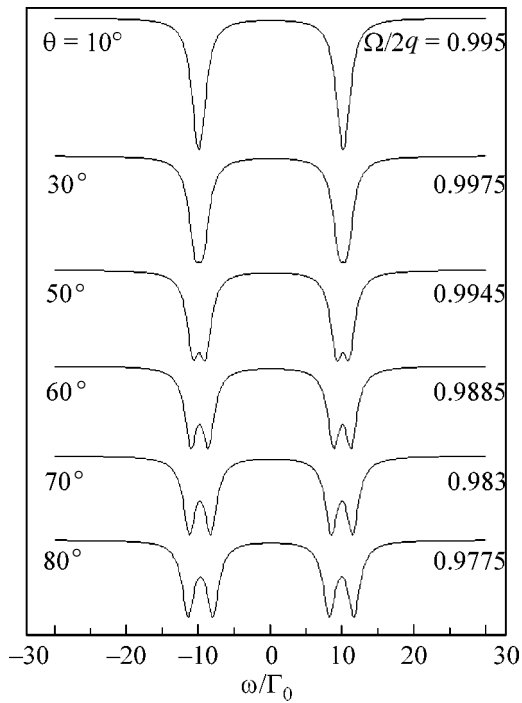


**Fig. 5.** Mössbauer spectra in the case of the small librations ( $\phi_0 = 0.2$ ) of the principal axis of the electric field gradient tensor at various angles  $\theta$  in the exact nuclear quadrupole resonance determined by Eqs. (21) and (26).

According to Eq. (18), the absorption spectrum in this case is the superposition of four Lorentzian lines of natural width whose intensity is determined by the mutual orientation of the  $z$  and  $\tilde{z}$  axes. Simple analysis of Eqs. (18)–(20) shows that, at exact resonance, when condition (21) is satisfied, the Mössbauer spectrum is the superposition of four Lorentzian lines of the natural width:

$$\sigma(\omega) = -\frac{\sigma_0 \Gamma_0}{8} \times \text{Im} \left( \frac{1}{\omega - (\bar{q} - \delta) + i \frac{\Gamma_0}{2}} + \frac{1}{\omega - (\bar{q} + \delta) + i \frac{\Gamma_0}{2}} + \frac{1}{\omega + (\bar{q} - \delta) + i \frac{\Gamma_0}{2}} + \frac{1}{\omega + (\bar{q} + \delta) + i \frac{\Gamma_0}{2}} \right). \quad (22)$$

In this case, the position of the spectral lines is determined by both the effective constant of quadrupole interaction (14b) and the resonance splitting value

$$\delta \equiv h_1 = \sqrt{3} \phi_0 q. \quad (23)$$

According to Eq. (20), when the frequency of librations is slightly detuned from resonance frequency

(21), the symmetric resonance splitting of each line of the quadrupole doublet almost disappears, which is clearly seen in Fig. 4.

It is interesting to analyze the manifestation of the NQR, which is described above, for the librations of the principal axis of the electric field gradient tensor at the arbitrary angle  $\theta$ . As is seen in Fig. 1, small librations ( $\phi_0 \ll 1$ ) in the first approximation are also oscillations in a plane, but the principal axis of the electric field gradient tensor in this case oscillates in the  $(y, z')$  plane with the effectively smaller amplitude:

$$\phi'(t, \theta) = \phi'_0(\theta) \sin(\Omega t + \Delta), \quad (24a)$$

where  $\phi'(t, \theta)$  is the azimuth angle in the  $(y, z')$  plane and

$$\phi'_0(\theta) = \phi_0 \sin \theta. \quad (24b)$$

Then, one can return to the coordinate system with the quantization axis lying in the plane of librations (see Fig. 3) and rewrite Eqs. (9), (10), and (13)–(23), where  $\phi_0$  should be replaced by  $\phi'_0(\theta)$  for small librations ( $\phi_0 \ll 1$ ) of the principal axis of the electric field gradient tensor at the arbitrary angle  $\theta$ . In particular, in the limit of fast librations ( $\Omega \gg q$ ), the effective constant of the quadrupole hyperfine interaction acquires the form [rather than (10)]

$$\bar{q} = q \left( 1 - \frac{3}{4} \phi_0^2 \sin^2 \theta \right). \quad (25)$$

Concerning the resonance effects, we note that the Mössbauer absorption spectrum for small librations ( $\phi_0 \ll 1$ ) of the principal axis of the electric field gradient tensor at the arbitrary angle  $\theta$  is described by Eq. (18) near resonance (21), where

$$\bar{q} = q \left( 1 - \frac{9}{16} \phi_0^2 \sin^2 \theta \right), \quad (26a)$$

$$\delta \equiv h_1 = \sqrt{3} \phi_0 \sin \theta q. \quad (26b)$$

Correspondingly, the Mössbauer spectrum in exact resonance (21) is described by Eq. (22) with effective constants given by Eqs. (26).

Figure 5 shows the resonance shapes of Mössbauer spectra for the small librations ( $\phi_0 = 0.2$ ) of the principal axis of the electric field gradient tensor at various angles to the axis of librations. These spectra were calculated by general formula (4). It is clearly seen that the characteristics of the resonance splitting for various angles  $\theta$  are well reproduced by simple expressions (26).

Thus, the harmonic librations of the principal axis of the electric field gradient tensor in cages of the liquid lead to the specific transformation of Mössbauer absorption spectra, in which the qualitatively different natures of rotational motions in such materials can be manifested. All qualitative effects observed in Mössbauer spectra in the framework of the above model for

oscillations of the principal axis of the electric field gradient tensor about an arbitrary axis at an arbitrary angle are described in terms of the effective constant of the quadrupole hyperfine interaction and the resonance splitting of the main lines of the quadrupole doublet. The corresponding simple analytical expressions can be effectively used to analyze experimental Mössbauer spectra in liquids.

It is necessary to emphasize that all the above specific forms of the quadrupole hyperfine structure can be observed in Mössbauer spectra in liquids only when the stochastic relaxation processes are slower than the characteristic period of the librations. However, even if the features predicted above for the formation of the quadrupole hyperfine structure are not pronounced in spectra due to the superposition of partial components corresponding to different time trajectories of the molecular angular momentum or due to relaxation effects, the traces of the predicted specific forms can be manifested in experimental Mössbauer spectra and should be taken into account when analyzing these spectra.

We point to the fundamental difference between the predicted NQR in gamma resonance spectra and the well-known physical NQR method, which is widely applied, in particular, for the detection of explosive and drug substances in airports. In the latter method, resonance is observed in the presence of the external rf magnetic field, whose frequency is tuned to the quadrupole splitting value (12) [9]. A similar realization of NQR is also possible in Mössbauer spectroscopy and resonance effects for the case of magnetic hyperfine interaction (an analog of NMR), which are similar in manifestation (splitting of lines) and are well known and even observed in the spectra of soft magnetic materials under the action of the rf field [5, 10]

For the possibility of observing the predicted NQR in the distinct form, it is necessary to ensure the situation where the principal axis of the electric field gradient tensor undergoes small oscillations with a given frequency and at a given angle due to the external excitation. In this case, choosing the corresponding characteristics of the external excitation, one can realize the conditions necessary for observing the reso-

nance forms of Mössbauer spectra shown in Figs. 2, 4, and 5.

This study was supported by the Russian Foundation for Basic Research (project no. 05-02-16297) and the European Synchrotron Radiation Facility (contract no. ESRF-074-2005). I am sincerely grateful to I. Sergeev, who works at the European Synchrotron Radiation Facility, for fruitful discussions of the problem of rotational dynamics in "liquids."

#### REFERENCES

1. H. Bayer, *Z. Phys.* **130**, 227 (1951).
2. L. Liu, A. Faraone, and S.-H. Chen, *Phys. Rev. E* **65**, 041506 (2002).
3. P. P. Craig and N. Sutin, *Phys. Rev. Lett.* **11**, 460 (1963); A. Abras and J. G. Mullen, *Phys. Rev. A* **6**, 2343 (1972); S. L. Ruby, J. C. Love, P. A. Flinn, and B. J. Zabransky, *Appl. Phys. Lett.* **27**, 320 (1975); D. C. Champeney, E. S. M. Higgy, and R. G. Ross, *J. Phys. C: Solid State Phys.* **8**, 507 (1975); A. Vasquez and P. A. Flinn, *J. Chem. Phys.* **72**, 1958 (1980); G. U. Nienhaus, H. Frauenfelder, and F. Parak, *Phys. Rev. B* **43**, 3345 (1991); I. Chang, H. Hartmann, Yu. Krupyanski, *et al.*, *Chem. Phys.* **212**, 221 (1996); A. Gahl, M. Hillberg, F. J. Litterst, *et al.*, *J. Phys.: Condens. Matter* **10**, 961 (1998).
4. A. M. Afanas'ev, M. A. Chuev, and J. Hesse, *Phys. Rev. B* **56**, 5489 (1997).
5. A. M. Afanas'ev, M. A. Chuev, and J. Hesse, *Zh. Éksp. Teor. Fiz.* **113**, 1799 (1998) [*JETP* **86**, 983 (1998)].
6. A. M. Afanas'ev, M. A. Chuev, and J. Hesse, *Zh. Éksp. Teor. Fiz.* **116**, 1001 (1999) [*JETP* **89**, 533 (1999)].
7. E. Matthias, B. Olsen, D. A. Shirley, *et al.*, *Phys. Rev. A* **4**, 1626 (1971).
8. A. M. Afanas'ev and M. A. Chuev, *Pis'ma Zh. Éksp. Teor. Fiz.* **77**, 489 (2003) [*JETP Lett.* **77**, 415 (2003)]; *Dokl. Akad. Nauk* **390**, 750 (2003) [*Dokl. Phys.* **48**, 277 (2003)]; *J. Phys.: Condens. Matter* **15**, 4827 (2003).
9. V. S. Grechushkin, *Nuclear Quadrupole Interactions in Solids* (Nauka, Moscow, 1973) [in Russian].
10. F. G. Vagizov, R. A. Manapov, E. K. Sadykov, and L. L. Zakirov, *Hyperfine Interact.* **116**, 91 (1998).

*Translated by R. Tyapaev*

# Transverse Charge-Carrier Transfer in Selectively Doped GaAs/AlGaAs Semiconductor Heterostructures with Longitudinal Current Flow

E. I. Lonskaya<sup>a</sup> and O. A. Ryabushkin<sup>a, b</sup>

<sup>a</sup> Institute of Radio Engineering and Electronics, Russian Academy of Sciences,  
Fryazino, Moscow region, 141190 Russia

e-mail: e.lonskaya@mail.ru

<sup>b</sup> Moscow Institute of Physics and Technology (State University),  
Dolgoprudnyĭ, Moscow region, 141700 Russia

Received October 17, 2005

Photoreflectance spectra of selectively doped GaAs/AlGaAs heterostructures are studied under the conditions of direct current flow along the structure layers. Using a model developed for the spectra, variations of the internal transverse electric fields are calculated for longitudinal current flow. It is proved experimentally that even a weak heating of electrons in such structures leads to a spatial redistribution of electrons in the direction transverse to the heterostructure layers. © 2005 Pleiades Publishing, Inc.

PACS numbers: 73.40.Kp, 78.40.Fy, 78.66.Fd

Advances in the manufacturing technology and methods for the precision diagnostics of semiconductor heterostructures with selective doping made from the beginning of the 1980s and up to the present allow for the development of unique fast-response field-effect transistors based on GaAs/AlGaAs, InGaAs/AlGaAs, GaN/AlGaN, and other heterostructures [1–4]. In spite of the diversity of the investigations of selectively doped heterostructures, the question of the behavior of electrons at the passage of a high-density current in such structures remains open [5]. The heating of electrons in selectively doped heterostructures was studied theoretically in many papers [5–7], in which it was shown that charge carriers heated by a longitudinal electric current can spatially move from a high-conductivity region of the heterostructure (channel) to low-conductivity layers. This charge transfer was related to the regions of negative differential conductivity experimentally observed in the current–voltage characteristics (CVCs) of heterostructures [5]. However, measurements of CVCs cannot provide detailed information on the variation of the electron states and the band diagram of the heterostructure upon heating of charge carriers. To solve this problem, we propose using the modulation reflectance techniques [8–10], which allow the built-in electric fields and characteristic band-structure energies to be measured. Modulation reflectance spectra also contain information on both free and bound (exciton and impurity) electron states.

This paper reports on a photoreflectance study of the variations of the electron energy states and the band diagram of a selectively doped GaAs/Al<sub>x</sub>Ga<sub>1-x</sub>As ( $x \approx 0.2$ )

heterostructure under conditions of charge carrier heating. The heterostructure was grown by molecular beam epitaxy and consisted of a 100-Å cap layer of undoped GaAs (region 1 in Fig. 1), a 600-Å layer of doped *n*-AlGaAs ( $N_D \approx 0.7 \times 10^{18} \text{ cm}^{-3}$ ) (regions 2 and 3), a 100-Å spacer layer of undoped AlGaAs (region 4), a 1-μm buffer layer of undoped GaAs (regions 5–7), and a GaAs/AlGaAs technological superlattice grown on a semi-insulating GaAs substrate. The heterostructure band diagram is schematically shown in Fig. 1. The sample length and width were 10 and 3 mm, respectively. The measurements for this sample were carried out at room temperature. The heating of the carriers was carried out by a direct electric current passing along the heterostructure layers (along the *Y* axis, Fig. 1) through

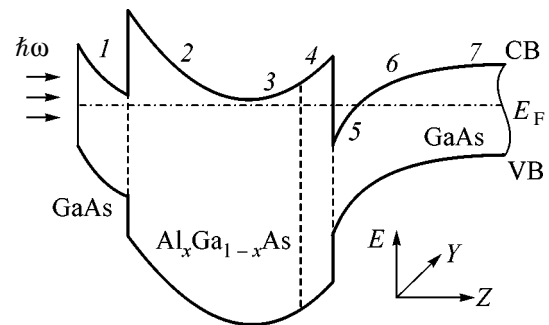


**Fig. 1.** Profile of the conduction band (CB) bottom and the valence band (VB) top of the active part of the studied heterostructure,  $E_F$  is the Fermi level.

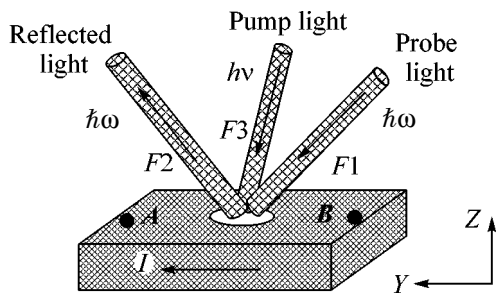


**Fig. 2.** Arrangement of fibers and a sample with contacts when measuring the photoreflectance spectra with a current. The diameter of the *F1*, *F2*, and *F3* fibers was 300  $\mu\text{m}$ .

indium ohmic contacts formed on the sample surface. The electric power dissipated in the sample  $P_{dc}$  varied from 0 to 110 mW with the current varied from 0 to 10 mA. In this range of the external current, regions with a negative differential conductivity were absent in the CVC of the studied sample.

To measure the photoreflectance (PR) spectra [9–11], the sample was illuminated with probe light of constant intensity with the photon energies  $\hbar\omega$  near the characteristic energy features of the heterostructure layers and the pump light of modulated intensity with the quantum energies  $\hbar\nu$  larger than the bandgap width of the structure semiconductor layers. The probe light from an incandescent lamp passed through an optical filter and was supplied to the sample using multimode optical fiber *F1*. Radiation from a helium–neon laser with the energy  $\hbar\nu = 1.96$  eV ( $\lambda = 632.8$  nm) was used as the pump light. It was supplied to the sample using the same fiber *F3*. The pump light intensity was modulated by a mechanical chopper with a frequency of 2 kHz. The areas on the sample surface illuminated with the probe and pump lights were spatially matched (Fig. 2). The probe light reflected from the sample was directed to fiber *F2*. The intensity of the probe light reflected from the sample had a constant  $I(\omega)$  and a variable  $\Delta I(\omega)$  component. The exit aperture of fiber *F2* was matched to the entrance aperture of the spectrometer. At the spectrometer exit, the spectral components of the probe light were detected by a photodiode. The pump light with an intensity of  $\sim 1$  W/cm<sup>2</sup> generated nonequilibrium electrons and holes in both the GaAs and AlGaAs layers. It is known that the light reflectance  $R(\omega)$  of semiconductors in the spectral range of energies in the vicinity of the fundamental absorption edge  $\hbar\omega \sim E_g$  depends on the strength of the built-in electric field [12]. Modulation of the pump light led to a modification of the internal electric fields and, as a result, to modulation of the probe light reflectance  $\Delta R(\omega)$ . The relative change in the reflected light intensity  $\Delta I(\omega)/I(\omega)$  proportional to  $\Delta R(\omega)/R(\omega)$  was measured at the pump light modulation frequency using synchronous detection.

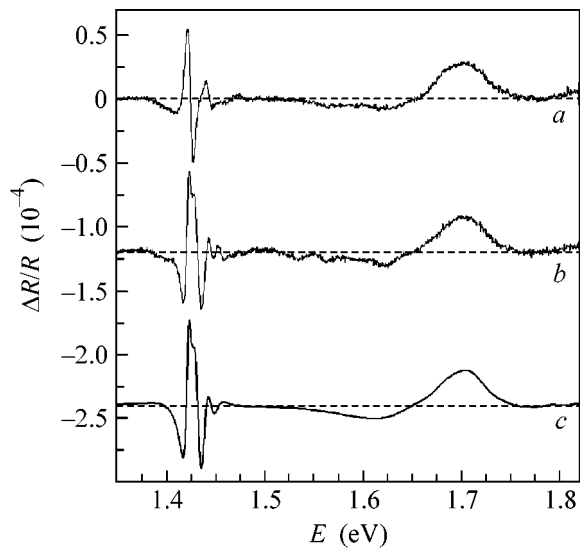


**Fig. 3.** Experimental photoreflectance spectra: (a) without a current, (b) at the electric power dissipated in the sample  $P_{dc} = 12$  mW, and (c) a model photoreflectance spectrum at  $P_{dc} = 12$  mW.

The PR spectrum measured in the absence of a current is presented in Fig. 3a. In this spectrum, features can be distinguished in the region of energies  $E$  1.38–1.48 eV in the vicinity of the GaAs bandgap energy

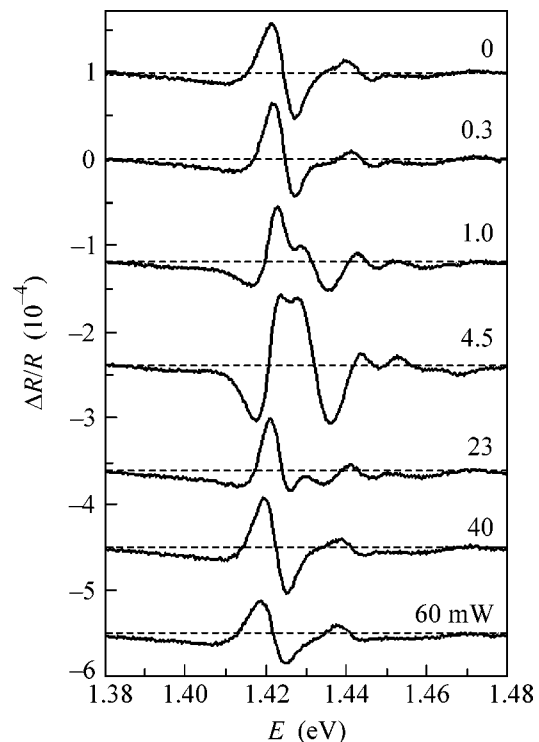


**Fig. 4.** Experimental photoreflectance spectra for energies  $E \sim \text{GaAs } E_g$  at various values of  $P_{dc}$  from 0 to 60 mW.

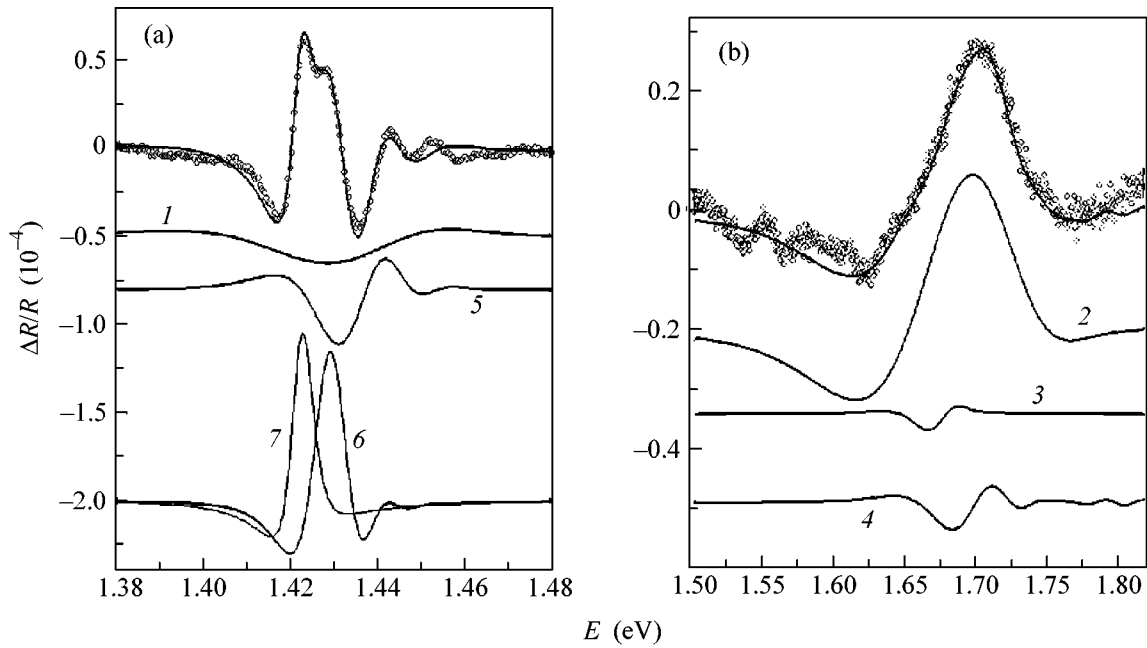


**Fig. 5.** Example of the model photoreflectance spectrum at  $P_{dc} = 12$  mW: contribution to the photoreflectance spectrum from (a) various GaAs layers and (b) AlGaAs layers. The numbering of layers is given according to Fig. 1. A comparison of (points) the measured photoreflectance spectrum and (solid lines) the model spectrum is shown above.

( $E_g = 1.4273$  eV). These features characterize several GaAs layers. The features in the region of energies 1.6–1.8 eV ( $E_g = 1.67$  eV) are due to the AlGaAs layer.

Passing a longitudinal electric current along the sample layers substantially changes the PR spectra, see Figs. 3b and 4. It is seen in the figures that the spectrum in the region of energies 1.38–1.48 eV is clearly separated into two parts: in the left-hand side of the spectrum at the energy  $E < \text{GaAs } E_g$ , a characteristic oscillation changes its width and amplitude with increasing current power; in the right-hand side of the spectrum at the energy  $E > \text{GaAs } E_g$ , additional oscillations appear, whose amplitude also changes. No notable changes in the region of energies 1.6–1.8 eV of the PR spectrum are observed upon passing a current. Even from a qualitative comparison of the PR spectra in these energy ranges, a conclusion can be made that electrons in the GaAs layers are spatially redistributed upon heating by a current.

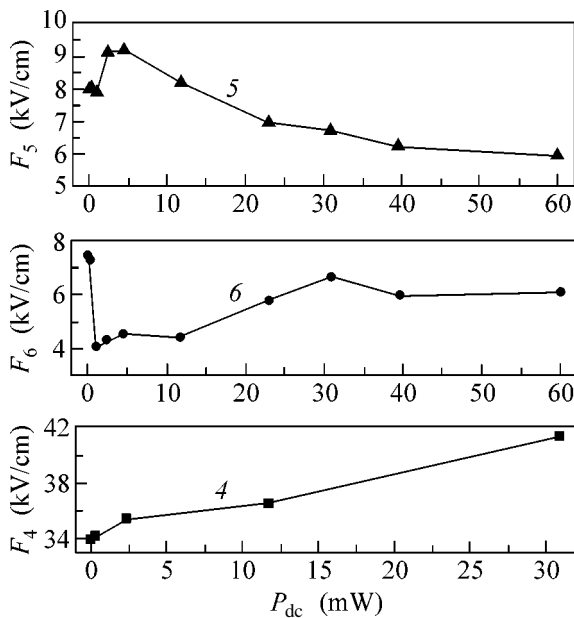


**Fig. 6.** Calculated changes in the internal (transverse) electric fields  $F_5$ ,  $F_6$ , and  $F_4$  in heterostructure regions 5, 6, and 4 at various values of the electric power  $P_{dc}$  dissipated in the sample. The numbering of regions is given according to Fig. 1. The computational error in the determination of the internal fields was 5%.

A physical model was developed to describe in detail the measured PR spectra, in which two main mechanisms were considered [10, 13, 14]: (1) the built-in electric fields in the GaAs layers with fields 1, 5, and 6 (Fig. 1) and in the AlGaAs layers with fields 2–4 are changed because of the redistribution of heated electrons; (2) the binding energy of free excitons in layer 7 of the GaAs is changed by heated electrons. Conventional analytical expressions and parameters were used directly in the calculations of the PR spectra [15–18]. An example of the model PR spectrum at the electric power dissipated in the sample  $P_{dc} = 12$  mW is demonstrated in Fig. 3c and Fig. 5. The values of the built-in fields calculated from the model PR spectra at a longitudinal current flow of different power in sample layers

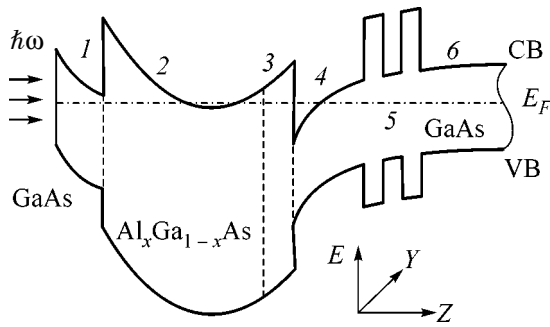


**Fig. 7.** Band diagram of the sample with an additional superlattice in the GaAs buffer layer (region 5).

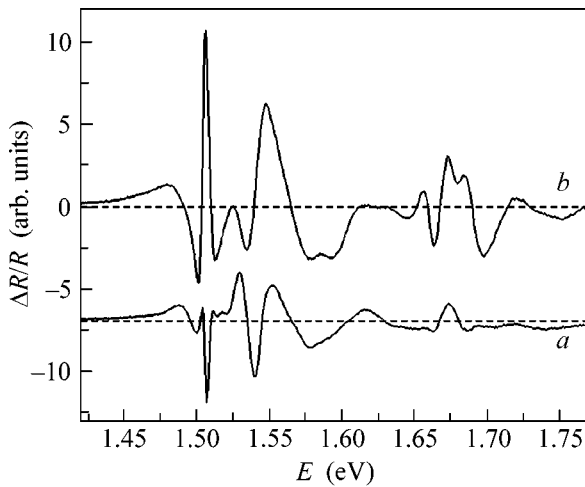


**Fig. 8.** Experimental photoreflectance spectra for the heterostructure with an additional superlattice (*a*) in the absence of a current and (*b*) at the electric power dissipated in the sample  $P_{dc} = 160$  mW.

4–6 are shown in Fig. 6. The internal fields in layers 1, 2, and 3 remain virtually unchanged with the current and are equal in absolute value to 30, 165, and 14 kV/cm, respectively. The binding energy of free excitons decreases from  $4.1 \pm 0.1$  meV without current to  $3.6 \pm 0.1$  meV at  $P_{dc} = 60$  mW. The heating of free electrons and excitons lead to insignificant heating of the lattice, which was  $\Delta T \sim 5$  K at  $P_{dc} = 60$  mW. Thus, it is evident from the results obtained that, upon charge carrier heating, electrons pass from the AlGaAs layer (layer 4) and the GaAs channel (layer 5) in the depth of the GaAs buffer layer (layers 6, 7), leading to a modification of exciton states [14]. It should be emphasized that the insignificant changes in the PR spectra in the range of energies in the vicinity of AlGaAs  $E_g$  are most likely due to the fact that the weakly heated electrons from the GaAs channel cannot overcome the barrier in the AlGaAs conduction band and leave the heating region into the depth of the GaAs buffer.

To study the effect of the heated electrons on the doped AlGaAs layer, analogous, selectively doped GaAs/Al<sub>x</sub>Ga<sub>1-x</sub>As heterostructures ( $x \approx 0.12$ ) with an additional superlattice in the GaAs buffer layer were studied. The superlattice was located at a distance of 225 Å from the active interface [10]. The band diagram of such a heterostructure is schematically shown in Fig. 7. To enhance the heating of electrons, the measurements of the PR spectra of this sample with a longitudinal current flow were performed at a temperature of 77 K.

The experimental PR spectrum without a current is presented in Fig. 8*a*. The GaAs bandgap energy was 1.51 eV. The peak at an energy of 1.506 eV was due to the modulation of exciton states in region 6 of the GaAs buffer layer (Fig. 7) by the pump light. The modulation of excitons in quantum wells (region 5 in Fig. 7) and built-in fields in GaAs layers 1 and 4 leads to the formation of spectral features in the energy range 1.52–1.63 eV. The spectral features in the energy range 1.66–1.72 eV are due to the modification of the internal fields in AlGaAs layers 2 and 3. It is evident in Fig. 8*b* that the PR spectrum of this heterostructure also substantially changes in the entire measured energy range upon passing a longitudinal current. In the range of energies in the vicinity of AlGaAs  $E_g$  (1.67 eV), the simply shaped peak of the PR spectrum is split into two types of oscillations with different periods and amplitudes. This is connected with an increase in the internal fields in regions 2 and 3 of the AlGaAs layer, that is, with charge carrier transfer in the direction transverse to the heterostructure layers. This behavior of the PR spectrum allowed us to separate experimentally two values of the measured built-in fields (on the right and on the left) in the AlGaAs layer (regions 2 and 3 in Fig. 7). Thus, it is seen that each heterostructure exhibits its own features of the heating of charge carriers, which are reliably detected by the light modulation reflectance techniques.

Note, in conclusion, that we experimentally confirmed charge carrier transfer in the real space for selectively doped GaAs/AlGaAs heterostructures. It is shown that weak heating of electrons significantly affects the heterostructure band diagram even at room temperature.

This work was supported in part by the Russian Foundation for Basic Research, project no. 03-02-16942.

## REFERENCES

1. Zh. I. Alferov, Usp. Fiz. Nauk **172**, 1068 (2002).
2. T. Mimura, S. Hiyamizu, and T. Fujii, Jpn. J. Appl. Phys. **19**, L225 (1980).
3. T. Drummond, W. Masselink, and H. Morkoc, Proc. IEEE **74**, 773 (1986).

4. S. Karmalkar, M. Shur, and R. Gaska, in *Wide Energy Bandgap Electronic Devices*, Ed. by F. Ren and J. Zolper (World Sci., River Edge, N.J., 2003), p. 173.
5. Z. Gribnikov, K. Hess, and G. Kosinovsky, *J. Appl. Phys.* **77**, 1337 (1995).
6. A. Garmatin and A. Kal'fa, *Fiz. Tekh. Poluprovodn. (Leningrad)* **19**, 1147 (1985) [*Sov. Phys. Semicond.* **19**, 704 (1985)].
7. A. A. Kal'fa and A. S. Tager, *Fiz. Tekh. Poluprovodn. (Leningrad)* **21**, 1353 (1987) [*Sov. Phys. Semicond.* **21**, 823 (1987)].
8. O. A. Ryabushkin and V. A. Sablikov, *Pis'ma Zh. Éksp. Teor. Fiz.* **67**, 217 (1998) [*JETP Lett.* **67**, 233 (1998)].
9. J. Misiewicz, P. Sitarek, G. Sek, *et al.*, *Mater. Sci.* **21**, 263 (2003).
10. O. A. Ryabushkin, E. I. Lonskaya, A. E. Sotnikov, *et al.*, *Phys. Status Solidi A* **202**, 1282 (2005).
11. O. A. Ryabushkin and E. I. Lonskaya, *Physica E (Amsterdam)* **13**, 374 (2002).
12. D. E. Aspnes and N. Bottka, in *Semiconductors and Semimetals*, Vol. 9: *Modulation Techniques*, Ed. by R. K. Willardson and A. C. Beer (Academic, New York, 1972), Chap. 6.
13. O. A. Ryabushkin and V. A. Sablikov, *Proc. SPIE* **3732**, 137 (1999).
14. O. A. Ryabushkin, in *Proceedings of International Symposium on Nanostructures: Physics and Technology* (St. Petersburg, 1997), p. 270.
15. R. A. Batchelor, A. C. Brown, and A. Hamnett, *Phys. Rev. B* **41**, 1401 (1990).
16. C. Tanguy, *Phys. Rev. Lett.* **75**, 4090 (1995); *Phys. Rev. Lett.* **76**, 716 (1996).
17. S. Adachi, *Phys. Rev. B* **41**, 1003 (1990).
18. M. El Allali, C. B. Sorensen, E. Veje, *et al.*, *Phys. Rev. B* **48**, 4398 (1993).

*Translated by A. Bagatur'yants*

# Optical Transitions for 2D Electrons at the Solid Hydrogen–Vapor Interface

V. Shikin and S. Nazin

*Institute of Solid State Physics, Russian Academy of Sciences, Chernogolovka, Moscow region, 142432 Russia*

*e-mail: shikin@issp.ac.ru*

Received October 17, 2005

Details of the problem of “vertical” transitions between discrete levels of 2D electrons on the surface of liquid (solid) dielectrics in the presence of a gas over this surface (their own vapors or artificially produced combinations such as solid hydrogen–gaseous helium) are discussed. The structure of the interaction of an electron with a gaseous medium, where the so-called scattering length appears to depend on the gas density, is determined. The role of Van der Waals forces, which attract gas atoms to the dielectric surface, is shown. A notion of quasi-2D electron bound states on gas atoms is introduced. The experimental data concerning the effect of the gas on the frequencies of optical transitions for 2D electrons over the surface of solid hydrogen are discussed using this information. © 2005 Pleiades Publishing, Inc.

PACS numbers: 67.55.Ig

The concept of a quantum computer and the discussed possibility of its realization by using 2D electrons over helium have renewed interest in optical transitions between discrete electron levels on the surface of liquid (solid) dielectrics (see, e.g., [1, 2]). In view of this circumstance, it is reasonable to discuss phenomena accompanying “vertical” excitation of 2D electrons. The pressure effect is one of them. The nonzero gas pressure changes the transition frequencies in a discrete electron system embedded in a gas if it gives rise to different shifts of the ground and high-lying levels. Selective “gas-induced” shifts of levels, which were known for atomic systems as early as since works [3–5], occur in loose 2D electron states on the flat liquid–vapor interface. However, the causes of gas selection are different. The contact effect of the gas on deep electron levels is negligible in atomic systems. It is expected only for high-lying semiclassical states with a scale estimated in the so-called optical approximation, where the shift  $W_0$  is determined by the expression [3–5]

$$W_0 = \frac{2\pi\hbar^2 a_0}{m} n_g. \quad (1)$$

Here,  $m$  is the free-electron mass,  $n_g$  is the average gas density, and  $a_0$  is the so-called scattering length (the  $s$  component of the scattering amplitude). This effect is manifested only in optical media involving transitions from the ground state to high levels located near the edge of the continuous spectrum (for details, see [3–5]).

The localization scale of loose 2D electron states over the liquid (solid) dielectric differs from the atomic. As a result, the ground and high-lying 2D states are “embedded” in the gaseous medium almost equiprobably

[at least in the optical approximation given by Eq. (1)]. Although gas shifts of electron levels exist, they are identical in the optical approximation. The distances between levels do not change and, as a result, the pressure does not affect optical frequencies. The selectivity of the interaction of 2D electrons with the gaseous medium is manifested beyond the framework of the optical approximation. In this case, the vertical localization of 2D electrons in the ground state on the length  $\lambda_1$ , which is noticeably less than the structural characteristic of the gas  $R \propto n_g^{-1/3}$ , is important. The 2D pressure effect becomes noticeable if

$$\lambda_1 \leq R, \text{ and } \lambda_l \geq R \text{ for } l > 1, \quad R = n_g^{-1/3}. \quad (2)$$

Here,  $\lambda_1$  and  $\lambda_l$  are the localization lengths of the electron wave function over the substrate in the ground and excited states, respectively, and  $n_g$  is the average gas density.

Thus, the pressure effect in the “flat” case can be observed without involving high-lying electron levels, which are necessarily involved for observing the pressure effect in atomic optics. However, conditions (2) that allow the operation with the minimum numbers of the electron state must be satisfied.

The scenario given by Eq. (2) was realized in the elegant experiments reported in [6, 7], where the authors, by varying substrates, showed that the pressure effect is almost insignificant [conditions (2) are strongly violated] for 1–2 transitions at the vapor–liquid helium interface. The gas effect is slightly manifested at the vapor–liquid neon interface. Conditions (2) are satisfied for the combination vapor–solid hydrogen (deute-

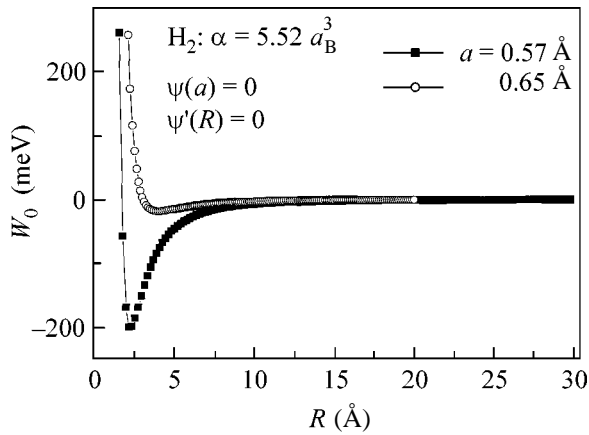


**Fig. 1.** Energy  $W_0$  vs.  $R = n_g^{-1/3}$ , where  $n_g$  is the gas density, for the boundary conditions  $\psi(a) = 0$  and  $d\psi/dr|_{r=R} = 0$ . The constant  $a$  is chosen so that the energy  $W$  is equal to zero for a reasonable  $n_g$  value corresponding to the liquid state of hydrogen. In this way, the scale of the scattering length  $a_0(n_g)$  is uniquely determined (see Fig. 2).

rium) or solid  $H_2$  + gaseous helium, and the pressure effect is distinctly observed. For hydrogen,

$$d\omega_{12}/dn_g < 0, \quad \hbar\omega_{12} = |\Delta_2 - \Delta_1|, \quad (3)$$

and for the  $H_2$  + He,

$$d\omega_{12}^*/dn_g > 0, \quad \hbar\omega_{12}^* = |\Delta_2^* - \Delta_1^*|, \quad (4)$$

where  $\Delta_l$  and  $\Delta_l^*$  are the 2D electron levels over solid hydrogen or in gaseous helium, respectively (the solid + gaseous  $H_2$  combination is allowed by the phase diagram of hydrogen; the  $H_2$  + gaseous helium pair is realized at temperatures quite low for gaseous  $H_2$ , when hydrogen vapor is almost frozen, whereas gaseous helium can exist over hydrogen).

The authors of [6, 7] did not attach particular importance to the specificity of the interaction of the ground 2D electron state with the gas. This specificity, as well as results represented by Eqs. (3) and (4), should be interpreted. Inequality (4) seems to be natural (the interaction energy of electrons with dense helium is positive), whereas the inequality for the case of  $H_2$  is paradoxical: solid  $H_2$ , as well as helium, repulses electrons from its bulk (which explains the presence of 2D electron states at the solid–vapor interface), whereas gaseous  $H_2$  attracts them [which explains the negative sign of derivative (3)]. This paper is devoted to the detailed discussion of the above problems.

**1.** We begin with the problem of the interaction energy  $W_0$  of a low-energy electron with a gaseous medium. The optical approximation given by Eq. (1) is conventional in this case. The definition of  $W$  given by

Eq. (1) is valid if the interaction of electrons with atoms is contact:

$$V_0(\mathbf{r} - \mathbf{R}_i) = \frac{2\pi\hbar^2 a_0}{m} \delta(\mathbf{r} - \mathbf{R}_i), \quad (5)$$

where  $\mathbf{r}$  and  $\mathbf{R}_i$  are the radius-vectors of the electron and given atom, respectively, and  $a_0$  is the effective amplitude of the electron scattering by a single atom, which depends slightly on the gas density. However, in the problem under consideration, there is the polarization attraction

$$V(r) = \begin{cases} V_0, & r \leq a \\ -\alpha e^2/2r^4, & r > a, \end{cases} \quad (6)$$

for which the introduction of the scattering length is problematic (see [8, 9]) and the coordinate dependence can hardly be treated as short-range. Here,  $\alpha$  and  $a$  are the polarizability and radius of the atom, respectively. The potential  $V(r)$  given by Eq. (6) is too rough for the accurate calculation of the binding energy of an extra electron with the neutral atom in noble gases (see, e.g., [10]). The basic inaccuracy is associated with the necessity of simulating the boundary condition for the electron wave function on the atomic surface with radius  $a$  that excludes the fall of a particle onto the attractive center and allows the reduction of the problem of electron localization to a single-particle problem. The importance of the problem of boundary conditions is seen at least from the fact that the helium atom, whose atomic polarization  $\alpha$  is minimal among noble gases, binds the extra electron with the binding energy  $\sim 0.06$  eV, whereas other representatives of this series with much larger  $\alpha$  values have no bound states (for more details, see [10]). The single-electron formalism proposed in [11] qualitatively takes into account this circumstance. This formalism is based on the solution of the wave equation in the Wigner–Seitz spherical cell with a given atom at its center and with the boundary conditions for the wave function  $\psi(r)$  that allow the transition of an electron from one cell to another, as well as the specificity of the behavior of the electron near the atom (whether or not this atom forms a negative ion). As a result, one can determine the electron energy  $W$  in the cell and, comparing it with  $W_0$  given by Eq. (1), find the gas-density dependence of the effective scattering length  $a_0$ . Such a plan was realized in [11] for the inert-gas family. Similar calculations for hydrogen  $H_2$  in the model that do not imply the localization on a single  $H_2$  molecule are shown in Figs. 1 and 2 (any data on  $H_2^-$  are absent in comprehensive book [10] devoted to various negative ions; moreover, a version with the electron wave function vanishing on the sphere with radius  $a$  of the central atom of the Wigner cell is least favorable for the appearance of the negative part in the electron energy  $W(n_g)$ ; thereby, the results shown in Figs. 1 and 2 are lower estimates). The value  $\alpha =$

$5.52a_B^3$  is taken from [12]. The choice of the effective radius  $a$  of the  $H_2$  molecule is used to fit the zero point of the energy  $W$  to the liquid hydrogen density. The range of the negative  $a_0$  values, which is necessary for correct interpretation of the data reported in [6, 7], is marked by the arrows in Fig. 2.

2. An important detail that enabled the authors of [6, 7] to explain their observation is the absence of the gas effect on the ground state of the electron over the hydrogen substrate and its presence for level 2 [see comments to Eqs. (1) and (2)]. However, the gas density  $n_g(z)$  is noticeably increased near the substrate. In the framework of the scenario accepted in [6, 7], it is necessary to analyze this difficulty.

The local increase in  $n_g(z)$  is caused by the Van der Waals forces between gas atoms and the substrate. In the classical approximation,

$$n_g(z) = n_g \exp(f\Omega/Tz^3), \quad \Omega \approx 4\pi a^3/3, \quad (7)$$

where  $n_g$  is the average gas density far from the substrate,  $f$  is the Van der Waals energy (on the order of 20 K),  $\Omega$  is the volume of one gas atom, and the  $Z$  axis is directed along the normal to the substrate with the positive direction corresponding to the gas phase.

The combination of the energies

$$V(z) = W_0(z) + V_{im}(z), \quad V_{im}(z) = -\Lambda/z, \quad (8)$$

$$\Lambda = (\epsilon - 1)e^2/4(\epsilon + 1),$$

where  $\epsilon$  is the dielectric constant of the dielectric (its value for hydrogen is taken from [13]) and  $W_0(z)$  is the energy given by Eq. (1) with  $n_g(z)$  specified by Eq. (7) (and with the possible dependence of  $a_0$  on  $n_g$ ), is responsible for the localization of electrons near the dielectric surface. In contrast to the vacuum limit with the sharp boundary, this energy has no singularity and, correspondingly, the pure "hydrogen" approximation for wave functions and eigenenergies becomes nonoptimal. It is clear that the gas inhomogeneity shifts the electron to the region  $z > 0$ ; i.e., the electron localization degree decreases compared to the hydrogen limit. The shift can be estimated by determining the position of the minimum of the potential  $V(z)$  given by Eq. (8):

$$z_{\min}^2 = \frac{6\pi\hbar^2 a_0}{m} n_g \frac{f\Omega}{\Lambda T}. \quad (9)$$

According to this expression,  $z_{\min}$  is on the order of several angstroms.

Perturbation of Eq. (8) can be approximately taken into account by the known method {introduction of a nonsingular potential  $U(z)$  by analogy with [14]}:

$$V(z) = \begin{cases} V_0, & z < 0 \\ -\Lambda/(z + z_{\min}), & z > 0, \end{cases} \quad (10)$$

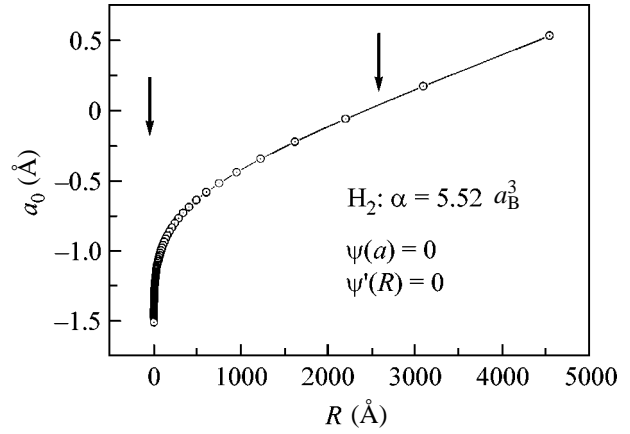


Fig. 2. Scattering length  $a_0$  vs.  $R = n_g^{-1/3}$  as determined due to the comparison of the energy  $W_0$  plotted in Fig. 1 and the energy  $W_0$  given by Eq. (1). The arrows show the region of negative  $a_0$  values that is necessary for the correct interpretation of the experimental data reported in [6, 7].

where  $z_{\min}$  is determined from Eq. (9),  $V_0 > 0$  is the electron energy in the condensed phase, and this energy is assumed to be independent of the gas density. The  $z_{\min}$  value is usually chosen by fitting the experimental frequencies of optical transitions between 2D electron levels over the liquid (see [14]). In the case under consideration,  $z_{\min}$  is given and the level shifts are determined by the formula

$$\Delta_l = \Delta_l^o + \frac{\hbar^2}{2m} \left[ z_{\min} - \left( \frac{\hbar^2}{2mV_0} \right)^{1/2} \right] \left. \left( df_l/dz \right)^2 \right|_{z=0}. \quad (11)$$

The derivatives  $df_l/dz|_{z=0}$  decrease as  $l$  increases. Therefore, the optical frequencies must decrease at  $z_{\min} \neq 0$ . This dependence is qualitatively clear, because the layer  $z_{\min} \neq 0$  effectively shifts the electron from the main substrate. The contribution of channel (11) will be taken into account when constructing the general dependence  $\omega_{12}(n_g)$  for hydrogen. However, it is evidently insensitive to the sign of  $a_0$ .

3. Thus, we have discussed approximations in the description of the interaction of an electron located far from the liquid-vapor interface with the gaseous medium [this interaction is given by Eq. (4) with  $a_0$  taken from data shown in Fig. 2] and revealed how the 2D electron responds to the Van der Waals compression of the gas near the liquid-vapor interface. Now, let us discuss why the ground state of the 2D electron undergoes specific interaction with the gaseous medium as compared to a similar interaction far from the interface. We remind the reader that, if the electron-gas interaction is described by Eq. (1) even with the renormalized scattering length, the first-order corrections to the energies of the ground ( $l = 1$ ) and excited ( $l > 1$ ) levels are identical under the condition that the gas density is constant right up to the interface. The interaction energy

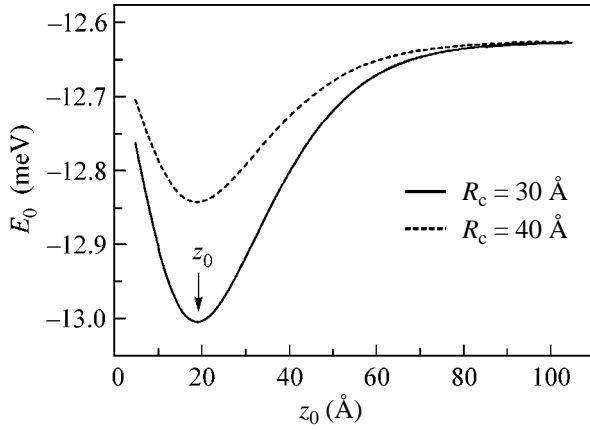


**Fig. 3.** Energy  $W_1(z_0, n_g)$  of the electron ground state in the cylindrical cell specified by Eqs. (12) and (13) vs. the position  $z_0$  of the central atom. The extremum is clearly seen at the point  $z_0 = z_0^*$ .

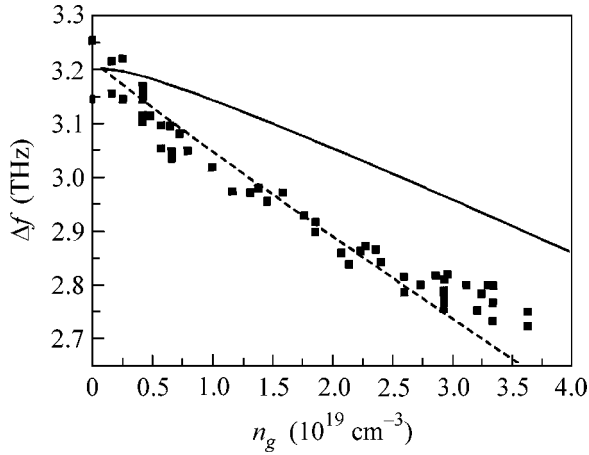


**Fig. 4.** Pressure effect (the gas-density effect on vertical transitions) for the 1–2 transition in the 2D electron system at the (solid hydrogen–its own vapor) interface as obtained by (dashed line) disregarding and (solid line) taking into account the gas-density dependence of the ground state energy of the 2D electron (for details, see the main text). The experimental points are taken from [6, 7] and  $a_0 \approx -1.4a_B$  under the experimental conditions described in [6, 7].

can be extracted from the corresponding integrals and the resulting expressions have the normalization form identical for all electron states.

In alternative terms of cells, which are also naturally used near the boundary, qualitatively new circumstances affecting the formation of the cell structure appear. First, its periphery must have the cylindrical shape according to the boundary conditions. Second, under the condition  $\lambda_1 \leq R$ , the central atom is not equiprobably distributed along the entire  $Z$  axis (as in the optical approximation); rather, it is located with a well-defined probability at a finite distance  $z_0$  that

approximately coincides with the maximum of the  $z$  component of the electron wave function. The latter statement is not evident and must be proved in the framework of the proposed model.

We should formally solve the wave equation for the electron [with the wave function  $\psi(\rho, z)$ , where  $\rho$  is the 2D radius along the substrate surface] in the field of the image forces  $V_{im}(z)$ , which are specified by Eqs. (8) and hold it near the surface with the dielectric constant  $\epsilon = \epsilon_{H_2} = 1.2936$ , and the polarization potential  $V(z - z_0, \rho)$  (6) of the atom located at height  $z_0$  over the surface:

$$V_{total}(z, \rho) = -\frac{\alpha e^2}{2((z - z_0)^2 + \rho^2)^2} + V_{im}(z). \quad (12)$$

The boundary conditions

$$\begin{aligned} \psi|_{z=0} = 0, \quad \psi|_{z=h} = 0, \quad \psi|_{(z-z_0)^2 + \rho^2 = a^2} = 0, \\ \frac{\partial \psi}{\partial \rho}|_{\rho=R_c} = 0, \quad R_c = n_g^{-1/3} / \sqrt{\pi} \end{aligned} \quad (13)$$

have the “spherical” form on the gas atom with the center at the point  $(z = z_0, \rho = 0)$  and the cylindrical structure on the outer surfaces of the cell (the cylinder height  $h = z_0 + 2R_c$ , where  $R_c$  is the cylinder radius, is high enough for the wave function of the ground state in the image-force field to almost vanish at  $z = h$ ).

The total energy of the electron at a given gas density (i.e., at a given  $R_c$  value) as a function of the parameter  $z_0$  has a deep minimum at  $z_0 = z_0^*$  correlating with the position of the maximum of the unperturbed electron wave function  $\psi_1(\rho, z)$  over the dielectric surface in the absence of the gas. The presence of such an extremum that depends slightly on  $R_c$  is illustrated in Fig. 3 for two values of this radius. Supposing that the gas atom is mainly located at this extremum, we unambiguously determine the minimum electron energy  $W_1(z_0^*, n_g)$  as a function of the gas density.

Thus, we have determined the characteristic shift energy  $W_1(n_g)$  of high-lying levels, which is estimated in the optical approximation by Eq. (1), the energy  $W_1(z_0^*, n_g)$  following from the numerical solution of the problem given by Eqs. (12) and (13) with the position of the central atom of the cell at the point  $z_0$  corresponding to the energy extremum in Fig. 3, and the Van der Waals shifts of the levels, which are given by Eq. (11). Using this information, one can construct the frequency shift  $\omega_{21}(n_g)$  applicable for comparison between the theory and data reported in [6, 7]:

$$\omega_{21}(n_g) = (\delta\Delta_{21}^0 + \delta\Delta_{21}^{vdW} + \delta\Delta_2 - \delta\Delta_1) / \hbar. \quad (14)$$

Here,  $\delta\Delta_{21}^0$  is the initial difference between the electron energy levels in the absence of the gas;  $\delta\Delta_{21}^{vdW} = \Delta_2 - \Delta_1$ , where  $\Delta_1$  and  $\Delta_2$  are given by Eq. (11);  $\delta\Delta_2$  is the

optical-approximation shift of level 2; and  $\delta\Delta_1$  is the shift of level 1 in the model described by Eqs. (12) and (13).

Figure 4, which illustrates the final results, shows the shift of the 1–2 transition frequency (dashed line) as calculated in optical approximation (1) for level 2 with the scattering length shown in Fig. 2 when the gas perturbation of level 1 is disregarded and (solid line) as calculated by taking into account the gas correction of the ground-state energy of the 2D electron through the solution of the wave problem given by Eqs. (12) and (13). In both cases, the slope  $d\omega_{12}/dn_g < 0$  and the effect magnitude correlate with the data reported in [6, 7]. This correlation indicates that the interpretation of causes of the negativity of the scattering length and the selection mechanism in the interaction of 2D electrons with gas atoms is qualitatively correct. The numerical difference between the slopes of the dashed and solid lines can be reduced by additionally varying the boundary conditions on the Wigner–Seitz cell surface. These details will be discussed elsewhere.

### SUMMARY

Details of the pressure effect for optical transitions in the system of 2D electrons at the solid hydrogen–gas interface have been discussed. This phenomenon is linear in the interaction of the electron with gas atoms and thereby provides information on the sign of the amplitude of electron scattering by a single atom. The effect becomes observable if 2D electron states selectively interact with the gaseous medium. For relatively shallow 2D electron levels at the interface between two media, the nature of selectivity requires a special consideration beyond the optical approximation given by Eq. (1). In our interpretation, the selectivity is primarily determined by the structure of the Wigner–Seitz cell for electrons far from the phase interface and on its surface. In the former case, this structure is spherically symmetric with a separate hydrogen atom at the cell center and the minimum energy  $W_0(n_g)$  shown in Fig. 1. The cell near the interface under the condition  $\lambda_1 \ll R$  has the form of a cylinder with radius  $R_c$  and the height  $h = z_0 + R_c$  with the central atom located on the cylinder axis at the point  $z_0 = z_0^*$ , where the energy  $W_1(z_0, n_g)$  shown in

Fig. 3 is minimal. The behavior of the minimum energy  $W_1(z_0^*, n_g) = \delta\Delta_1$  differs from the behavior of the energy  $W(n_g) = \delta\Delta_2$  shown in Fig. 1. The difference  $W(n_g) - W_1(z_0^*, n_g)$  is shown in Fig. 4 as the difference between the frequencies  $\omega_{21}(n_g)$  given by Eq. (14). The above formalism provides additional capabilities for improving the agreement between the theory and experiment that will be discussed in a more detailed work.

We are grateful to S.V. Iordanskiĭ for discussion of the results. This work was supported in part by the Russian Foundation for Basic Research (project no. 03-02-16121) and the Presidium of the Russian Academy of Sciences (program no. P28).

### REFERENCES

1. P. Platzman and M. Dykman, *Science* **284**, 1967 (1999).
2. E. Collin, W. Bailey, P. Fazoli, *et al.*, *Phys. Rev. Lett.* **89**, 245301 (2002).
3. E. Fermi, *Nuovo Cimento* **11**, 157 (1934).
4. E. Amaldi and E. Segre, *Nuovo Cimento* **11**, 145 (1934).
5. H. Margenau and W. W. Watson, *Rev. Mod. Phys.* **8**, 22 (1936).
6. V. Zav'yalov and I. Smol'yaninov, *Zh. Éksp. Teor. Fiz.* **92**, 339 (1987) [*Sov. Phys. JETP* **65**, 194 (1987)].
7. I. Smol'yaninov, Candidate's Dissertation in Physics and Mathematics (Inst. for Physical Problems, USSR Academy of Sciences, Moscow, 1989).
8. E. Vogt and G. H. Wannier, *Phys. Rev.* **95**, 1190 (1954).
9. T. O'Malley, L. Spruch, and L. Rosenberg, *J. Math. Phys.* **2**, 491 (1961).
10. B. M. Smirnov, *Negative Ions* (Atomizdat, Moscow, 1978; McGraw-Hill, New York, 1982).
11. S. Nazin and V. Shikin, *Pis'ma Zh. Éksp. Teor. Fiz.* **82**, 255 (2005) [*JETP Lett.* **82**, 236 (2005)].
12. T. F. O'Malley, *Phys. Rev.* **130**, 1020 (1963).
13. *Physical Encyclopedic Dictionary*, Ed. by B. A. Vvedenskiĭ (Sovetskaya Éntsiklopediya, Moscow, 1960) [in Russian].
14. C. Grimes, T. Brown, M. Burns, and C. Zipfel, *Phys. Rev. B* **13**, 140 (1976).

*Translated by R. Tyapaev*